NUMERICAL LOAD TESTING OF A GEOSYNTHETIC REINFORCED SOIL

A THESIS SUBMITTED TO THE GRADUATE DIVISION OF THE
UNIVERSITY OF HAWAIʻI AT MĀNOA IN PARTIAL FULFILLMENT
OF THE REQUIREMENTS FOR THE DEGREE OF

MASTER OF SCIENCE

IN

CIVIL ENGINEERING

DECEMBER 2016

By

Landon Hideaki Kaya

Thesis Committee:

Phillip Ooi, Chair Person
Horst G. Brandes
Teruo Nakai

ACKNOWLEDGMENTS

I would like to sincerely thank the following people:

- My advisor, Dr. Phillip Ooi, for his unwavering, welcoming, insightful guidance and encouragement throughout the entirety of my master's research.
- Dr. Teruo Nakai and Dr. Shahin Hossain for giving me the opportunity to use their FEMtij programs for my research, for modifying the software to meet the needs of this research and for troubleshooting numerous runs.
- Dr. Phillip Ooi, Dr. Teruo Nakai, and Dr. Horst Brandes for agreeing to be on my thesis committee.
- Ms. Melia Iwamoto for the many discussions on GRS due to her previous experience with working on GRS column load tests.
- The Federal Highway Administration's (FHWA) lab technicians for providing me with quality soil test data that was used in the analyses of the geosynthetic reinforced soil (GRS) column load test.
- Dr. Phillip Ooi, Dr. Teruo Nakai, Dr. Horst Brandes, Dr. Adrian Archilla, and Dr. Xiong Zhang for the courses I took to increase my knowledge during my master's program and thus further preparing me for my career.
- Ms. Janis Kusatsu and Ms. Jean Zheng for their friendly help in filling out and organizing my graduate forms.
- And finally, my family and friends for motivating and supporting me throughout this whole experience.

ABSTRACT

Geosynthetic reinforced soil (GRS) abutments have been increasingly used due to several advantages over traditional concrete abutment walls. Two notable advantages include: (1) Fast and cost-efficient method of construction due to the elimination of cast-in-place reinforced concrete abutments; and (2) Reduced carbon footprint due to less use of cement since cement production produces an enormous amount of carbon dioxide. GRS abutments have to be designed for settlement and bearing capacity. Available design procedures are often based on large scale load tests on GRS columns which is expensive and not routinely performed. Therefore, using a numerical model to simulate these load or performance tests would offer a more economical alternative.

The FEMtij program was used for analyzing GRS load tests in 2-D and 3-D. In 2-D , the ideal constitutive models for the soil, CMU blocks, geotextile, and footing were the subloading t_{ij}, Drucker-Prager, linear elastic with post-yield softening, and linear elastic, respectively. Three factors that greatly affect the GRS capacity were investigated by performing a sensitivity analysis. These factors were the effects of soil-footing friction angle, the constitutive model of the CMU (Drucker Prager vs linear elastic), and the constitutive model of the geotextile (linear elastic with post-yield softening vs linear elastic). The 3D analyses were less successful, details of which can be found in the thesis.

From the calculated 2D load-settlement and lateral displacement curves, and heat maps of shear strain, the following observations and conclusions were made: (1) The capacity of the GRS increased with increasing soil-footing friction angle. (2) Using a Drucker-Prager model for the CMUs caused the GRS to have a smaller capacity than if they were linear elastic. (3) Modelling CMU blocks with an elasto-plastic model is important due to some of the CMUs crushing during

the performance tests. (4) By allowing the geotextiles to soften after exceeding its tensile strength, the GRS capacity was less than if the geotextiles were linear elastic. (5) It is important to model a softening geotextile because of the observed ripping of the geotextiles during the performance tests. (6) Shear bands were observed in the GRS columns. They are inclined at 45° and 50° to the horizontal for GRS columns without and with CMU blocks, respectively.

Table of Contents

LIST OF TABLES

LIST OF FIGURES

1 INTRODUCTION

1.1 Geosynthetic Reinforced Soil

Geosynthetic reinforced soil (GRS) is defined as closely-spaced (≤ 0.3 m) layers of geosynthetic reinforcement and compacted granular fill material (Adams et al., 2011). GRS abutments for single span bridges have become increasingly common and this system has been termed GRS-IBS, where IBS stands for Integrated Bridge System. This increase in interest for GRS-IBS is due to the following advantages:

1. Fast and cost-effective method of bridge support. It eliminates the need for cast-in-place reinforced concrete abutments traditionally supported on deep foundations.
2. Reduced carbon footprint with less use of concrete and hence cement, the production of which is known to contribute significantly to global warming.
3. Quality compaction control can be realized since backfill is placed in thin lifts between the closely spaced geosynthetics.
4. Closely-spaced geosynthetic systems are not prone to catastrophic abutment collapse. This has been observed in numerous load tests carried out to failure (Nicks et al., 2013).
5. Can be built in variable weather conditions with common labor, materials and equipment, and can be easily modified in the field.
6. Alleviates the "bump at the end-of-the-bridge" problem caused by differential settlement between the bridge abutment and the approach roadway. This is made possible by eliminating deep foundations, by using GRS to construct the integrated approach to the superstructure and by limiting its use to short, single-span integral abutment bridge systems.
7. Very flexible system that is amenable to differential settlement.

An example of this system is shown in Figure 1-1 and it consists of a reinforced soil foundation, a GRS abutment, and the GRS integrated appoarch.

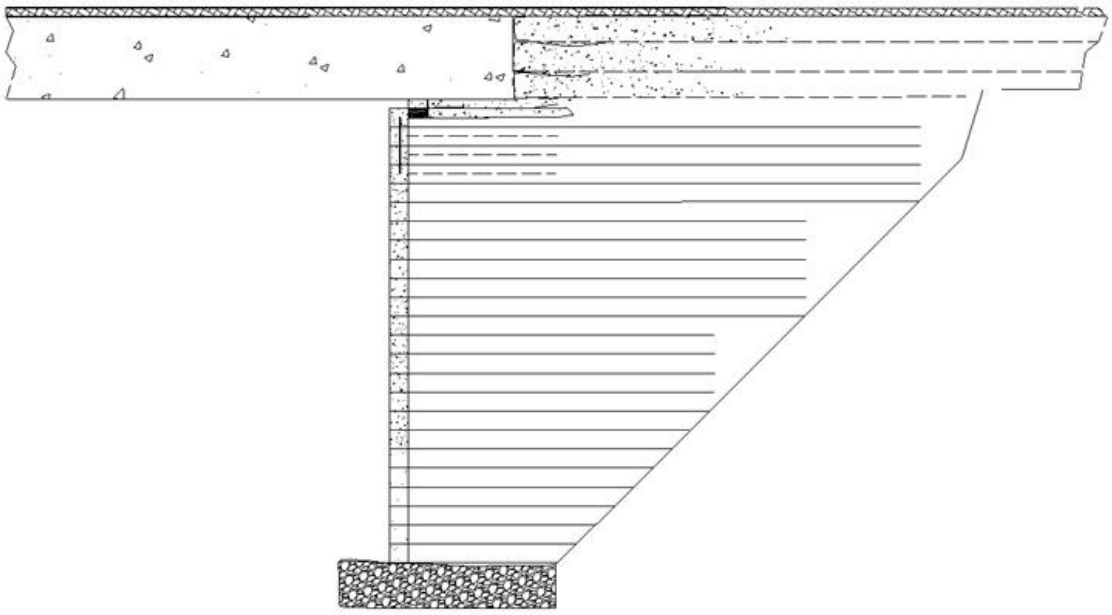

Figure 1-1: Example of geosynthetic reinforced soil integrated bridge system (GRS-IBS).

To design GRS abutments, large scale performance load tests are sometimes performed on GRS columns to analyze for settlement and bearing capacity.

1.2 Motivation

Due to the fact that large scale GRS column performance tests are expensive and not routinely performed in the design process, this thesis aims to investigate the possibility of modelling these load tests with a numerical model. Numerical load tests would offer an economical alternative and can be performed in a relatively short amount of time with no expenses on material costs necessary.

1.3 Thesis Overview

The objectives of this thesis include the following: (1) Develop a 2-D plane strain numerical model using a very robust and versatile soil constitutive model; (2) Investigate the effects of friction between footing and soil, as well as the effects of the facing and geotextile properties on the results of the numerical load tests; (3) Create a 3-D model of the performance tests and compare it to the 2-D model.

2 LITERATURE REVIEW

In this chapter, the constitutive model used in this research work is first reviewed. It is the subloading t_{ij} model by Nakai and Mihara (1984), which is based on the Cam-Clay model. This model was chosen because of the following capabilities:

1. It can mimic the stress-strain and volume change behavior of the soil well by considering the influence of density.
2. It can consider the influence of the intermediate principal stress by transforming the stresses onto a spatially mobilized (t_{ij}) plane.
3. In terms of convergence, the model is very stable because on a transformed plane, the geomaterial does not go into tension.
4. The plasticity is associated during hardening implying it will not result in any negative work done.
5. The model is flexible and robust as it is able to fit the stress-strain and volume change characteristics of a wide variety of geomaterials.

Before describing the subloading t_{ij} model, the Cam-Clay model is first described since it forms the basis of the subloading t_{ij} model.

2.1 Cam-Clay Model

Roscoe and Schofield (1963) developed the Cam-Clay model to predict the behavior of soft clays from Cambridge, England in triaxial and consolidation tests. Roscoe and Burland (1968) then improved the original Cam-Clay model by changing the shape of the yield surface. Known as the modified Cam-Clay model, this model has become well known in the soil mechanics community. The prefix "modified" is dropped from hereon and the model will be referred to as the Cam-Clay model for the sake of brevity. The symbols used in the Cam-Clay model are defined as follows:

χ	Scalar multiplier
δ	Signifies incremental value
∂	Signifies partial derivative

e	Void ratio
ε_{ij}	Strain tensor
$\varepsilon_{1,2,3}$	Principal strains
ε_p^e	Elastic volumetric strain
ε_q^e	Elastic deviatoric strain
ε_p^p	Plastic volumetric strain
ε_q^p	Plastic deviatoric strain
f	Yield locus
g	Plastic potential
G'	Shear modulus
ϕ	Critical state friction angle
η	Stress ratio (=q/p')
p'	Mean principal stress
p'_{oA} & p'_{oB}	Reference size for yield locus (i.e. pre-consolidation stress)
κ	Slope of unload-reload line
λ	Slope of isotropic normally consolidation line
M	Slope between origin and top of yield locus in q-p' space
N	Reference specific volume at 1 atmosphere
υ	Specific volume (=1 + e)
q	Deviatoric stress
σ_{ij}	Stress tensor
$\sigma_{1,2,3}$	Principal stresses

The Cam-Clay model captures the soil's stress-strain and volume change behavior by simplifying the 9 components of the stress tensor σ_{ij} into two stress variables: p' (mean stress) and q (deviatoric stress). Similarly, the strain tensor ε_{ij} is also simplified by using the volumetric strain (ε_v or ε_p) and deviatoric strain (ε_d or ε_q). These variables are defined visually in the octahedral plane (see Figure 2-1) in the principal stress and strain space.

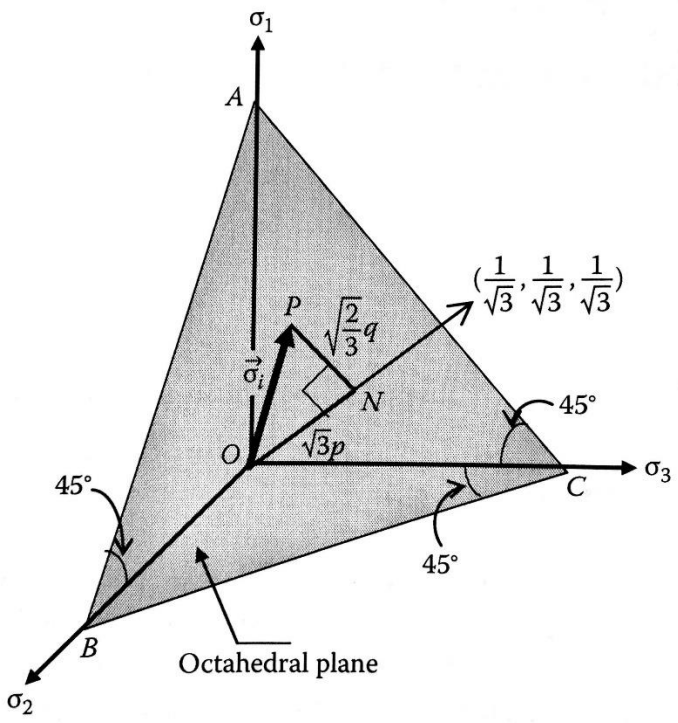

(a)

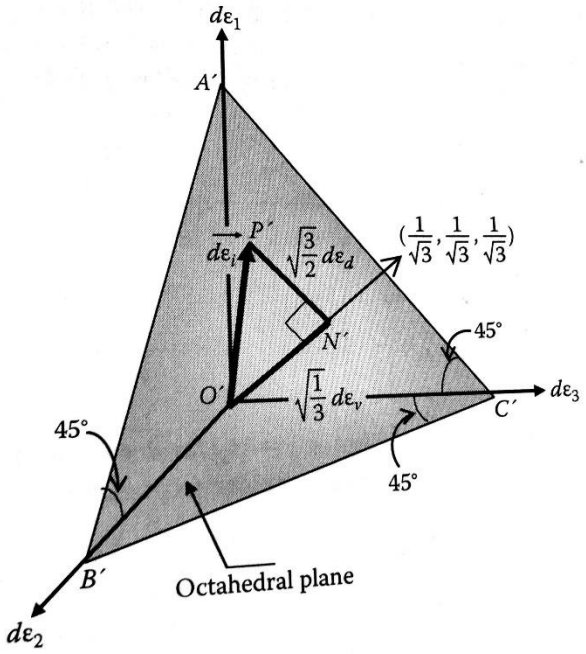

(b)

Figure 2-1: Using the octahedral plane to describe: (a) p' and q (b) ε_v and ε_d (Nakai, 2013).

As shown in Figure 2-1(a), p' and q are normal and in-plane to the octahedral plane, respectively. Similarly, in Figure 2-1(b), $d\varepsilon_p$ and $d\varepsilon_q$ are normal and in-plane to the octahedral

plane, respectively. All these stresses and strains are defined via the following equations (Nakai, 2013):

$$p' = \frac{1}{3}(\sigma_1 + \sigma_2 + \sigma_3) = \frac{1}{3}\sigma_{ij}\delta_{ij} \quad \text{(Equation 2.1)}$$

$$q = \frac{1}{\sqrt{2}}\sqrt{(\sigma_1 - \sigma_2)^2 + (\sigma_2 - \sigma_3)^2 + (\sigma_3 - \sigma_1)^2} \quad \text{(Equation 2.2)}$$

$$d\varepsilon_v = d\varepsilon_1 + d\varepsilon_2 + d\varepsilon_3 = d\varepsilon_{ij}\delta_{ij} \quad \text{(Equation 2.3)}$$

$$d\varepsilon_d = \frac{\sqrt{2}}{3}\sqrt{(d\varepsilon_1 - d\varepsilon_2)^2 + (d\varepsilon_2 - d\varepsilon_3)^2 + (d\varepsilon_3 - d\varepsilon_1)^2} \quad \text{(Equation 2.4)}$$

The intermediate principal stress $\sigma_2 = \sigma_3$ in triaxial compression and $\sigma_2 = \sigma_1$ in triaxial extension. Thus, equations 2.1 and 2.2 simplify to:

$$p' = \frac{\sigma_1 + 2\sigma_3}{3}, q = (\sigma_1 - \sigma_3) \text{ [Triaxial Compression] (Equation 2.5)}$$

$$p' = \frac{2\sigma_1 + \sigma_3}{3}, q = (\sigma_1 - \sigma_3) \quad \text{[Triaxial Extension] (Equation 2.6)}$$

To capture the relationship between stresses and strains, the Cam-Clay model uses a yield surface to determine whether the soil behaves elastically or elasto-plastically when sheared.

The yield surface is one within the q-p' space where any stresses that remain within this surface results in strains that are recoverable when the stresses are removed and thus the soil acts purely elastically. However, when stress excursions beyond the yield surface occur, plastic strains develop, along with elastic strains, and the yield surface expands. This is shown in Figure 2-2 where the yield locus for the Cam-Clay model is elliptical in shape and its size is governed by the stress p'_{oA} initially but changes to p'_{oB} when the yield surface expands.

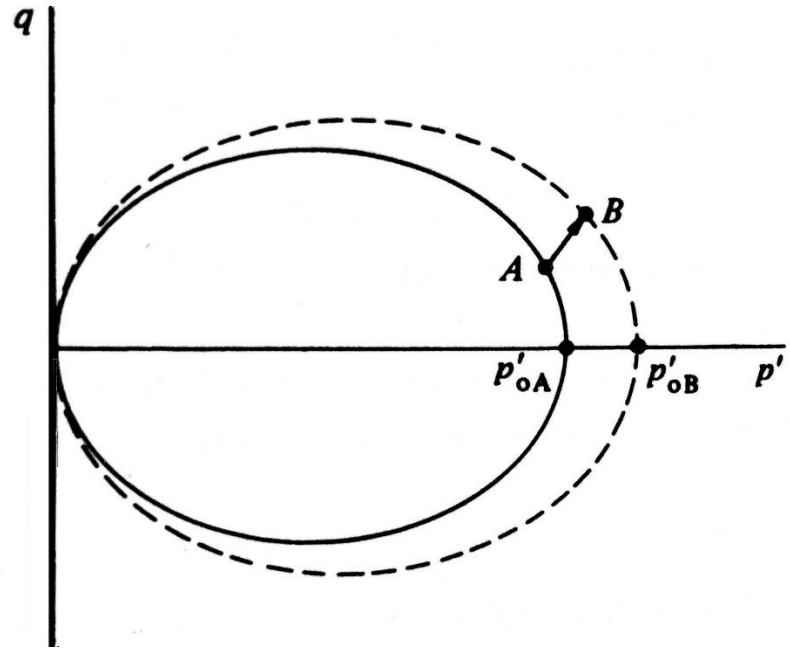

Figure 2-2: Example of expanding yield surface (Wood, 1990).

These size governing variables, p'_{oA} and p'_{oB}, are termed pre-consolidation stresses obtained from conventional isotropic consolidation tests. They represent the highest stress that the soil has experienced thus far. Therefore, this relationship is shown in the following figures:

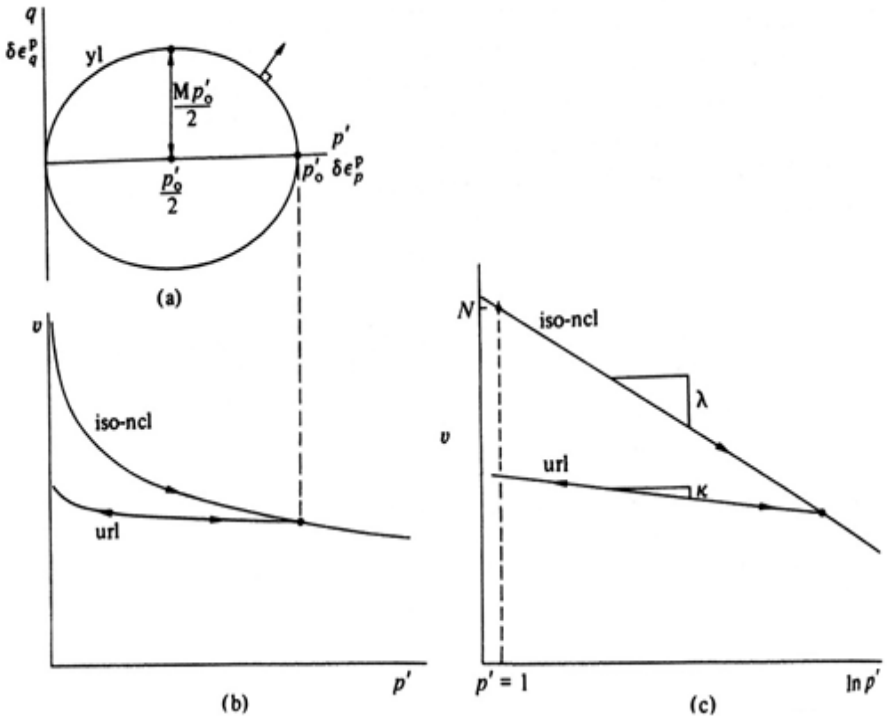

Figure 2-3: (a) Yield surface in q-p' space (b), (c) isotropic normal compression line and unload-reload line (Wood, 1990).

Furthermore, from the isotropic consolidation test shown in Figure 2-3 (c) three parameters for the Cam-Clay model can be calculated. These parameters are the slopes of the normally consolidated and unload-reload line, λ and κ, respectively, as well as the specific volume (υ = 1 + void ratio) corresponding to a reference pressure of 1 atmosphere, N. Additionally, the elliptical yield surface in Figure 2-3 (a) can be defined with the aid of Equation 2.7. When the yield surface expands, changes in p'_o, p, and q are related via Equation 2.7's differential form, which is shown in Equation 2.8 (Wood, 1990).

$$\frac{p\prime}{p\prime_o} = \frac{M^2}{M^2+\eta^2} \qquad \text{(Equation 2.7)}$$

where M = $\frac{6sin\phi}{3-sin\phi}$ or the slope between the origin and the top of the yield surface (as seen in Figure 2-3 (a)).

$$\left(\frac{M^2-\eta^2}{M^2+\eta^2}\right)\frac{\delta p\prime}{p\prime} + \left(\frac{2\eta}{M^2+\eta^2}\right)\frac{\delta q}{p\prime} - \frac{\delta p'_o}{p'_o} = 0 \qquad \text{(Equation 2.8)}$$

In the Cam-Clay model the elastic volumetric and shear strains are estimated using the following equations (Wood, 1990):

$$\delta\varepsilon_p^e = \kappa\frac{\delta p\prime}{\upsilon p\prime} \qquad \text{(Equation 2.9)}$$

$$\delta\varepsilon_q^e = \frac{\delta q}{3G\prime} \qquad \text{(Equation 2.10)}$$

The plastic volumetric and shear strains are more complex to estimate. In addition to the formula for the elliptical yield surface (*f*), another formula that describes the plastic potential (*g*) of the soil is needed. The plastic potential surface in stress space is one whose normal at any stress state defines the distribution of plastic strains in three dimensions. This surface expands in stress space and follows the stress state during plastic loading and remains fixed during unloading. In the Cam-Clay model the plasticity is associated whereby $f = g$ (Wood, 1990). Thus, it follows that the plastic volumetric and shear strains can be estimated as follows (Wood, 1990):

$$\delta\varepsilon_p^p = \chi\frac{\partial g}{\partial p\prime} \qquad \text{(Equation 2.11)}$$

$$\delta\varepsilon_q^p = \chi\frac{\partial g}{\partial q} \qquad \text{(Equation 2.12)}$$

Furthermore, the hardening rule relates the changes in these strains with the changes in the size of the yield surface (p'_o) via Equation 2.13. Then, combining Equations 2.11-2.13 with the differential form of the yield surface (Equation 2.14), the scalar multiplier χ can be solved and is shown in Equation 2.15 (Wood, 1990).

$$\delta p'_o = \frac{\partial p'_o}{\partial \varepsilon_p^p}\delta\varepsilon_p^p + \frac{\partial p'_o}{\partial \varepsilon_q^p}\delta\varepsilon_q^p \qquad \text{(Equation 2.13)}$$

$$\frac{\partial f}{\partial p'}\delta p' + \frac{\partial f}{\partial q}\delta q + \frac{\partial f}{\partial p'_o}\delta p'_o = 0 \qquad \text{(Equation 2.14)}$$

$$\chi = -\left(\frac{\partial f}{\partial p'}\delta p' + \frac{\partial f}{\partial q}\delta q\right) \Big/ \frac{\partial f}{\partial p'_o}\left(\frac{\partial p'_o}{\partial \varepsilon_p^p}\frac{\partial g}{\partial p'} + \frac{\partial p'_o}{\partial \varepsilon_q^p}\frac{\partial g}{\partial q}\right) \qquad \text{(Equation 2.15)}$$

Substituting Equation 2.15 into Equations 2.11 and 2.12, the following matrix equation can be used to estimate the incremental plastic volumetric and shear strains (Wood, 1990):

$$\begin{bmatrix}\delta\varepsilon_p^p \\ \delta\varepsilon_q^p\end{bmatrix} = \frac{-1}{\left[\frac{\partial f}{\partial p'_o}\left[\frac{\partial p'_o}{\partial \varepsilon_p^p}\frac{\partial g}{\partial p'} + \frac{\partial p'_o}{\partial \varepsilon_q^p}\frac{\partial g}{\partial q}\right]\right]}\begin{bmatrix}\frac{\partial f}{\partial p'}\frac{\partial g}{\partial p'} & \frac{\partial f}{\partial q}\frac{\partial g}{\partial p'} \\ \frac{\partial f}{\partial p'}\frac{\partial g}{\partial q} & \frac{\partial f}{\partial q}\frac{\partial g}{\partial q}\end{bmatrix}\begin{bmatrix}\delta p' \\ \delta q\end{bmatrix} \qquad \text{(Equation 2.16)}$$

However, some components are still unknown. Comparing Equations 2.8 and 2.14, and using the fact that $f = g$, the following can be found:

$$\frac{\partial f}{\partial p'} = \frac{\partial g}{\partial p'} = \left(\frac{M^2-\eta^2}{M^2+\eta^2}\right)\frac{1}{p'},\ \frac{\partial f}{\partial q} = \frac{\partial g}{\partial q} = \left(\frac{2\eta}{M^2+\eta^2}\right)\frac{1}{p'},\ and\ \frac{\partial f}{\partial p'_o} = -\frac{1}{p'_o} \qquad \text{(Equation 2.17)}$$

Additionally, from Figure 2-3 (b), Equation 2.18 can be written. The plastic volumetric strain increment can be related to the change in p'_o by combining Equations 2.18 and 2.19 to form Equation 2.20 (Wood, 1990).

$$\delta\upsilon^p = -(\lambda-\kappa)\frac{\delta p'_o}{p'_o} \qquad \text{(Equation 2.18)}$$

$$\delta\varepsilon_p^p = -\frac{\delta\upsilon}{\upsilon} \qquad \text{(Equation 2.19)}$$

$$\delta\varepsilon_p^p = [(\lambda-\kappa)/\upsilon]\frac{\delta p'_o}{p'_o} \qquad \text{(Equation 2.20)}$$

For Equations 2.13 and 2.20 to be true, the following must be assumed:

$$\frac{\partial p'_o}{\partial \varepsilon_p^p} = \frac{\upsilon p'_o}{\lambda - \kappa} \; and \; \frac{\partial p'_o}{\partial \varepsilon_q^p} = 0 \qquad \text{(Equation 2.21)}$$

Finally, the stress-strain relationship can be represented by combining Equations 2.9 and 2.10 for the elastic portion and Equations 2.16, 2.17, and 2.21 for the plastic portion as follows (Wood, 1990):

$$\begin{bmatrix} \delta \varepsilon_p^e \\ \delta \varepsilon_q^e \end{bmatrix} = \begin{bmatrix} \kappa / \upsilon p' & 0 \\ 0 & 1/3\, G' \end{bmatrix} \begin{bmatrix} \delta p' \\ \delta q \end{bmatrix} \qquad \text{(Equation 2.22)}$$

$$\begin{bmatrix} \delta \varepsilon_p^p \\ \delta \varepsilon_q^p \end{bmatrix} = \frac{\lambda - \kappa}{\upsilon p' (M^2 + \eta^2)} \begin{bmatrix} (M^2 - \eta^2) & 2\eta \\ 2\eta & 4\eta^2 / (M^2 - \eta^2) \end{bmatrix} \begin{bmatrix} \delta p' \\ \delta q \end{bmatrix} \qquad \text{(Equation 2.23)}$$

In summary, the parameters λ, κ, N and p'_o can all be found from an isotropic consolidation test. The shear modulus G' and M can be found from drained triaxial compression tests by plotting the shear stress vs shear strain and q vs p', respectively.

The stress-strain and volume change behavior of a soil can be constructed as follows: using fixed increments of p', increments of q can be found using Equation 2.7 with parameters p'_o and M. Using these increments of p' and q, Equation 2.22 can be used to predict incremental elastic strains when the stresses lie within the yield surface. Equations 2.22 and 2.23 provide the incremental plastic strains when stress excursions beyond the yield surface occur. Values of incremental stresses and strains can be added cumulatively to get the total stress and strain values. Finally, the stress-strain and volume change soil behavior can be evaluated by plotting deviatoric stress vs axial strain and volumetric strain vs axial strain, respectively.

Although the Cam-Clay model can mimic soil behavior fairly well, there are a few disadvantages. They include:

1. The influence of the intermediate principal stress cannot be completely captured when only p' and q are used to represent the state of stress.
2. If the influence of soil density is not taken into consideration, the consolidation curve in υ-ln p' space consists of only straight lines. However, it is known that actual consolidation curves do curve when transitioning from the over-consolidated to the normally consolidated state.

3. In the Cam-Clay model, the soil can only contract and dilate during strain hardening and softening, respectively. However, real soils have been observed to dilate during strain hardening. This behavior cannot be captured by the Cam-Clay model.
4. It cannot model stress path dependency on the direction of plastic strain increments. In real soil behavior, the plastic strain increment is not normal to the yield surface in σ_{ij} space. However, the Cam-Clay model assumes that the plastic strain increment is normal to the yield surface.

These factors are important to consider for this research. Hence, a more realistic soil constitutive model such as the subloading t_{ij} model, described subsequently, is needed to simulate the GRS column load test.

2.2 Subloading t_{ij} Model

As mentioned in the previous section, models that use the Cam-Clay p [= $\frac{1}{3}(\sigma_1 + 2\sigma_3)$ for triaxial compression] and q [= $\sigma_1 - \sigma_3$ for triaxial compression] stress variables cannot describe a soil's behavior when it experiences three different principal stresses. Therefore, in 1984, Nakai and Mihara formulated a Cam-Clay based elastoplastic model called the subloading t_{ij} model to consider the influence of the intermediate principal stress. This was achieved using a modified stress tensor called t_{ij} defined on a spatially mobilized plane (SMP; Nakai & Matsuoka, 1974), the orientation of which changes with change in stress instead of the octahedral plane, the orientation of which is fixed in principal stress space. Furthermore, the model includes several additional features such as incorporating the influence of density and having the ability to model stress path dependency on the direction of plastic strain increments especially when the stress state in not near or at failure. The symbols used in this model are defined as follows:

$a_{1,2,3}$	Direction cosines of normal to spatially mobilized plane (SMP)
β	Parameter (≥ 1) that controls the shape of the yield function (if $\beta = 1$ => original Cam-Clay model
δ_{ij}	Unit tensor
$d\varepsilon_N^*$	Strain increment invariant in t_{ij} concept (i.e.; normal component of $d\varepsilon_{ij}$ with respect to the SMP ($=d\varepsilon_{ij}a_{ij}$)

$d\varepsilon_S^*$	Strain increment invariant in t_{ij} concept (i.e.; in-plane component of $d\varepsilon_{ij}$ with respect to the SMP (= $\sqrt{d\varepsilon'_{ij}d\varepsilon'_{ij}}$)
$d\varepsilon_{ij}^e$	Infinitesimal increment of elastic component of strain tensor
$d\varepsilon_{ij}^p$	Infinitesimal increment of plastic component of strain tensor
$d\varepsilon_{ij}^{p(AF)}$	Infinitesimal increment of plastic component of strain tensor that satisfies the associated flow rule
$d\varepsilon_{ij}^{p(IC)}$	Infinitesimal increment of plastic component of strain tensor under increasing mean stress
e_0	Initial void ratio
e_{ijk}	Permutation tensor
E_e	Tangential Young's modulus of the elastic component
$(-\Delta e)^p$	Plastic component of finite change in void ratio
F	Stress term in the yield function $(= (\lambda-\kappa) ln\frac{\sigma}{\sigma_0}, (\lambda-\kappa) ln\frac{p_1}{p_0}, or\ (\lambda-\kappa) ln\frac{t_{N1}}{t_{N0}})$
G(ρ)	Increasing function of ρ that satisfies G(0)=0
H	Plastic strain term in yield function $(= (-\Delta e)^p = (1+e_0)d\varepsilon_v^p)$
$I_{1,2,3}$	First, second, and third invariants of σ_{ij}
$I_{r1,2,3}$	First, second, and third invariants of r_{ij} (where $r_{ik}r_{kj} = \sigma_{ij}$)
Λ	Proportional constant $(= \frac{dF}{h^p}\ or\ \frac{dF+d\psi}{h^p})$
$\langle\Lambda\rangle$	< > are Macaulay brackets that make <A> = A if A > 0 but <A> = 0 if otherwise
$\Lambda^{(AF)}$	Proportional constant component that satisfies the associated flow rule
$\Lambda^{(IC)}$	Proportional constant component under increasing mean stress
M*	Intercept with X-axis in stress-dilatancy relations based on the t_{ij} concept; determined from X_{CS} and Y_{CS}
υ_e	Elastic component of Poisson's ratio
ϕ_{moij}	Mobilized angle between two principal stresses (σ_i and σ_j)
r_{ij}	Square root of σ_{ij} (i.e. $r_{ik}r_{kj} = \sigma_{ij}$)

R_{cs}	Principal stress ratio at critical state in triaxial compression ($= (\sigma_1/\sigma_3)_{CS(Comp)}$)
ρ	State variable representing density; difference between the current void ratio and the void ratio on the NCL at the same stress level
t_{ij}	Modified stress tensor based on the t_{ij} concept ($= a_{ik}\sigma_{kj}$)
$t_{1,2,3}$	Principal value of t_{ij}
t_N	Stress invariant in the t_{ij} concept (i.e. normal component of t_{ij} with respect to the SMP ($= t_{ij}a_{ij}$))
t_s	Stress invariant in the t_{ij} concept (i.e. in-plane component of t_{ij} with respect to the SMP ($= \sqrt{t'_{ij}t'_{ij}}$))
$t_{N0,1}$	Value of t_N on t_N-axis for the current yield surface
x_{ij}	Stress ratio tensor based on tij concept ($= \frac{t'_{ij}}{t_N}$)
X	Stress ratio ($= \frac{t_s}{t_N} = \sqrt{x_{ij}x_{ij}}$)
X_{cs}	Stress ratio at critical state
Y_{cs}	Plastic strain increment ratio ($=d\varepsilon_N^{*p}/ d\varepsilon_S^{*p}$) at critical state

In the Cam-Clay model, stresses are defined on the octahedral plane where it is assumed that either $\sigma_2 = \sigma_3$ (triaxial compression) or $\sigma_2 = \sigma_1$ (triaxial extension). In the subloading t_{ij} model, stresses are defined on a spatially mobilized plane (SMP) where σ_2 is not limited to being σ_1 or σ_3 only. σ_2 can take on any number and that value is uniquely represented on the SMP. The advantage of doing so is that the subloading t_{ij} model can account for the effects of the intermediate principal stress.

The SMP in 3D stress space where the axes are the principal stresses, is shown in Figure 2-4 (a). Each SMP side has a shear-stress ratio that is maximized by using the Mohr circles in Figure 2-4(b).

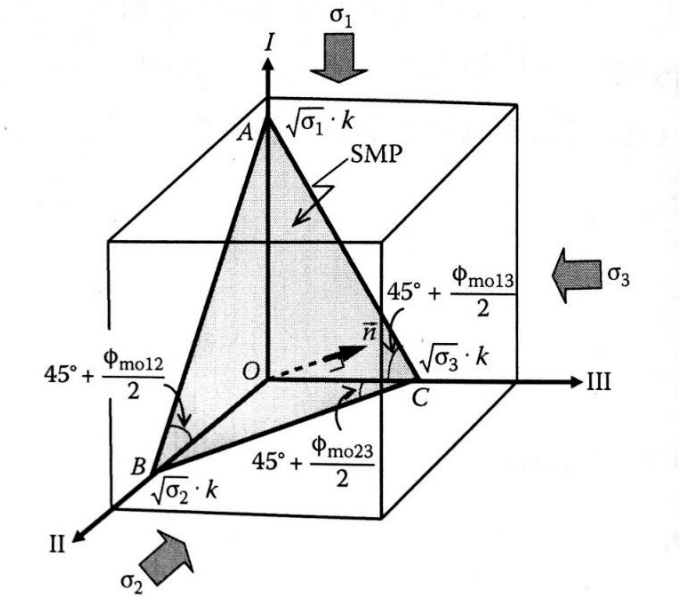

(a)

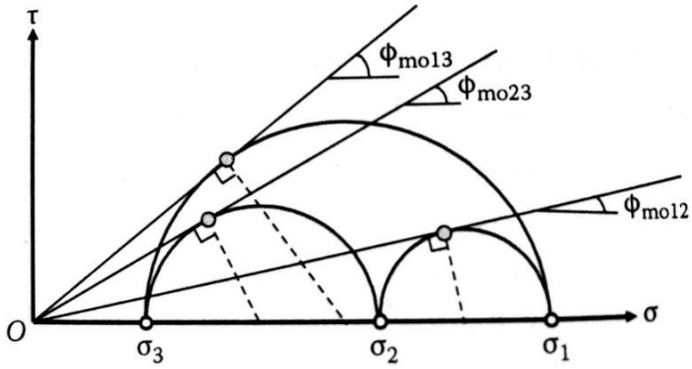

(b)

Figure 2-4: (a) SMP in 3D stress space (b) Mohr circles for three different principal stresses (Nakai and Matsuoka, 1974).

Furthermore, as shown in Figure 2-4(a) and (b), the following equation holds true for the values at the intersection of the axes and the SMP:

$$\tan\left(45° + \frac{\phi_{moij}}{2}\right) = \sqrt{\frac{1+sin\phi_{moij}}{1-sin\phi_{moij}}} = \sqrt{\frac{\sigma_i}{\sigma_j}}\ (i,j = 1,2,3; i < j) \qquad \text{(Equation 2.24)}$$

Therefore, the SMP becomes the octahedral plane when the soil is under an isotropic state of stress but it deviates from the octahedral plane with changes in stress ratio. Additionally, the direction cosines (a_1, a_2, and a_3) of the normal vector to the SMP are related to components of the model's stress tensor (σ_{ij}) and stress invariants (I_1, I_2, and I_3) as follows (Nakai, 1989):

$$a_1 = \sqrt{\frac{I_3}{I_2\sigma_1}}, a_2 = \sqrt{\frac{I_3}{I_2\sigma_2}}, a_3 = \sqrt{\frac{I_3}{I_2\sigma_3}} \ (Note: a_1^2 + a_2^2 + a_3^2 = 1) \quad \text{(Equation 2.25)}$$

The matrix of direction cosines and the unit tensor (δ_{ij}) are related through the square root stress tensor (r_{ij}), and r_{ij} invariants (I_{r1}, I_{r2}, and I_{r3}) as follows (Nakai, 1989):

$$a_{ij} = \sqrt{\frac{I_3}{I_2}} \cdot r_{ij}{}^{-1} = \sqrt{\frac{I_3}{I_2}} \cdot (\sigma_{ik} + I_{r2}\delta_{ik})(I_{r1}\sigma_{kj} + I_{r3}\delta_{kj})^{-1} \quad \text{(Equation 2.26)}$$

where $I_1 = \sigma_1 + \sigma_2 + \sigma_3$, $I_2 = \sigma_1\sigma_2 + \sigma_2\sigma_3 + \sigma_3\sigma_1$, $I_3 = \sigma_1\sigma_2\sigma_3$, $I_{r1} = \sqrt{\sigma_1} + \sqrt{\sigma_2} + \sqrt{\sigma_3}$, $I_{r2} = \sqrt{\sigma_1\sigma_2} + \sqrt{\sigma_2\sigma_3} + \sqrt{\sigma_3\sigma_1}$, and $I_{r3} = \sqrt{\sigma_1\sigma_2\sigma_3}$.

Nakai and Mihara (1984) defined the t_{ij} tensor to be equal to the product of a_{ik} and σ_{kj} with the following principal values of t_{ij}: $t_1 = a_1\sigma_1$, $t_2 = a_2\sigma_2$, and $t_3 = a_3\sigma_3$.

Including the effects of the intermediate principal stress this way, the subloading t_{ij} model can now be used to simplify the stresses and strains similar to the Cam-Clay model by having two stress variables, t_N and t_s, and two strain variables, $d\varepsilon_N^*$ and $d\varepsilon_S^*$. Furthermore, these stress and strain variables are normal and in-plane to the SMP, instead of the octahedral plane. The variables that are normal to the SMP are t_N and $d\varepsilon_N^*$ while the variables in-plane are t_s and $d\varepsilon_S^*$. These can be seen in Figure 2-5 (a) and (b).

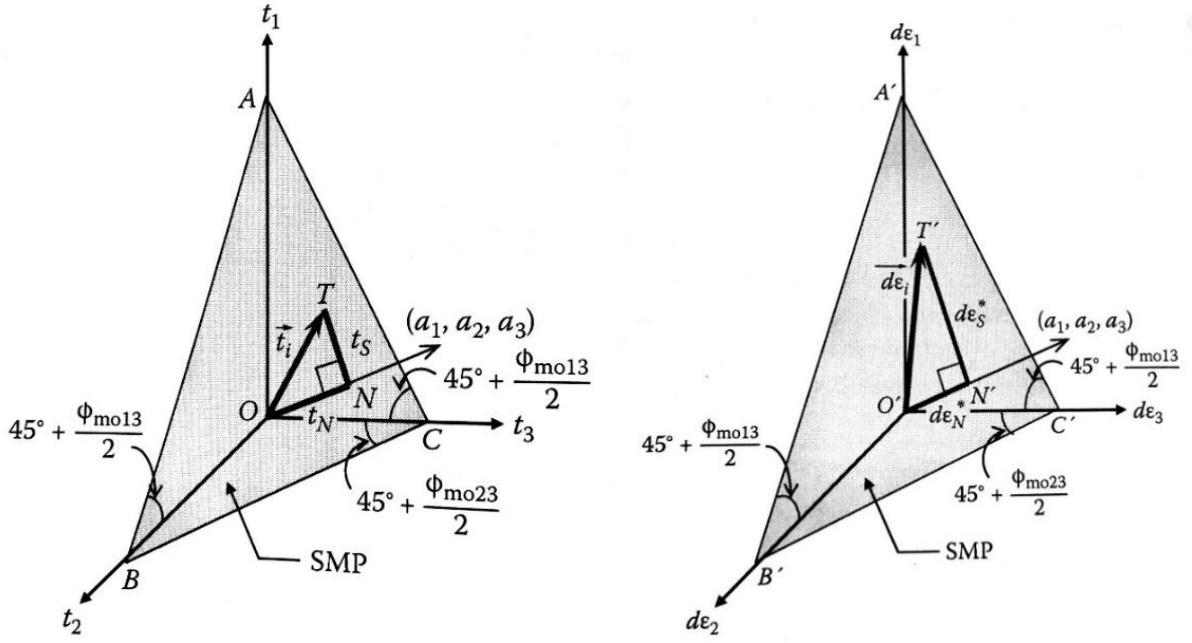

Figure 2-5: SMP with: (a) t_N and t_S stress variables (b) $d\varepsilon_N^*$ and $d\varepsilon_S^*$ strain variables.

From Figure 2-5 (a) and (b), the following equations can be formulated:

$$t_N = t_{ij}a_{ij} = 3\frac{I_3}{I_2} \quad \text{(Equation 2.27)}$$

$$t_S = \sqrt{t_{ij}t_{ij} - (t_{ij}a_{ij})^2} \quad \text{(Equation 2.28)}$$

$$d\varepsilon_N^* = d\varepsilon_{ij}a_{ij} \quad \text{(Equation 2.29)}$$

$$d\varepsilon_S^* = \sqrt{d\varepsilon_{ij}d\varepsilon_{ij} - (d\varepsilon_{ij}a_{ij})^2} \quad \text{(Equation 2.30)}$$

$$X = \frac{t_S}{t_N} = \frac{2}{3}\sqrt{\frac{(\sigma_1-\sigma_2)^2}{4\sigma_1\sigma_2} + \frac{(\sigma_2-\sigma_3)^2}{4\sigma_2\sigma_3} + \frac{(\sigma_3-\sigma_1)^2}{4\sigma_3\sigma_1}} = \sqrt{\frac{I_1I_2}{9I_3} - 1} \quad \text{(Equation 2.31)}$$

Analogous to the stress ratio η = q/p in the Cam-Clay model, the subloading t_{ij} model uses $X=t_S/t_N$. Furthermore, when X = constant, the following criterion is true for the three stress invariants of σ_{ij}:

$$\frac{I_1I_2}{I_3} = const. \quad \text{(Equation 2.32)}$$

Compared to the von Mises and Mohr-Coulomb failure criteria on the octahedral plane in principal stress space, the SMP failure criterion plots as shown in Figure 2-6:

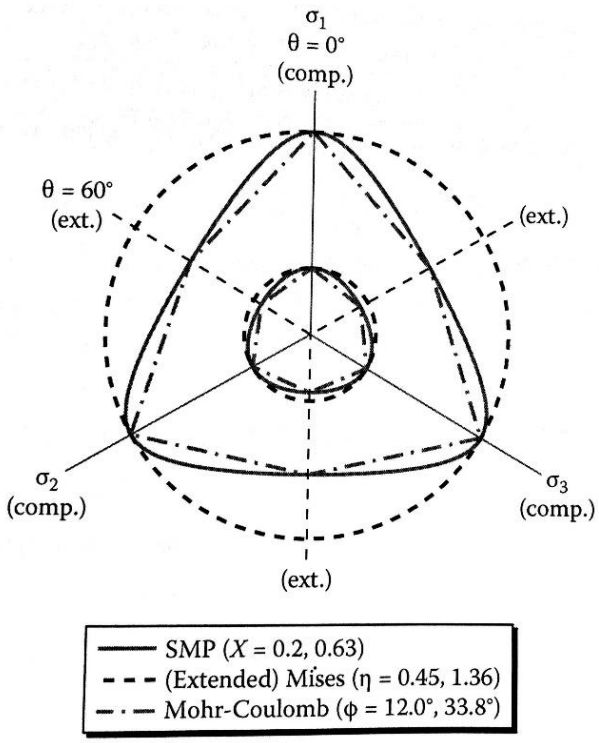

Figure 2-6: SMP, von Mises, and Mohr-Coulomb criteria on the octahedral plane in principal stress space (Nakai and Matsuoka, 1974).

As seen in Figure 2-6, the SMP failure criterion plots as a rounded triangle that coincides with all other failure criteria during triaxial compression and extension.

Using the t_{ij} concept, the soil stress-strain and volume change behavior can be estimated by replacing the p and q stress variables from the Cam-Clay model with t_N and t_S. This is done by first, defining the yield surface with t_N and t_S instead of p and q (Figure 2.7).

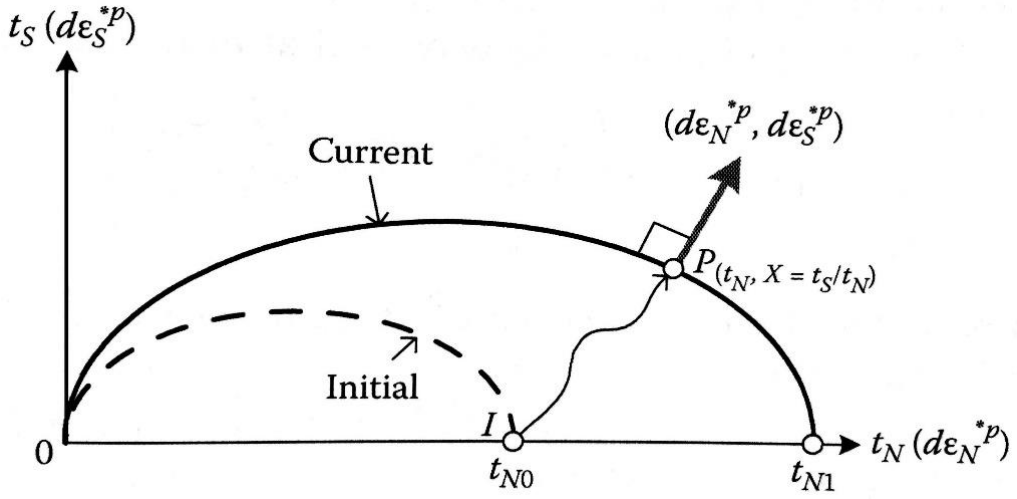

Figure 2-7: Yield surface in t_{ij} space (Nakai, 2013).

In Figure 2-7, t_{N0} and t_{N1} are analogous to the pre-consolidation stresses p'_{0A} and p'_{0B} in Figure 2-2. Therefore, with this yield surface, the stress term in the yield function, F (this is akin to a yield function), and the plastic strain term in the yield function, H (this is akin to a plastic potential function), in the subloading t_{ij} model were defined by Nakai (2013) as follows:

$$F = (\lambda - \kappa)\ln\left(\frac{t_{N1}}{t_{N0}}\right) = (\lambda - \kappa)\left\{\ln\left(\frac{t_N}{t_{N0}} + \frac{1}{\beta}\left(\frac{X}{M^*}\right)^{\beta}\right)\right\} \qquad \text{(Equation 2.33)}$$

$$\text{and } H = (1 + e_0)\varepsilon_v^p \qquad \text{(Equation 2.34)}$$

where β = is a parameter that controls the shape of the yield function, $M^* = \left(X_{CS}^{\beta} + X_{CS}^{\beta-1}Y_{CS}\right)^{1/\beta}, X_{CS} = \frac{\sqrt{2}}{3}\left(\sqrt{R_{CS}} - \frac{1}{\sqrt{R_{CS}}}\right), Y_{CS} = \frac{1-\sqrt{R_{CS}}}{\sqrt{2}(\sqrt{R_{CS}}+0.5)}, and\ R_{CS} = (\sigma_1/\sigma_3)_{CS}$. If β = 1, the subloading t_{ij} model becomes the original Cam-Clay model.

However, since the plasticity is associated,

$$F = H \Rightarrow (\lambda - \kappa)\left\{\ln\left(\frac{t_N}{t_{N0}} + \frac{1}{\beta}\left(\frac{X}{M^*}\right)^{\beta}\right)\right\} = (1 + e_0)\varepsilon_v^p \qquad \text{(Equation 2.35)}$$

The subloading t_{ij} model uses the following flow rule to find the magnitude of the plastic strains (Nakai, 2013):

$$d\varepsilon_{ij}^p = \Lambda\frac{\partial F}{\partial t_{ij}} = \Lambda\left(\frac{\partial F}{\partial t_N}\frac{\partial t_N}{\partial t_{ij}} + \frac{\partial F}{\partial X}\frac{\partial X}{\partial t_{ij}}\right) \qquad \text{(Equation 2.36)}$$

As shown in Equation 2.36, there is a constant (Λ) similar to Cam-Clay model's scalar multiplier, χ. This was termed the proportionality constant and it is defined with the following process:

$H = (1 + e_0)\varepsilon_v^p$

- ⇨ $dH = (1 + e_0)\Lambda\frac{\partial F}{\partial t_{kk}}$
- ⇨ Plasticity is associated, $dF = dH$
- ⇨ $dF = (1 + e_0)\Lambda\frac{\partial F}{\partial t_{kk}}$

$$\therefore \Lambda = \frac{dF}{(1+e_0)\frac{\partial F}{\partial t_{kk}}}\left[where\ dF = \frac{\partial F}{\partial \sigma_{ij}}d\sigma_{ij}\right] \qquad \text{(Equation 2.37)}$$

Consequently, in Equation 2.36, partial derivatives of F with respect to t_N and X (see Equation 2.33) and of t_N with respect to t_{ij} (see Equation 2.27) are required as shown in equations 2.38 through 2.40 (Nakai, 2013):

$$\frac{\partial F}{\partial t_N} = (\lambda - \kappa)\frac{1}{t_N} \quad \text{(Equation 2.38)}$$

$$\frac{\partial F}{\partial X} = (\lambda - \kappa)X^{\beta-1} \quad \text{(Equation 2.39)}$$

$$\frac{\partial t_N}{\partial t_{ij}} = \frac{\partial (t_{kl}a_{kl})}{\partial t_{ij}} = a_{ij} \quad \text{(Equation 2.40)}$$

Then taking partial derivatives of X with respect to t_{ij} and x_{kl} yield equations 2.41 and 2.42.

$$\frac{\partial X}{\partial t_{ij}} = \frac{\partial (\sqrt{x_{mm}x_{mm}})}{\partial x_{kl}}\frac{\partial x_{kl}}{\partial t_{ij}} = \frac{1}{X \cdot t_N}(x_{ij} - X^2 a_{ij}) \quad \text{(Equation 2.41)}$$

$$\frac{\partial X}{\partial x_{kl}} = \frac{\partial (\sqrt{x_{mm}x_{mm}})}{\partial x_{kl}} = \frac{x_{kl}}{X} \quad \text{(Equation 2.42)}$$

where $$x_{ij} = \frac{t'_{ij}}{t_N} = \frac{t_{ij} - t_N a_{ij}}{t_N} = \frac{t_{ij}}{t_N} - a_{ij} \quad \text{(Equation 2.43)}$$

In Equation 2.41, the partial derivative of x_{kl} (Equation 2.43) with respect to t_{ij} is needed and is shown as follows:

$$\frac{\partial x_{kl}}{\partial t_{ij}} = \frac{\partial}{\partial t_{ij}}\left(\frac{t_{kl}}{t_N} - a_{kl}\right) = \frac{1}{t_N}\{\delta_{ik}\delta_{jl} - (x_{kl} + a_{kl})a_{ij}\} \quad \text{(Equation 2.44)}$$

Furthermore, in Equation 2.37, the partial derivative of F with respect to σ_{ij} is required, which is defined as follows (Nakai, 2013):

$$\frac{\partial F}{\partial \sigma_{ij}} = \frac{\partial F}{\partial t_N}\frac{\partial t_N}{\partial \sigma_{ij}} + \frac{\partial F}{\partial X}\frac{\partial X}{\partial \sigma_{ij}} \quad \text{(Equation 2.45)}$$

Therefore, the partial derivatives in Equation 2.45 that are not defined yet include the partial derivatives of t_N with respect to σ_{ij} and of X with respect to σ_{ij}. They can be derived from equations 2.27 and 2.31 as follows:

$$\frac{\partial t_N}{\partial \sigma_{ij}} = \frac{\partial}{\partial \sigma_{ij}}\left(3\frac{I_3}{I_2}\right) = -3\frac{I_3}{I_2^2}\frac{\partial I_2}{\partial \sigma_{ij}} + 3\frac{1}{I_2}\frac{\partial I_3}{\partial \sigma_{ij}} \quad \text{(Equation 2.46)}$$

$$\frac{\partial X}{\partial \sigma_{ij}} = \frac{\partial}{\partial \sigma_{ij}}\left(\sqrt{\frac{I_1 I_2}{9I_3} - 1}\right) = \frac{1}{2X}\left(\frac{I_2}{9I_3}\frac{\partial I_1}{\partial \sigma_{ij}} + \frac{I_1}{9I_3}\frac{\partial I_2}{\partial \sigma_{ij}} - \frac{I_1 I_2}{9I_3^2}\frac{\partial I_3}{\partial \sigma_{ij}}\right) \quad \text{(Equation 2.47)}$$

In equations 2.46 and 2.47, the following terms are needed:

$$\frac{\partial I_1}{\partial \sigma_{ij}} = \frac{\partial \sigma_{kk}}{\partial \sigma_{ij}} = \delta_{ij} \quad \text{(Equation 2.48)}$$

$$\frac{\partial I_2}{\partial \sigma_{ij}} = \frac{\partial}{\partial \sigma_{ij}}\left(\frac{(\sigma_{kk})^2 - \sigma_{lm}\sigma_{ml}}{2}\right) = \sigma_{kk}\delta_{ij} - \sigma_{ij} \quad \text{(Equation 2.49)}$$

$$\frac{\partial I_3}{\partial \sigma_{ij}} = \frac{\partial}{\partial \sigma_{ij}}\left(\frac{e_{klm}e_{opq}\sigma_{ko}\sigma_{lp}\sigma_{mq}}{6}\right) = \frac{1}{2}e_{ilm}e_{jpq}\sigma_{lp}\sigma_{mq} \quad \text{(Equation 2.50)}$$

Lastly, the elastic stress-strain relationship for the subloading t_{ij} model uses the generalized Hooke's Law modified with the t_{ij} concept, which is shown as follows (Nakai, 2013):

$$d\varepsilon_{ij}^{e} = \frac{1+\upsilon_e}{E_e} d\left(\frac{\sigma_{ij}}{1+X^2}\right) - \frac{\upsilon_e}{E_e} d\left(\frac{\sigma_{mm}}{1+X^2}\right)\delta_{ij} \quad \text{(Equation 2.51)}$$

where $$E_e = \frac{3(1-2\upsilon_e)(1+e_0)t_N}{\kappa} \quad \text{(Equation 2.52)}$$

As with the Cam-Clay model, the subloading t_{ij} model uses the elastic stress-strain relationship when the stresses remain within the yield surface in t_{ij} space. However, once the state of stress reaches the yield surface, the elastic and plastic strains are superimposed.

In addition to considering the intermediate principal stress, the subloading t_{ij} model can also introduce a curvature to the recompression line by considering the influence of density (ρ). Once the recompression line is curved, the strains are no longer purely elastic. Plastic strains are introduced. Physically, ρ represents the soil's vertical offset from the NCL. For non-structured soils, ρ is typically ≥ 0 and usually decreases as the loading approaches the normally consolidated line from an overconsolidated state. From Figure 2-8, Equation 2.53 can be derived to estimate the change in void ratio due to plastic straining in overconsolidated soils:

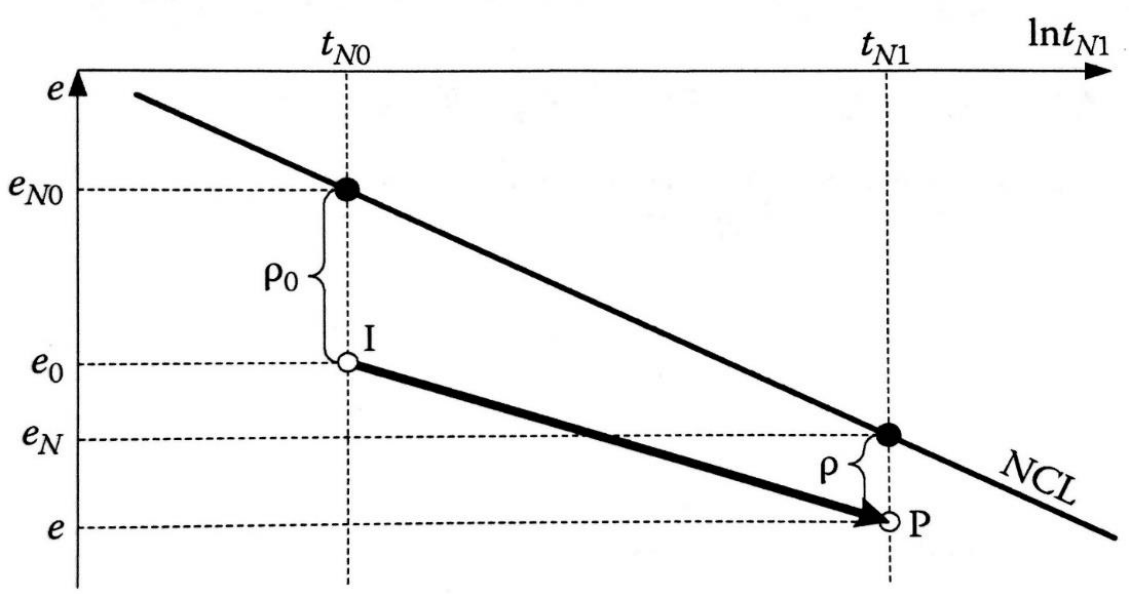

Figure 2-8: Change in plastic void ratio for an overconsolidated soil (Nakai, 2013).

$$(-\Delta e)^p = (\lambda - \kappa) \ln\left(\frac{t_{N1}}{t_{N0}}\right) - (\rho_0 - \rho) \qquad \text{(Equation 2.53)}$$

To include the influence of density, the relationship between the yield and plastic potential functions is modified as follows:

$$f = F - \{H + (\rho_0 - \rho)\} = 0$$

Imposing the consistency condition df = 0 yields:

$$df = dF - \{dH - d\rho\} = 0$$

Introducing the flow rule (Equation 2.36) yields:

$$df = dF - \left\{(1 + e_0)\Lambda \frac{\partial F}{\partial t_{ii}} - d\rho\right\} = 0 \qquad \text{(Equation 2.54)}$$

Note that for dρ to be dimensionless like dF and dH, the proportionality constant, Λ, must have the same dimensions as stress, while the derivative $\partial F/\partial t_{ii}$ has the dimensions of the inverse of stress. Therefore, the following expression for dρ satisfies the above conditions (Nakai, 2013):

$$d\rho = -(1 + e_0)\frac{G(\rho)}{t_N}\Lambda$$

Substituting it back into Equation 2.54 yields the proportionality constant that considers the influence of density:

$$df = dF - \left\{(1+e_0)\Lambda\frac{\partial F}{\partial t_{ii}} + (1+e_0)\frac{G(\rho)}{t_N}\Lambda\right\} = 0$$

$$\therefore \Lambda = \frac{dF}{(1+e_0)\left\{\frac{\partial F}{\partial t_{ii}}+\frac{G(\rho)}{t_N}\right\}} \qquad \text{(Equation 2.55)}$$

where G(ρ) is a monotonically increasing function that satisfies G(0)=0. For simplicity, it is usually defined as either $G(\rho) = a\rho$, $G(\rho) = a\sqrt{\rho}$ or $G(\rho) = a\rho^2$. Additionally, $dF = \frac{\partial F}{\partial \sigma_{kl}} d\sigma_{kl}$.

As a result, the plastic strain increment shown in Equations 2.36 can now be modified by replacing the proportionality constant (Λ) with the right hand side of Equation 2.55, and invoking the loading criterion where if $\Lambda > 0$, then $d\varepsilon_{ij}^p \neq 0$ and if $\Lambda \leq 0$, then $d\varepsilon_{ij}^p = 0$. The resulting equation is as follows:

$$d\varepsilon_{ij}^p = \langle\Lambda\rangle\frac{\partial F}{\partial t_{ij}} = \left\langle\frac{dF}{(1+e_0)\left\{\frac{\partial F}{\partial t_{ii}}+\frac{G(\rho)}{t_N}\right\}}\right\rangle\frac{\partial F}{\partial t_{ij}} \qquad \text{(Equation 2.56)}$$

where < > are Macaulay brackets that make <Λ> = Λ if Λ > 0 but <Λ> = 0 otherwise.

The elastic strain increment is estimated the same way using Equations 2.51 and 2.52.

The subloading t_{ij} model also accounts for the fact that the direction of plastic strain increment is dependent on the stress path. This consideration is important because many models inherently assume that the direction of plastic strain increment is independent of the stress path, and thus the stress-dilatancy relation is thought to be not affected by the stress path. However, Tatsuoka (1978) experimentally showed that the stress-dilatancy relation does depend on the stress path even during the early stages of loading in figures 2-9 (q/p vs $d\varepsilon_v/d\varepsilon_d$) and 2-10 ($t_S/t_N$ vs $d\varepsilon_N^*/ d\varepsilon_S^*$) for normally consolidated clay and medium dense sand, respectively.

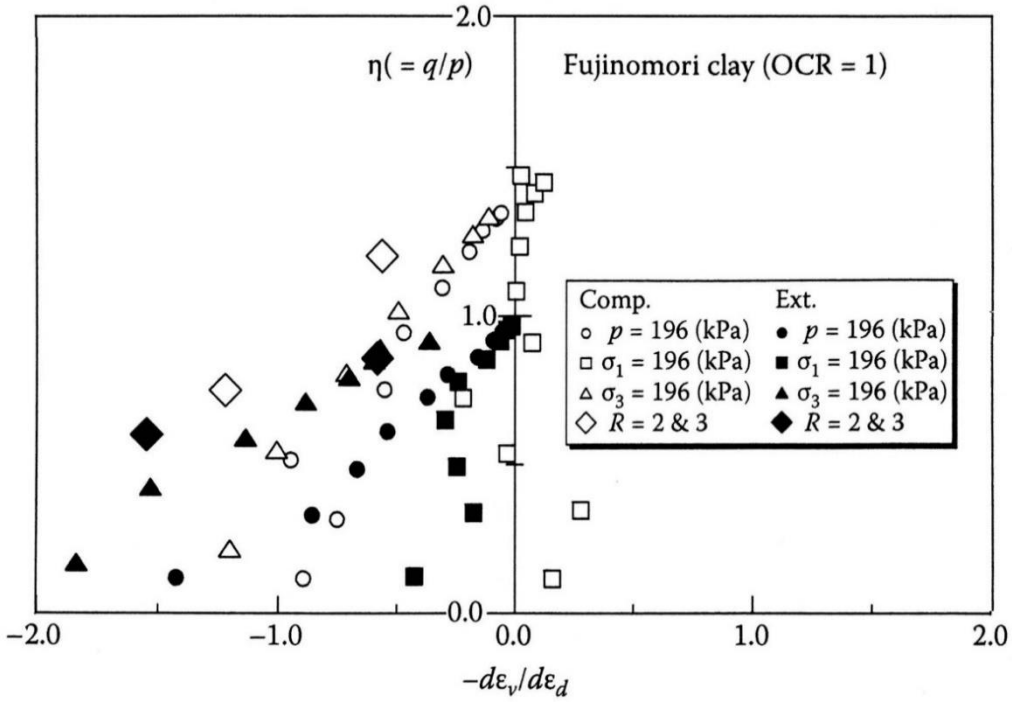

(a) Normally consolidated clay

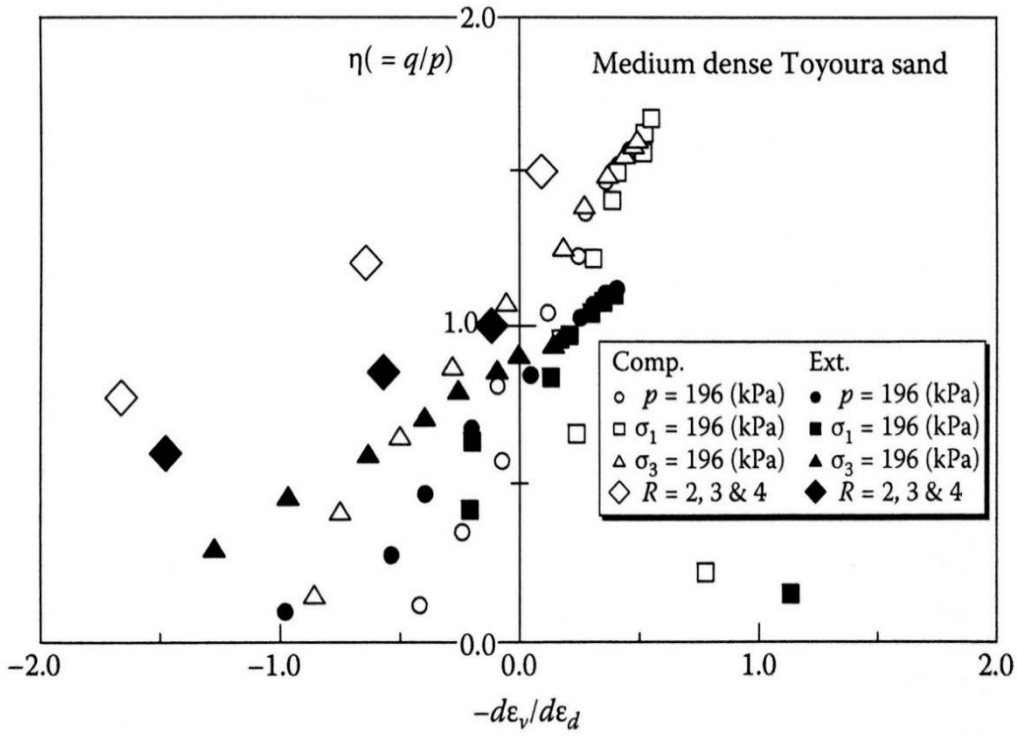

(b) Medium dense sand

Figure 2-9: q/p vs $d\varepsilon_v/d\varepsilon_d$ to show dependency of direction of plastic strain increment on stress path (Tatsuoka, 1978).

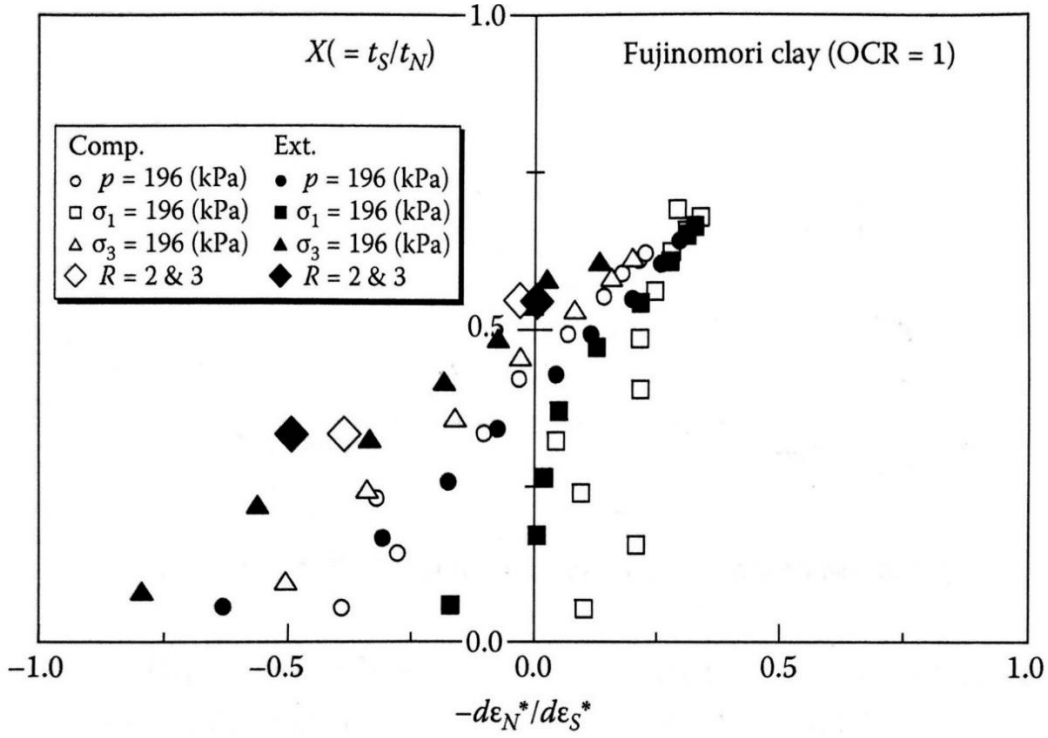

(a) Normally consolidated clay

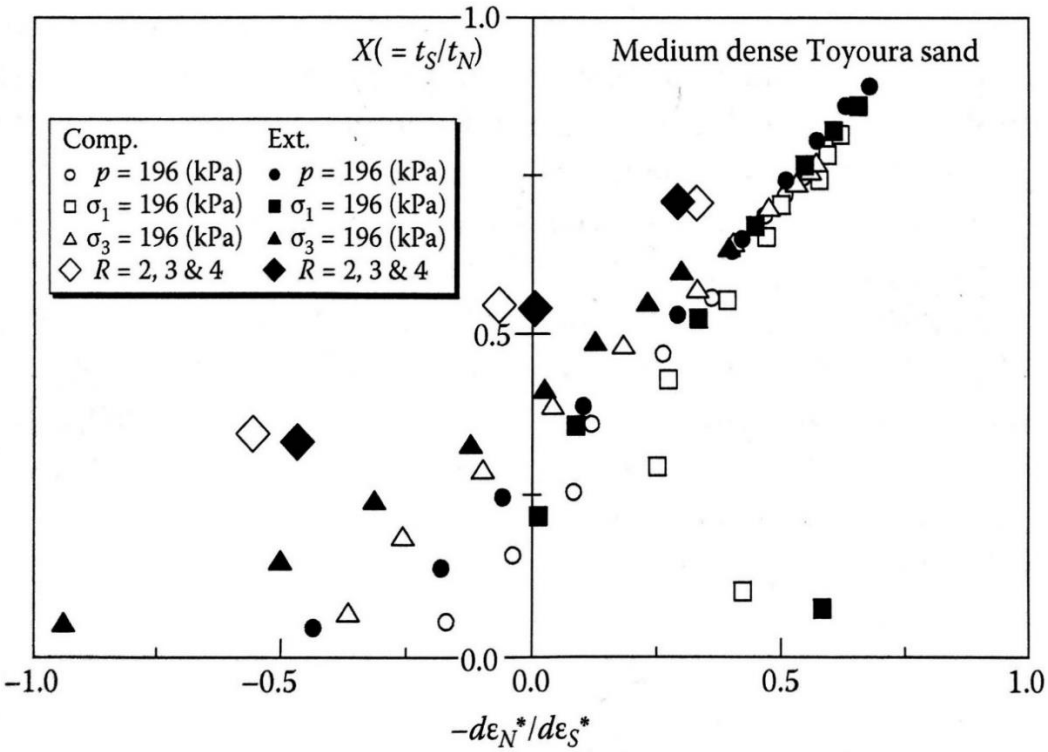

(b) Medium dense sand

Figure 2-10: t_S/t_N vs $d\varepsilon_N^*/ d\varepsilon_S^*$ to show dependency of direction of plastic strain increment on stress path (Tatsuoka, 1978).

The plastic strain increment can be decomposed into an "associated flow rule" component that is normal to the yield surface $d\varepsilon_{ij}^{p(AF)}$ and an isotropic compression component $d\varepsilon_{ij}^{p(IC)}$. As seen in Figure 2-11, when $d\varepsilon_{ij}^{p(AF)}$, given by Equation 2.56, has a negative slope (i.e.; when the state of stress moves towards region II), $dF > 0$, $dt_N \leq 0$, and $d\varepsilon_{ij}^{p(IC)} = 0$. When $d\varepsilon_{ij}^{p(AF)}$ has a positive slope (i.e.; when the state of stress moves towards region III), $dF > 0$, $dt_N > 0$, and both $d\varepsilon_{ij}^{p(AF)}$ and $d\varepsilon_{ij}^{p(IC)}$ are non-zero (Nakai, 2013).

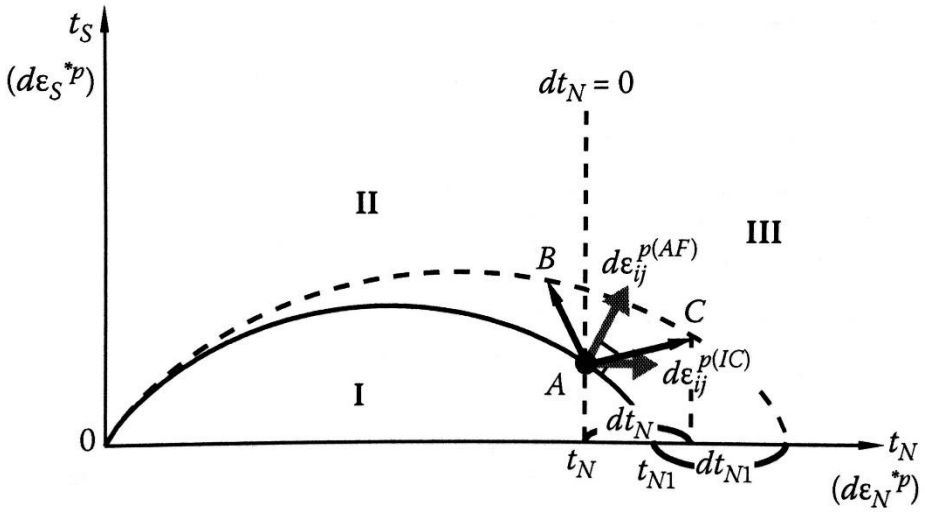

Figure 2-11: Yield surface showing the plastic strain components $d\varepsilon_{ij}^{p(AF)}$ and $d\varepsilon_{ij}^{p(IC)}$ (Nakai, 2013).

During isotropic compression, there are no shear stresses. Therefore, $t_S = X = 0$ and $d\varepsilon_{ij}^{p(IC)}$ can be derived as follows (Nakai, 2013):

$$d\varepsilon_v^p = d\varepsilon_{ii}^p = \Lambda \frac{\partial F}{\partial t_{ii}} = \frac{dF}{(1+e_0)\left\{\frac{\partial F}{\partial t_{kk}} + \frac{G(\rho)}{t_N}\right\}} \cdot \frac{\partial F}{\partial t_{ii}}$$

During isotropic compression, $t_{N1} = t_N = p$ and $\frac{\partial F}{\partial t_{ii}} = \frac{\lambda-\kappa}{t_N} a_{ii}$:

$$\Rightarrow \quad d\varepsilon_v^p = \frac{\lambda-\kappa}{(1+e_0)\left\{1+\frac{G(\rho)}{(\lambda-\kappa)a_{ii}}\right\}} \cdot \frac{dt_N}{t_N}$$

When $t_N > 0$, and the isotropic compression component of the plastic strain increment $d\varepsilon_{ij}^{p(IC)}$ is a fraction (t_N/t_{N1}) of $d\varepsilon_v^p$. Hence, $d\varepsilon_{ij}^{p(IC)}$ can be written as:

$$\Rightarrow \quad d\varepsilon_{ij}^{p(IC)} = \Lambda^{(IC)} \frac{\delta_{ij}}{3} = \frac{\lambda-\kappa}{(1+e_0)\left\{1+\frac{G(\rho)}{(\lambda-\kappa)a_{kk}}\right\}} \cdot \frac{\langle dt_N \rangle}{t_N} \cdot \frac{t_N}{t_{N1}} \cdot \frac{\delta_{ij}}{3}$$

As shown in Equation 2.33, $t_{N1} = t_N \cdot \exp\left(\frac{1}{\beta}\left(\frac{X}{M^*}\right)^{\beta}\right)$:

$$\Rightarrow \quad d\varepsilon_{ij}^{p(IC)} = \Lambda^{(IC)} \frac{\delta_{ij}}{3} = \frac{\lambda-\kappa}{(1+e_0)\left\{1+\frac{G(\rho)}{(\lambda-\kappa)a_{kk}}\right\}} \cdot \frac{\langle dt_N \rangle}{t_N} \cdot \frac{t_N}{t_N \cdot \exp\left(\frac{1}{\beta}\left(\frac{X}{M^*}\right)^{\beta}\right)} \cdot \frac{\delta_{ij}}{3}$$

$$\therefore d\varepsilon_{ij}^{p(IC)} = \frac{\frac{(\lambda-\kappa)\langle dt_N \rangle}{t_N \cdot \exp\left(\frac{1}{\beta}\left(\frac{X}{M^*}\right)^{\beta}\right)}}{(1+e_0)\left\{1+\frac{G(\rho)}{(\lambda-\kappa)a_{kk}}\right\}} \cdot \frac{\delta_{ij}}{3} \qquad \text{(Equation 2.57)}$$

Finally, the proportionality constant for the AF term for the plastic strain increment can be derived as shown in Equation 2.58.

$$\Lambda^{(AF)} = \frac{dF - \frac{\lambda-\kappa}{t_N \cdot \exp\left(\frac{1}{\beta}\left(\frac{X}{M^*}\right)^{\beta}\right)}\langle dt_N \rangle}{(1+e_0)\left(\frac{\partial F}{\partial t_{kk}} + \frac{G(\rho)}{t_N}\right)} \qquad \text{(Equation 2.58)}$$

Substituting Equation 2.58 into Equation 2.56, yields the following expression for $d\varepsilon_{ij}^{p(AF)}$ (Nakai, 2013).

$$d\varepsilon_{ij}^{p(AF)} = \Lambda^{(AF)} \cdot \frac{\partial F}{\partial t_{ij}} = \frac{dF - \frac{\lambda-\kappa}{t_N \cdot \exp\left(\frac{1}{\beta}\left(\frac{X}{M^*}\right)^{\beta}\right)}\langle dt_N \rangle}{(1+e_0)\left(\frac{\partial F}{\partial t_{kk}} + \frac{G(\rho)}{t_N}\right)} \cdot \frac{\partial F}{\partial t_{ij}} \qquad \text{(Equation 2.59)}$$

where $dF = \frac{\partial F}{\partial \sigma_{mm}} d\sigma_{mm}$.

In summary, the subloading t_{ij} model utilizes the same input parameters as the Cam-Clay model. Additionally, the subloading t_{ij} model uses fitting parameters to optimize the agreement between measured and calculated stress-strain and volume change curves. These fitting parameters are the influence of density parameter (a) and the yield surface shape parameter (β).

The subloading t_{ij} model utilizes a parameter R_{cs} instead of M as used in the Cam-Clay model. R_{cs} is defined as:

$$R_{CS} = (\sigma_1/\sigma_3)_{CS(Comp)} \qquad \text{(Equation 2.60)}$$

In fact, the two are related as follows:

$$R_{CS} = \frac{2M+3}{3-M} \qquad \text{(Equation 2.61)}$$

To summarize, the stress-strain relationship for the subloading t_{ij} model can be obtained for each region as follows (Nakai, 2013):

1. Elastic region $(dF < 0)$:

   $$d\varepsilon_{ij} = d\varepsilon_{ij}^{e} = \frac{1+\upsilon_e}{E_e} d\sigma_{ij} - \frac{\upsilon_e}{E_e} d\sigma_{mm}\delta_{ij}$$

2. Elastoplastic region with strain hardening $(dF > 0 \; and \; dt_N > 0)$:

   $$d\varepsilon_{ij} = d\varepsilon_{ij}^{e} + d\varepsilon_{ij}^{p(AF)} + d\varepsilon_{ij}^{p(IC)}$$

   $$= \frac{1+\upsilon_e}{E_e} d\sigma_{ij} - \frac{\upsilon_e}{E_e} d\sigma_{kk}\delta_{ij} + \frac{dF - \frac{\lambda-\kappa}{t_N \cdot \exp\left(\frac{1}{\beta}\left(\frac{X}{M^*}\right)^{\beta}\right)} \langle dt_N \rangle}{(1+e_0)\left(\frac{\partial F}{\partial t_{kk}} + \frac{G(\rho)}{t_N}\right)} \cdot \frac{\partial F}{\partial t_{ij}} + \frac{\frac{(\lambda-\kappa)\langle dt_N \rangle}{t_N \cdot \exp\left(\frac{1}{\beta}\left(\frac{X}{M^*}\right)^{\beta}\right)}}{(1+e_0)\left\{1+\frac{G(\rho)}{(\lambda-\kappa)a_{kk}}\right\}} \cdot \frac{\delta_{ij}}{3}$$

3. Elastoplastic region with strain softening $(dF > 0 \; and \; dt_N < 0)$:

   $$d\varepsilon_{ij} = d\varepsilon_{ij}^{e} + d\varepsilon_{ij}^{p}$$

   $$= \frac{1+\upsilon_e}{E_e} d\sigma_{ij} - \frac{\upsilon_e}{E_e} d\sigma_{kk}\delta_{ij} + \left\langle \frac{dF}{(1+e_0)\left\{\frac{\partial F}{\partial t_{mm}} + \frac{G(\rho)}{t_N}\right\}} \right\rangle \cdot \frac{\partial F}{\partial t_{ij}}$$

Then, the incremental stresses and strains can be added cumulatively to get total strains. With these total strains, the calculated stress-strain and volume change curves can be compared with the measured. This process can be repeated with different "a" and β parameters until the calculated curves best fits the measured curves.

2.3 Finite Element Method

The finite element method (FEM) is a numerical analysis that solves boundary value problems that are too complex to solve by hand. The domain within the boundaries is typically subdivided into simpler, finite, subdivisions. This analysis is usually performed with the aid of a computer.

An example of this subdivision can be seen in Figure 2-12. This process is known as creating the mesh.

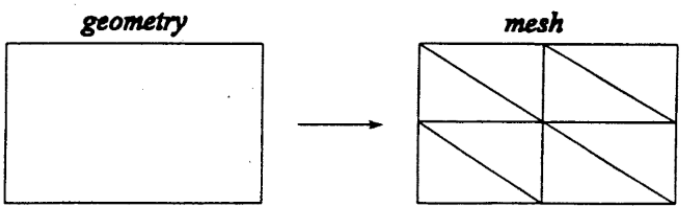

Figure 2-12: Finite element mesh.

Each element in the mesh is interconnected at common points called nodes (1D, 2D and 3D), common boundary lines (2D and 3D) or common surfaces (3D). Furthermore, each problem will have a set of governing differential equations, initial values, and boundary conditions, which are specified values on the boundaries to help solve for the unknowns.

For stress-deformation problems, constitutive models for the materials that make up the boundary value problem are needed. Examples of these constitutive models include Hooke's law for linear elastic materials, as well as Cam-Clay model and subloading tij model for non-linear elasto-plastic materials. The steps in the FEM for a stress-deformation problem include the following:

1. Discretization and select element configuration
2. Select approximation function which relate the nodal displacements to the displacements at any point in an element
3. Define strain-displacement, stress-strain relationships
4. Derive element equations
5. Assemble element equations to obtain global equation
6. Introduce boundary conditions to find primary unknowns
7. Compute secondary quantities such as stresses and strains
8. Interpret results

2.4 Unsaturated Soil Mechanics

Classical soil mechanics have traditionally been applied to analyze the behavior of two–phase materials; i.e.; saturated soils, because of its simplicity and because it is more conservative since an unsaturated soil is stronger than the same soil when saturated. Lately however, it has become increasingly important to incorporate the behavior of three–phase soils. In unsaturated soil mechanics, the air in the void give rise to suction or negative pore water pressure. An

increase in soil suction causes an increase in the strength of the soil. Conversely, a loss of suction can cause a loss of soil strength.

The symbols used in this section are as follows:

β	Angle of curvature
c’	Effective cohesion
χ	Soil saturation parameter
ϕ’	Angle of frictional resistance
R_s	Radius of curvature
S	Soil saturation
S_r	Residual soil saturation
T_s	Surface tension in contractile skin
u	Pore pressure
Δu	Change in pore pressure
u_w	Pore-water pressure
u_a	Pore-air pressure
(u_w-u_a)	Matric suction
$(\sigma-u_a)$	Net normal stress
τ	Shear strength

Unsaturated soils have three phases: soil, water, and air. However, Fredlund and Morgenstern (1977) recognized a fourth phase called air-water interface or contractile skin, which is shown in the following figure:

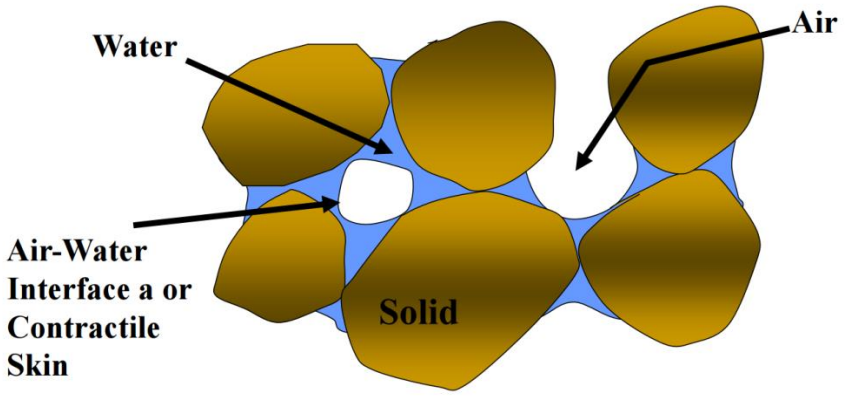

Figure 2-13: Unsaturated soil composition.

From a volume-mass point of view, this air-water interface is not important since its volume is negligible and its mass can be considered as part of the mass of water. However, during a stress analysis, it is important to consider the air-water interface because it can exert a tensile pull. This tensile pull can be prominent when a soil specimen is left to dry causing the pore water pressure to drop below zero. Since the pore air pressure remains atmospheric, the negative pore water pressure induces an unbalanced force equilibrium on the air-water interface. The air-water interface maintains equilibrium by exerting a tensile pull along the skin as shown in Figure 2-14.

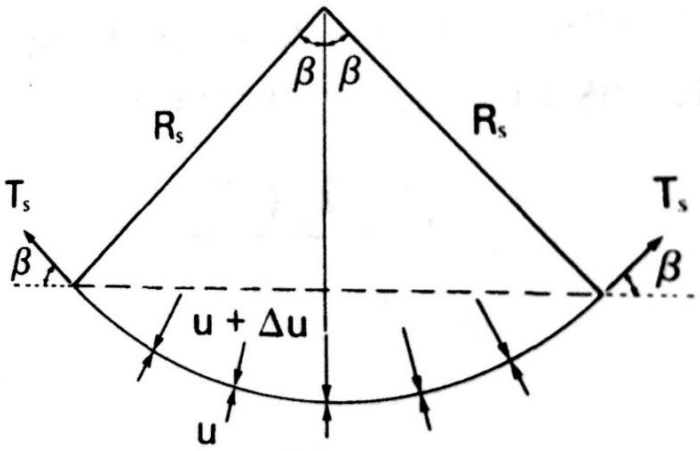

Figure 2-14: Kelvin's capillary model (Fredlund & Rahardjo, 1993).

With the aid of Figure 2-14, the difference between the pore air pressure (u_a) and pore water pressure (u_w), also known as matric suction (u_a-u_w), can be related to the radius of curvature (R_s) and the tensile pull (T_s) by resolving forces vertically as follows (Fredlund & Rahardjo, 1993):

$$2T_s sin\beta = 2\Delta u R_s sin\beta$$
$$\Rightarrow \quad \Delta u = u_a - u_w = \frac{T_s}{R_s} \qquad \text{(Equation 2.62)}$$

This can be extended to a 3-D membrane using the following figure and equation:

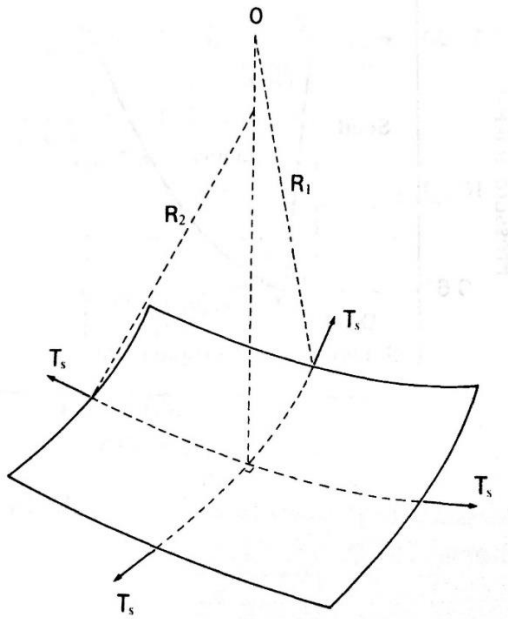

Figure 2-15: Surface tension on 3-D membrane (Fredlund & Rahardjo, 1993).

$$u_a - u_w = T_s\left(\frac{1}{R_1} + \frac{1}{R_2}\right)$$

Assuming all radii of curvature are the same: i.e.; $R_1 = R_2 = R_s$, then

$$\Rightarrow \quad u_a - u_w = \frac{2T_s}{R_s} \qquad \text{(Equation 2.63)}$$

Therefore, if the matric suction goes to zero, the radius of curvature goes to infinity and the air-water interface becomes flat.

A normal or shear load applied to an unsaturated soil will change the radius of curvature of the air-water interface leading to a change in matric suction. This is demonstrated in Figure 2-16.

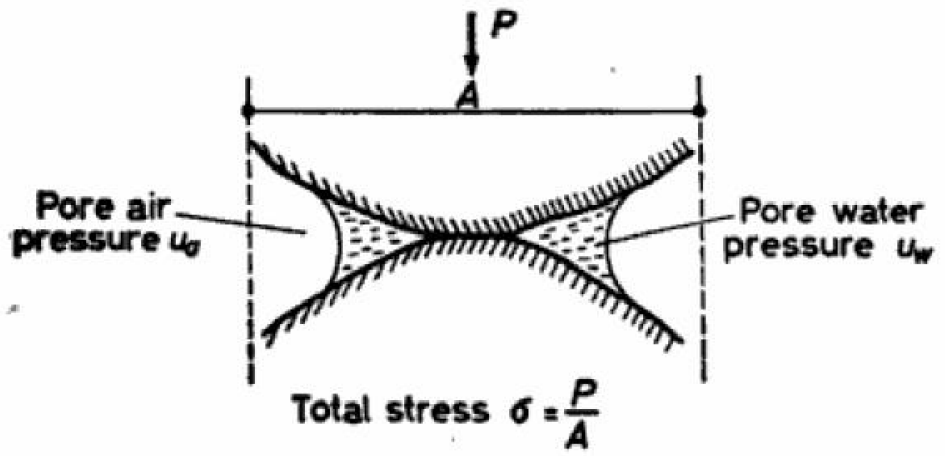

Figure 2-16: Influence of load application on matric suction (Fredlund & Rahardjo, 1993).

Bishop recognized that matric suction does affect the soil effective stress and proposed incorporating the matric suction in the effective stress equation as follows:

$$\sigma' = (\sigma - u_a) + \chi(u_a - u_w) \qquad \text{(Equation 2.64)}$$

where χ = Bishop's effective stress parameter that is related to the degree of saturation $= \frac{S - S_r}{1 - S_r}$ (Vaanapalli and Fredlund, 2000). When the soil is saturated, χ = 1, and the effective stress equation reverts to Terzaghi's equation: $\sigma' = \sigma - u_w$.

Similarly, including the effects of matric suction into the shear strength equation will result in an equation as follows:

$$\tau = c' + (\sigma_n - u_a)tan\phi' + \chi(u_a - u_w)tan\phi' \qquad \text{(Equation 2.65)}$$

From Equation 2.65, it can be seen that the matric suction effectively increases the soil confining stress by $\chi(u_a - u_w)$, which is important to consider when doing a stress analysis of an unsaturated soil.

To estimate the soil matric suction of a soil at a given water content, it is necessary to know the soil-water characteristic curve (SWCC), which is a plot of the water content vs matric suction. The following figure is an example of a SWCC:

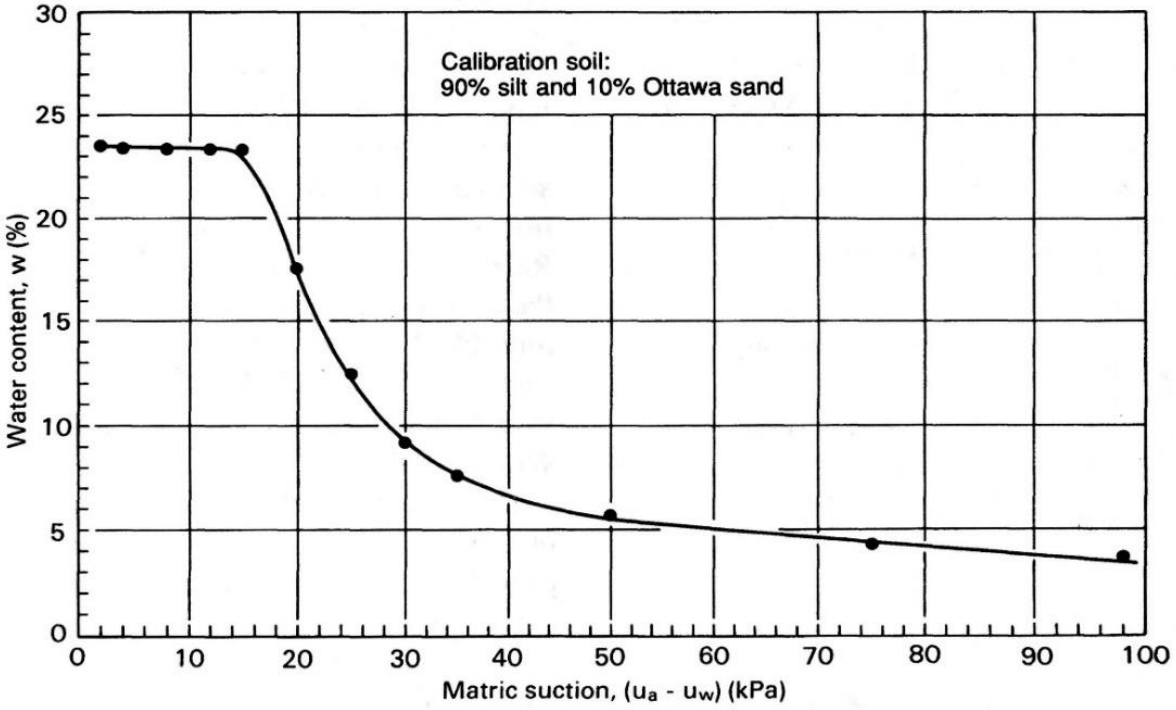

Figure 2-17: Example of SWCC (Fredlund and Wong, 1989).

3 PERFORMANCE TEST

Between 2011 and 2012, 14 GRS columns (mini-piers) were constructed and load tested by the Federal Highway Administration at the Turner-Fairbank Highway Research Center (TFHRC). Iwamoto (2014) analyzed eight of these in detail. Pertinent characteristics of these tests are summarized in Table 3-1.

Table 3-1: GRS performance tests conducted at TFHRC (Iwamoto, 2014).

Test	T_f[1] (lb/ft)	S_v[2] (in)	T_f/S_v (ksf)	Height of Mini-Pier (ft)	H/B	Facing Type
TF-6	4800 x 4800	7.63	7.55	6.35	1.95	CMU
TF-7	4800 x 4800	7.63	7.55	6.35	1.95	None
TF-9	4800 x 4800	15.3	3.78	6.35	1.95	CMU
TF-10	4800 x 4800	15.3	3.78	6.35	1.95	None
TF-11	1400 x 1400	3.81	4.41	6.35	1.95	None
TF-12	1400 x 1400	3.81	4.41	6.35	1.95	CMU
TF-13	3600 x 3600	11.3	3.84	6.56	2.02	None
TF-14	3600 x 3600	11.3	3.84	6.56	2.02	CMU

Notes: T_f = wide width tensile strength (all geotextiles have identical wide width tensile strengths in the machine and cross machine directions)
S_v = reinforcement spacing

This thesis will focus primarily on performance tests TF-6 and TF-7 since the geotextile strength and spacing are more in line with those commonly used in GRS practice. Details for the other performance tests have been described in detail by Nicks et al. (2013). The following is a list of symbols used in this chapter:

B	Width of the soil section of the GRS column
c	Cohesion
ε_f	Strain at failure
γ_d	Dry unit weight
H	Height of the soil section of the GRS column
ϕ	Friction angle
$q_{ult:\ emp,\ CMU,\ No\ CMU}$	Ultimate bearing capacity of: mini pier, with CMU, without CMU
S_v	Reinforcement spacing
$\sigma_{h,\ v}$	Horizontal, vertical stress
T_f	Wide width tensile strength

ω_{opt} Optimum water content

3.1 Test Configuration

Performance tests TF-6 and TF-7 are identical in every way except the cast masonry units (CMU) used as a facing were removed in TF-7 but not in TF-6 (see Figure3-1).

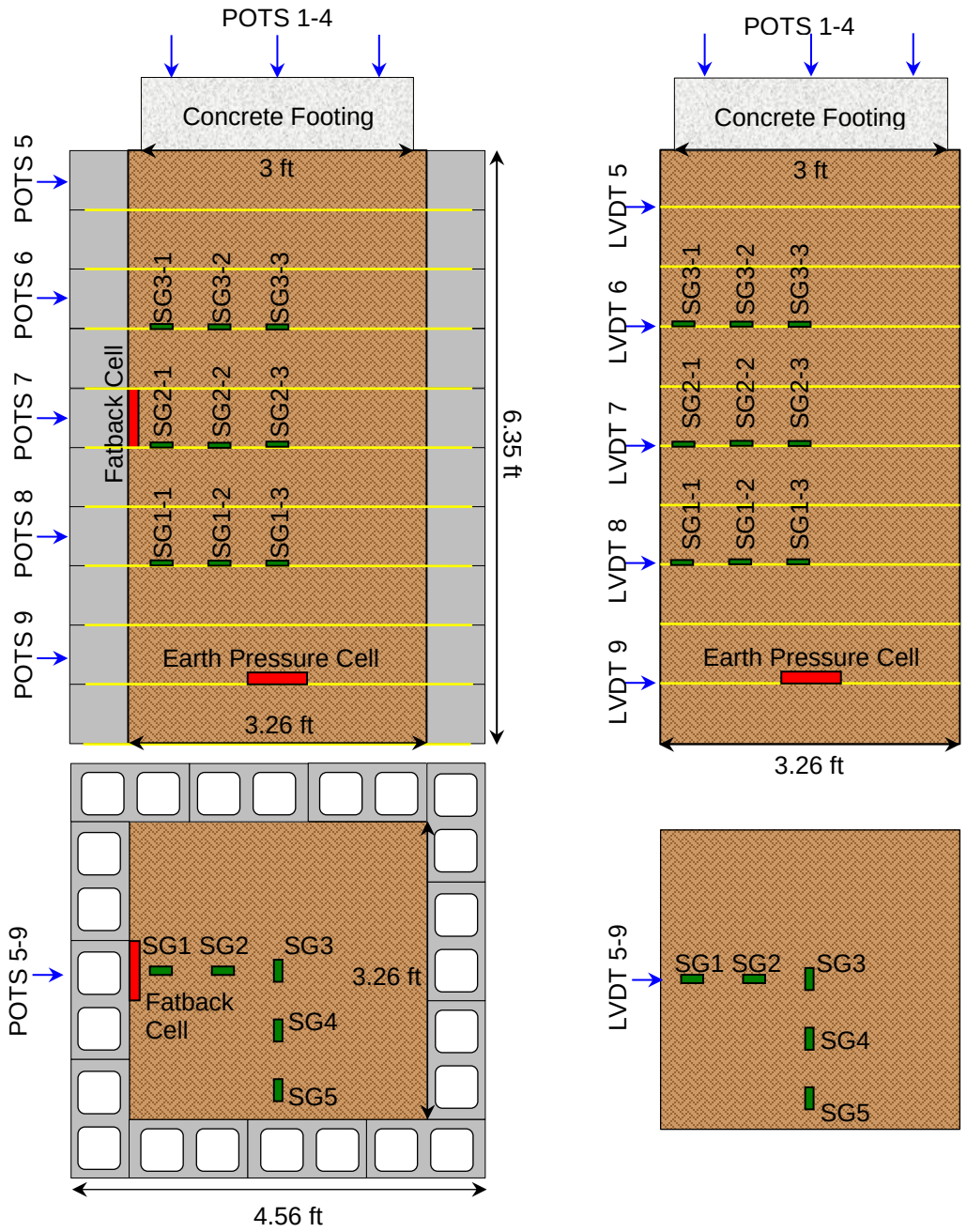

Figure 3-1: Plan and profile of TF-6 (left) and TF-7 (right) (Iwamoto, 2014).

Also both TF-6 and TF-7 were instrumented with potentiometers and linear variable differential transducers (LVDT) to measure deflections, fatback cells to measure lateral earth pressures, earth pressure cells to measure vertical stresses, and strain gages (SG) to measure strains in the geotextiles.

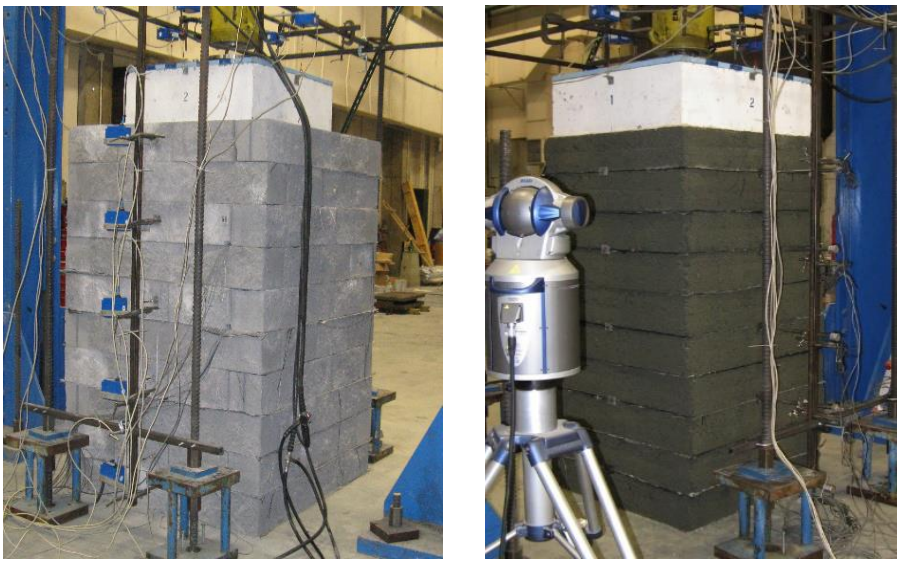

Figure 3-2: Photo of TF-6 (left) and TF-7 (right) (Iwamoto, 2014).

Figure 3-2 contains photos of the performance tests TF-6 and TF-7.

3.2 Backfill

The backfill used for the GRS columns was a well-graded gravel with silty fines (GW-GM) from Lucky Stone quarry in Leesburg, VA (Iwamoto, 2014). This backfill met the requirements for a 21A base course according to Virginia Department of Transportation (VDOT) and a GRS-IBS abutment backfill according to the Federal Highway Administration (FHWA), respectively. The backfill's grain size distribution is shown in Figure 3-3.

Direct shear tests were performed at normal stresses of 5 psi to 30 psi on the backfill with a maximum dry unit weight (γ_d) of 147 pcf and an optimum water content (ω_{opt}) of 7.5% (see Figure 3-4 for compaction curve). The direct shear soil specimens were 12-inch x 12-inch x 8-inch and were sheared at a rate of 0.015 in/min. The resulting Mohr-Coulomb failure envelope is plotted in Figure 3-5.

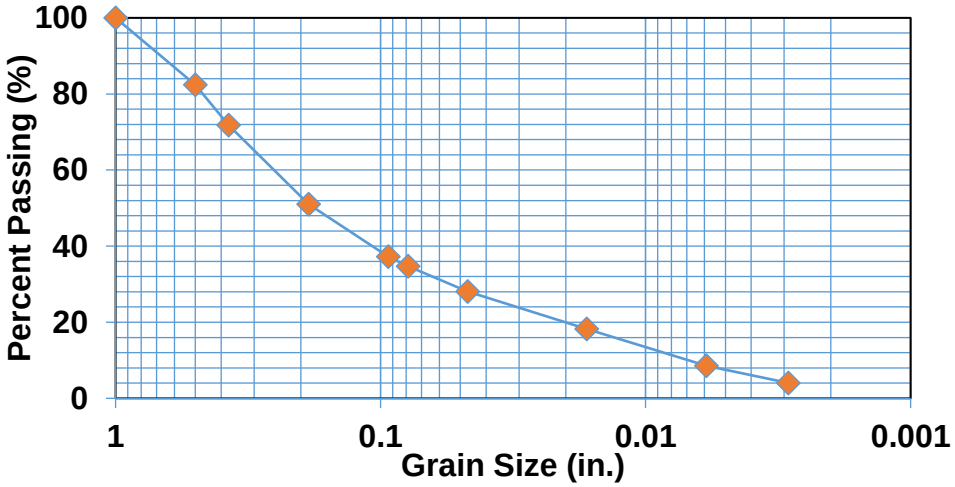

Figure 3-3: VDOT 21A Grain Size distribution (Iwamoto, 2014).

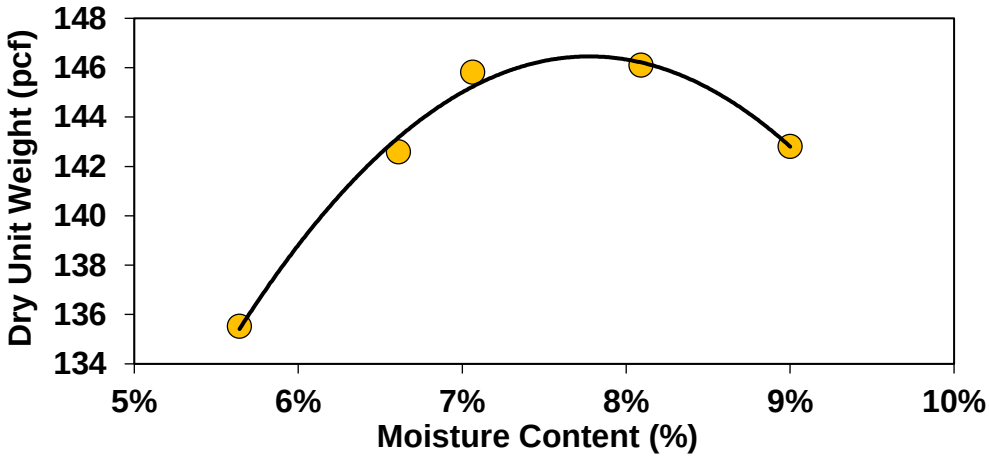

Figure 3-4: VDOT 21A Compaction Curve (Iwamoto, 2014).

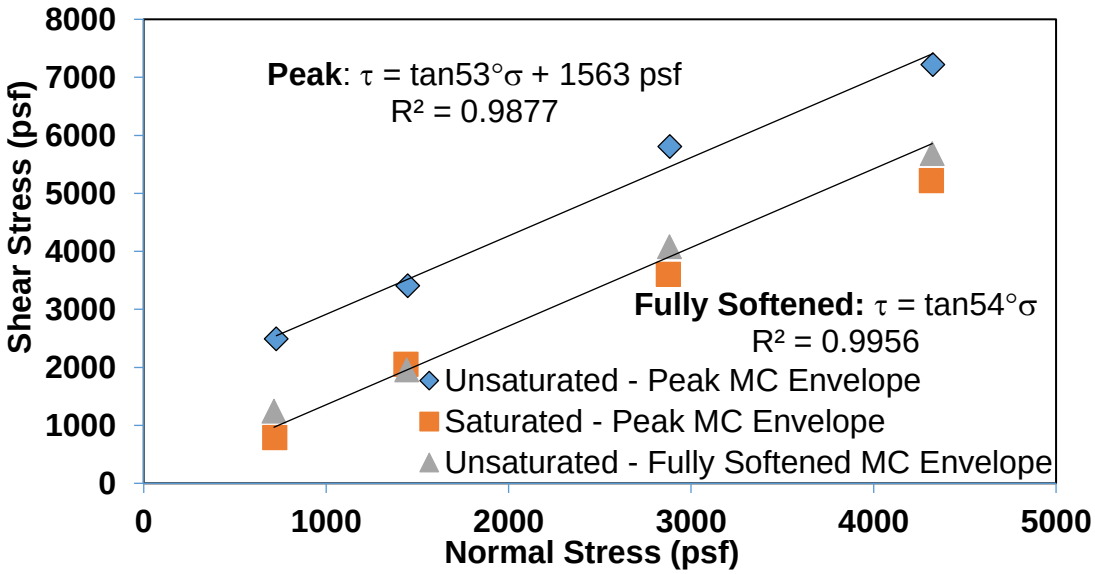

Figure 3-5: Mohr-Coulomb failure envelope of GRS backfill based on large scale direct shear tests (Iwamoto, 2014).

From Figure 3-5, the friction angle (ϕ) is 53° and cohesion (c) is 1563 psf at the peak for the unsaturated soil specimen, while the saturated sample has a similar friction angle with a negligible cohesion. Iwamoto et al. (2013) showed that fully softened strengths of the backfill yielded capacities that agreed better with measured GRS capacities (Iwamoto, 2014). The reason for this is because of the fact that the reinforcement in the GRS strengthens the soil by making it more ductile and results in very large strains (>10%) at failure while the peak soil strengths are mobilized at relatively smaller strains (≈2-5%) in the large scale direct shear tests (Iwamoto, 2014).

Lastly, the backfill was compacted with a Vibco Patchman PM 1012 plate compactor in 3.8-inch-thick lifts with the top two rows of CMU blocks ratchet-strapped together. With the aid of nuclear density gage, the relative compaction of each lift was maintained close to 100% and the water content at ±2% of optimum.

3.3 Geosynthetic Reinforcement

All geotextiles used in the GRS columns were biaxial, woven polypropylene as summarized in Table 3-2.

Table 3-2: Properties of geotextiles used (Iwamoto, 2014).

Test	Geotextile Manufacturer	Wide Width Tensile Strength (lb/ft)	Wide Width Tensile Strength at 5% Strain (lb/ft)	Tensile Strength (Grab) (lb)	Wide Width Elongation (%)
TF-6, -7, TF-9, -10	Propex	4800 x 4800	660 x 1500	600 x 500	(10 x 8%)
TF-11, -12	Industrial Fabrics	1400 x 1400	Not specified	200 x 200	(9 x 7%)
TF-13, -14	US Fabrics	3600 x 3600	1392 x 1740	450 x 350	(15 x 10%)

Due to the geotextiles having different stiffnesses in the cross-machine and machine directions, the reinforcements were placed in an alternating pattern to prevent the GRS from having a weaker reinforcement in a certain direction.

3.4 CMU Blocks

The CMU blocks used as a facing for the GRS columns were dry-cast, split-faced, weighed around 42 lbs on average, and had dimensions as shown in Figure 3-6.

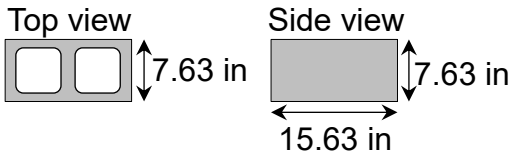

Figure 3-6: CMU block dimensions (Iwamoto, 2014).

For TF-6, the CMU blocks were frictionally connected to the geotextile. TF-7 did not have CMUs prior to load testing and thus, the geotextiles were trimmed to be flush with the backfill.

3.5 GRS Column Load Test Configuration

As seen in Figure 3-7, the loading configuration for the load test consisted of two 12-inch stroke Enerpac jacks, a two-post reaction frame that was bolted to the floor, and a data acquisition system.

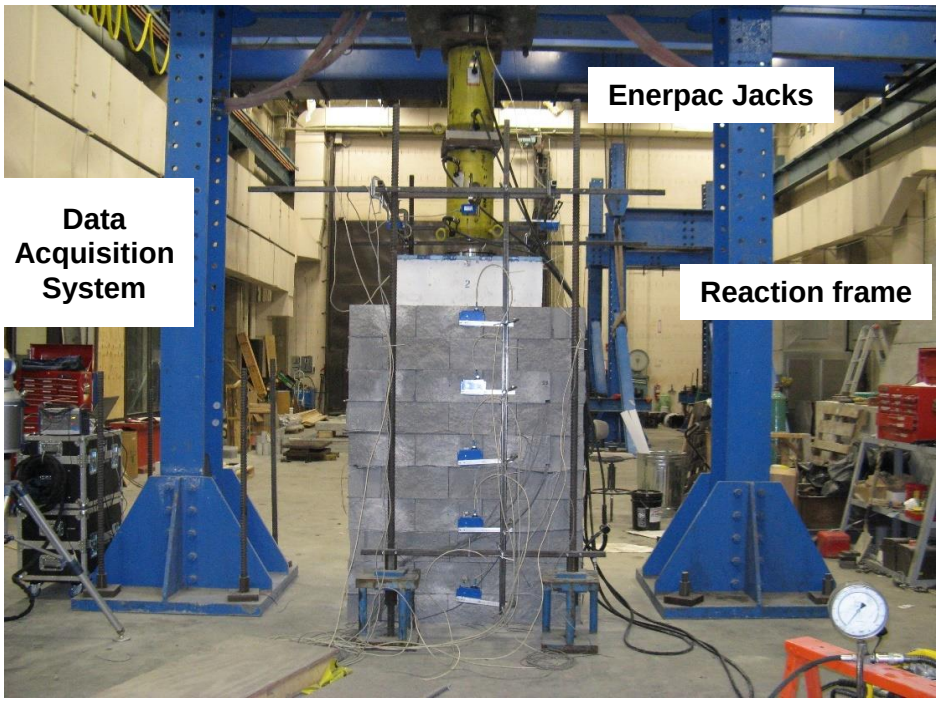

Figure 3-7: Loading system (Iwamoto, 2014).

The data acquisition system recorded settlements at 1, 3, 5, 7, 15, 20, 25, and 30 minute intervals from the start of each load increment. The load was manually applied with a hydraulic pump.

Furthermore, the load was maintained with a strain indicator box and was increased when no significant settlement occurred (< 0.003 inches). Each load increment was held for a minimum of 5 minutes and a maximum of 30 minutes. Each load test took about 6 hours to complete.

3.6 Instrumentation

The instrumentation used in the performance tests consisted of potentiometers, LVDTs, fatback cells, earth pressure cell and strain gages (see Figure 3-1).

The purpose of the potentiometers and LVDTs on the vertical faces of the GRS column was to measure lateral deflection. The potentiometers at the top of the GRS columns measured vertical deflection. Furthermore, the potentiometers and LVDTs were attached to a reference beam or column and measurements were recorded every minute.

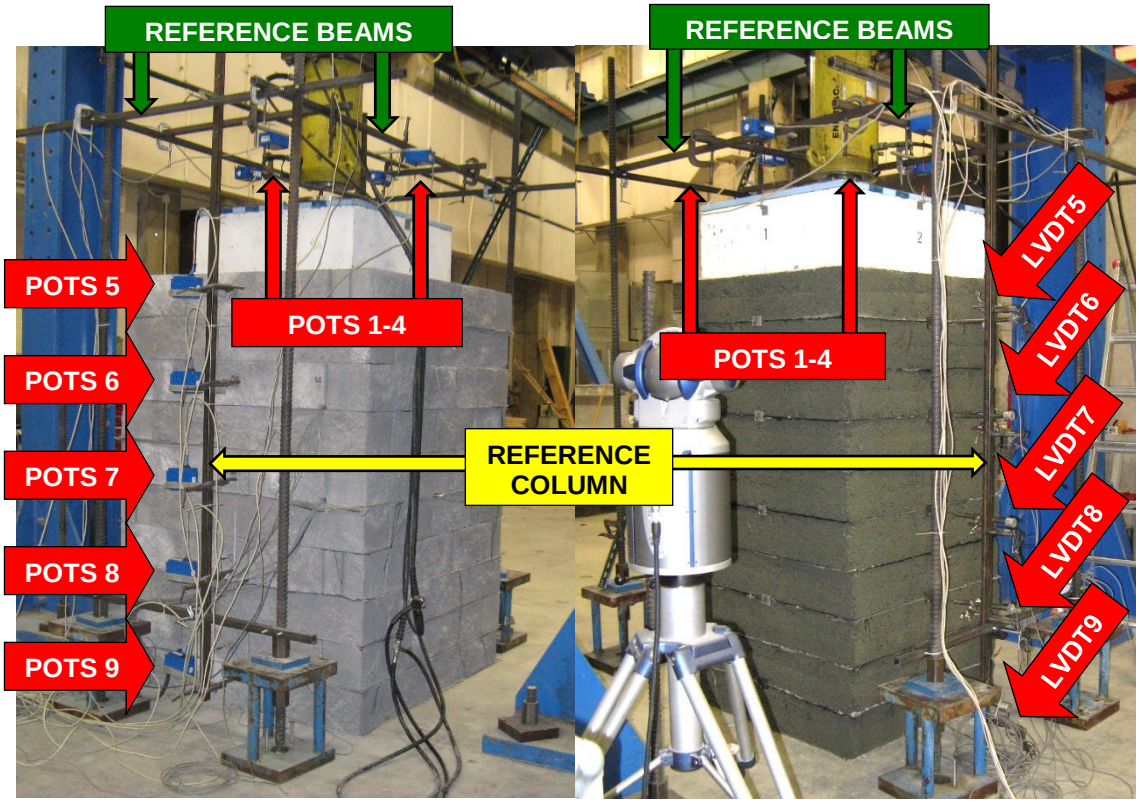

Figure 3-8: Deflection instrumentation configuration on TF-6 (left) and TF-7 (right) (Iwamoto, 2014).

Attached to the CMU block, the fatback cell (Figure 3-9) was used to measure the lateral pressure near the mid-height of GRS column TF-6. Six inches in diameter, the fatback cell

consisted of Geokon's model 4810, which is designed specifically to measure soil pressures against a structural face. Due to the GRS columns being loaded to failure, the fatback cells were not re-used after each performance test.

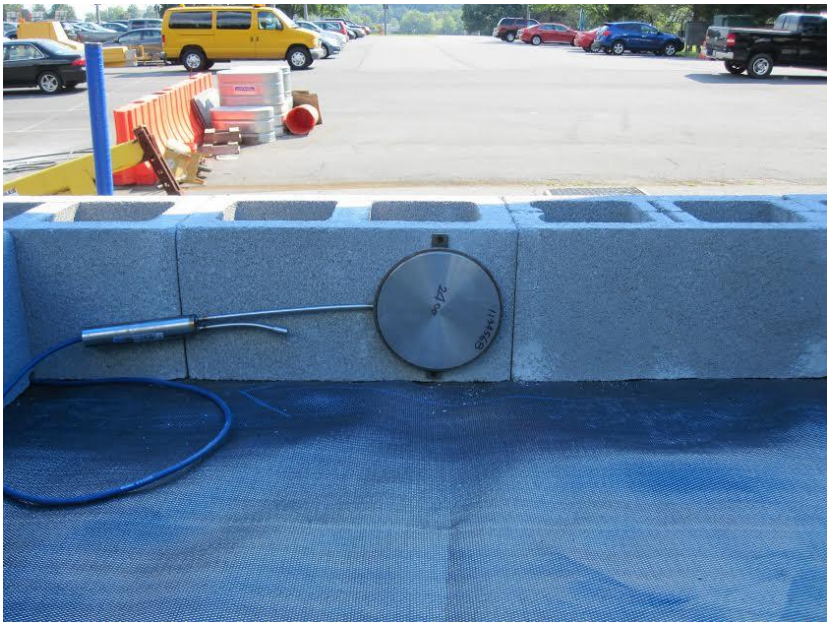

Figure 3-9: Fatback Cell (Iwamoto, 2014).

Earth pressure cells were used to measure the vertical earth pressures near the bottom of both TF-6 and TF-7. Nine inches in diameter, the earth pressure cells consisted of Geokon's model 4815. Centered in plan, they were placed 7.625 inches from the bottom of the GRS column.

Strain gages were used to measure strains in two orthogonal directions on the third, fifth and seventh geotextile layers. All strain gages were manufactured by Vishay Measurements Group, Inc. and their model type was the EP-08-250BG-120. These strain gages were glued to a 1-inch x 3-inch rectangular patch, which was then attached to the geotextile. This attachment technique was developed by the University of Colorado at Denver to prevent the geotextile from stiffening if the whole length of the strain gage was attached. This technique can be seen in Figure 3-10:

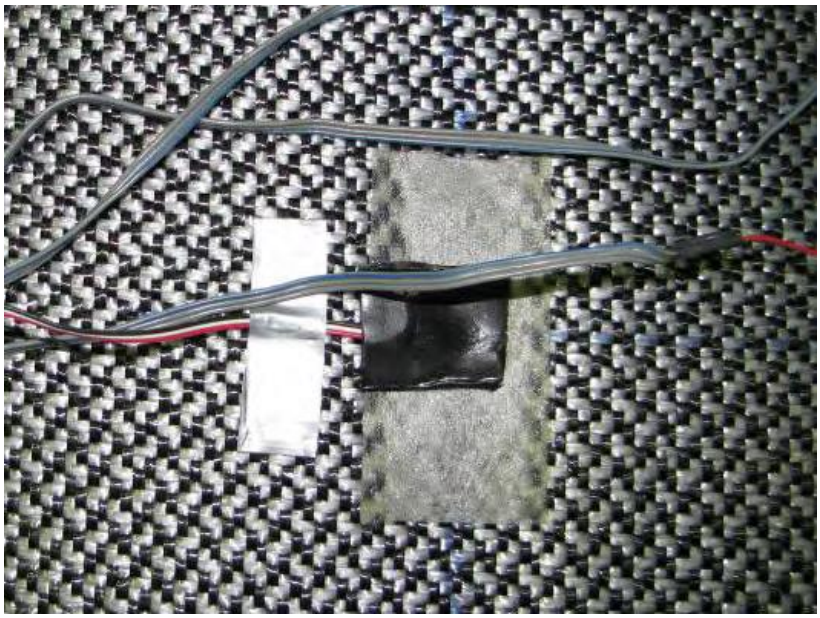

Figure 3-10: Strain gage attached using University of Colorado at Denver's technique (Iwamoto, 2014).

The 5 strain gages were set up in a 90 degree, L-shape pattern as shown in Figure 3-1 to provide strains in two orthogonal directions.

3.7 Results

This section will focus on the ultimate bearing capacities, load-settlement curves, lateral pressures and lateral displacement profiles of TF-6 and TF-7. Details of the other performance tests results can be found in "Geosynthetic Reinforced Soil Performance Testing – Axial Load Deformation Relationships" (Nicks et al., 2013) and "Observations from Load Tests on Geosynthetic Reinforced Soil" (Iwamoto, 2014).

3.7.1 Ultimate Bearing Capacity

The ultimate bearing capacity, $q_{ult,\ emp}$, and the strain at failure, ε_f, for all the GRS column performance tests are summarized in Table 3-3.

Table 3-3: Ultimate bearing capacity and strain at failure of mini-pier load tests (Iwamoto, 2014).

Test	T_f[1] (lb/ft)	S_v[2] (in)	T_f/S_v (ksf)	Height (ft)	Facing Type	$q_{ult,emp}$[3] (ksf)	$q_{ult,CMU}$[4]/ $q_{ult,No\ CMU}$[5]	ε_f[6] %
TF-6	4800	7.63	7.55	6.35	CMU	43.8	1.65	15.7
TF-7	4800	7.63	7.55	6.35	None	26.5		12.5
TF-9	4800	15.3	3.78	6.35	CMU	22.3	2.17	15.6
TF-10	4800	15.3	3.78	6.35	None	10.3		14.3
TF-11	1400	3.81	4.41	6.35	None	23.2	1.25	12.8
TF-12	1400	3.81	4.41	6.35	CMU	29.0		13.4
TF-13	3600	11.3	3.84	6.56	None	13.0	1.82	12.3
TF-14	3600	11.3	3.84	6.56	CMU	23.6		12.7

Notes:
1. T_f = wide width tensile strength (all geotextiles have identical wide width tensile strengths in the machine and cross machine directions)
2. S_v = reinforcement spacing
3. $q_{ult,emp}$ = ultimate bearing capacity of mini-pier
4. $q_{ult,\ CMU}$ = ultimate bearing capacity of mini-pier with CMU
5. $q_{ult,\ No\ CMU}$ = ultimate bearing capacity of mini-pier without CMU
6. ε_f = strain of load test at failure

The following observations can be made from Table 3-3:

- The GRS columns that had CMU blocks had higher capacities than those without. This is due to the confinement that the CMU blocks provided. For example, TF-6's ultimate bearing capacity of 43.8 ksf is 65% greater than TF-7, which had a value of 26.5 ksf (Iwamoto, 2014).
- As the T_f/S_v ratio increased, so did the ultimate bearing capacity.
- TF-6 had an ultimate bearing capacity (43.8 ksf) 11 times greater than the allowable bearing pressure (4 ksf; Elias and Christopher, 1997) of a GRS-IBS bridge abutment.

Therefore, it can be said that a GRS column can achieve a greater capacity with smaller reinforcement spacing, higher reinforcement strength, and the utilization of CMU blocks as facing.

3.7.2 *Load-settlement Curves*

The load-settlement curves for the performance tests are summarized in Figure 3-11.

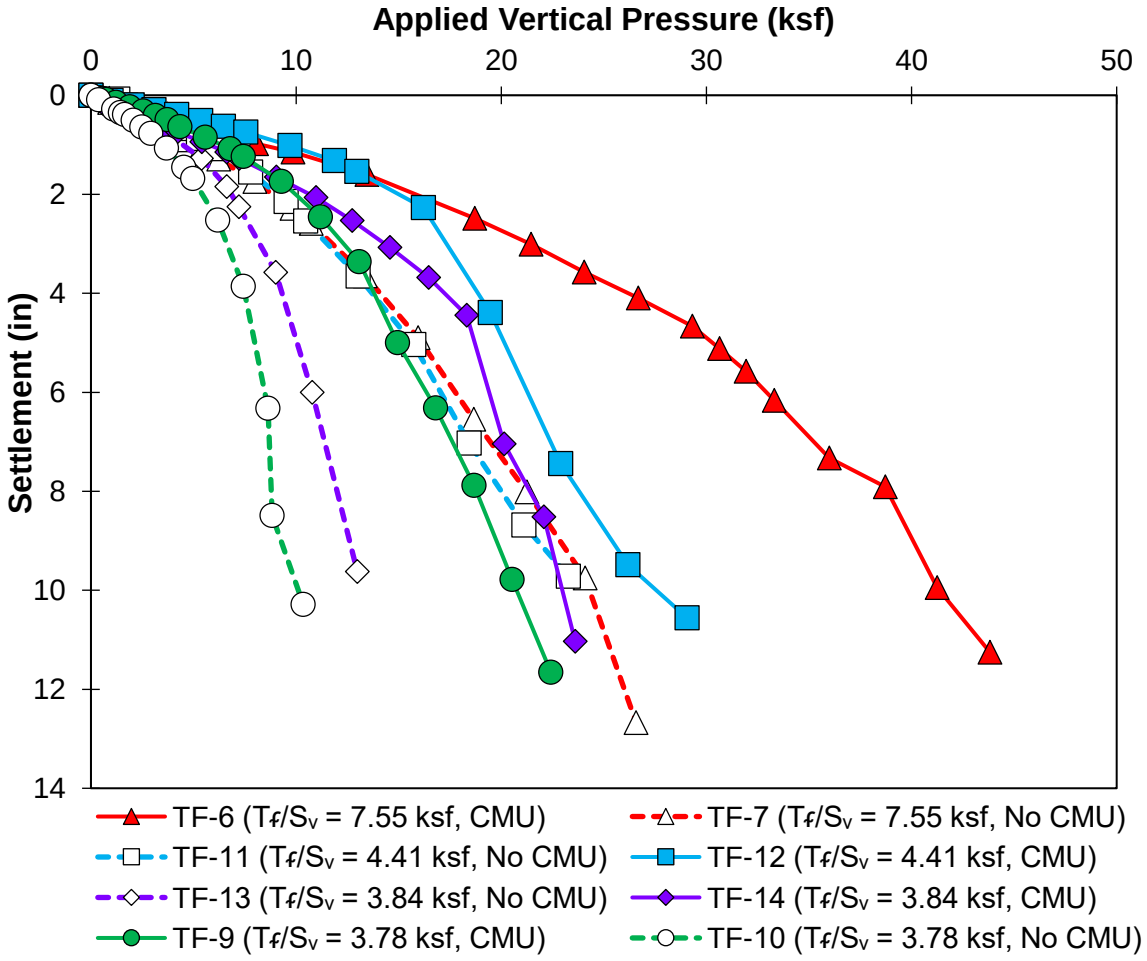

Figure 3-11: Load-settlement curves (Iwamoto, 2014).

From Figure 3-11, the GRS column with the highest capacity was TF-6 while the lowest was TF-10.

3.7.3 *Failure Plane*

The failure plane in the GRS column with CMU blocks is not visible until the CMU blocks were removed. Figure 3-12 depicts how each individual reinforcement in TF-6 ripped after it was loaded to failure (a-i) and how those rips formed a failure plan (j). Geotextiles 2 through 6 had tears around the inside edges of the CMU as well as tears through the soil mass

from one CMU face to the opposite face. This shear failure plane is similar to what is observed in triaxial specimens.

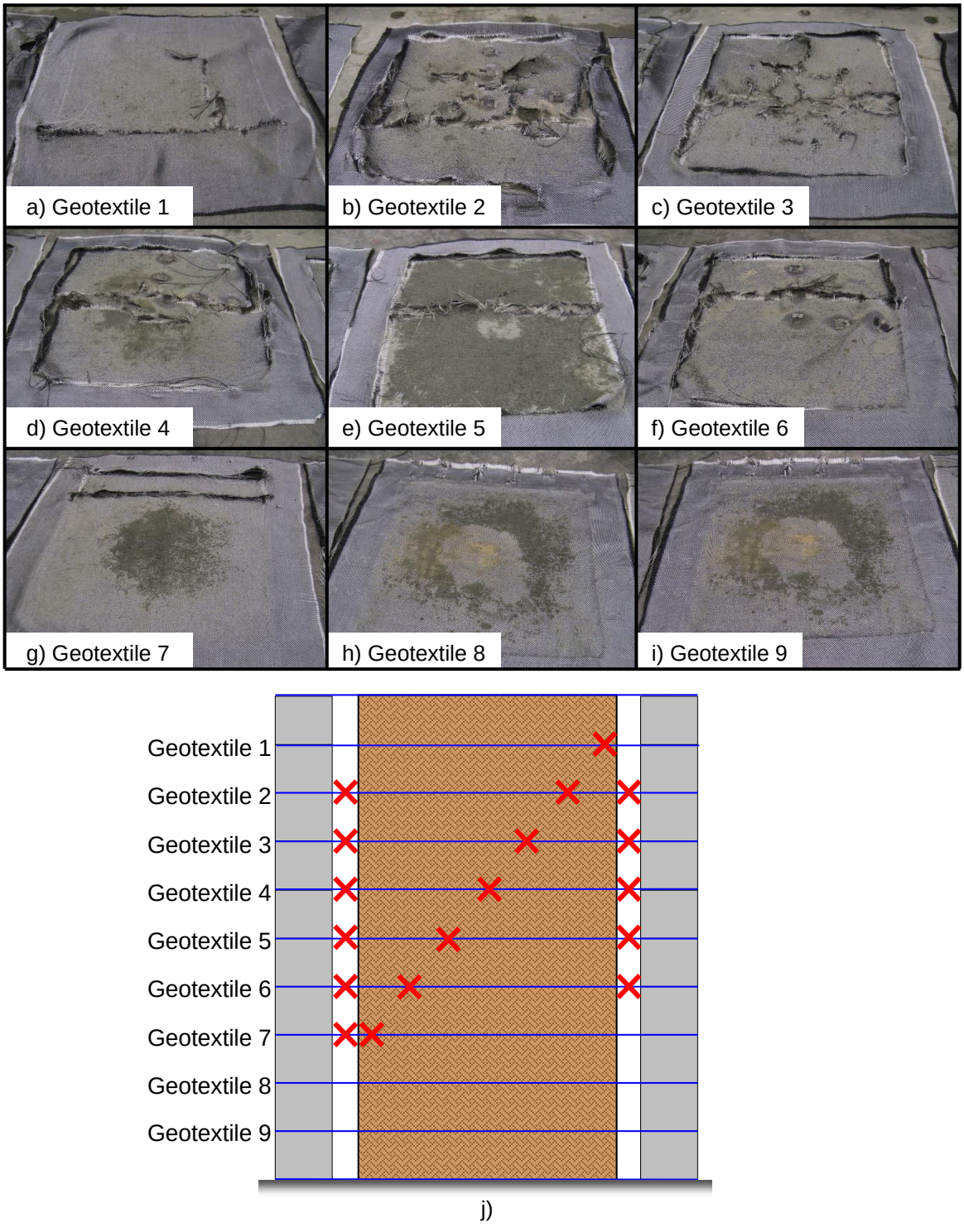

Figure 3-12: (a – i) TF-6's geotextiles after loading until failure; (j) failure plane due to the tears in geotextiles in TF-6 (Iwamoto, 2014).

It is also worth noting that some of the CMU blocks did crush during the TF-6 performance test.

A distinct failure plane was observed in TF-7 but no photographs are available.

3.7.4 Lateral Pressure

Figure 3-13 shows the measured lateral pressures and the corresponding vertical pressure during the load tests.

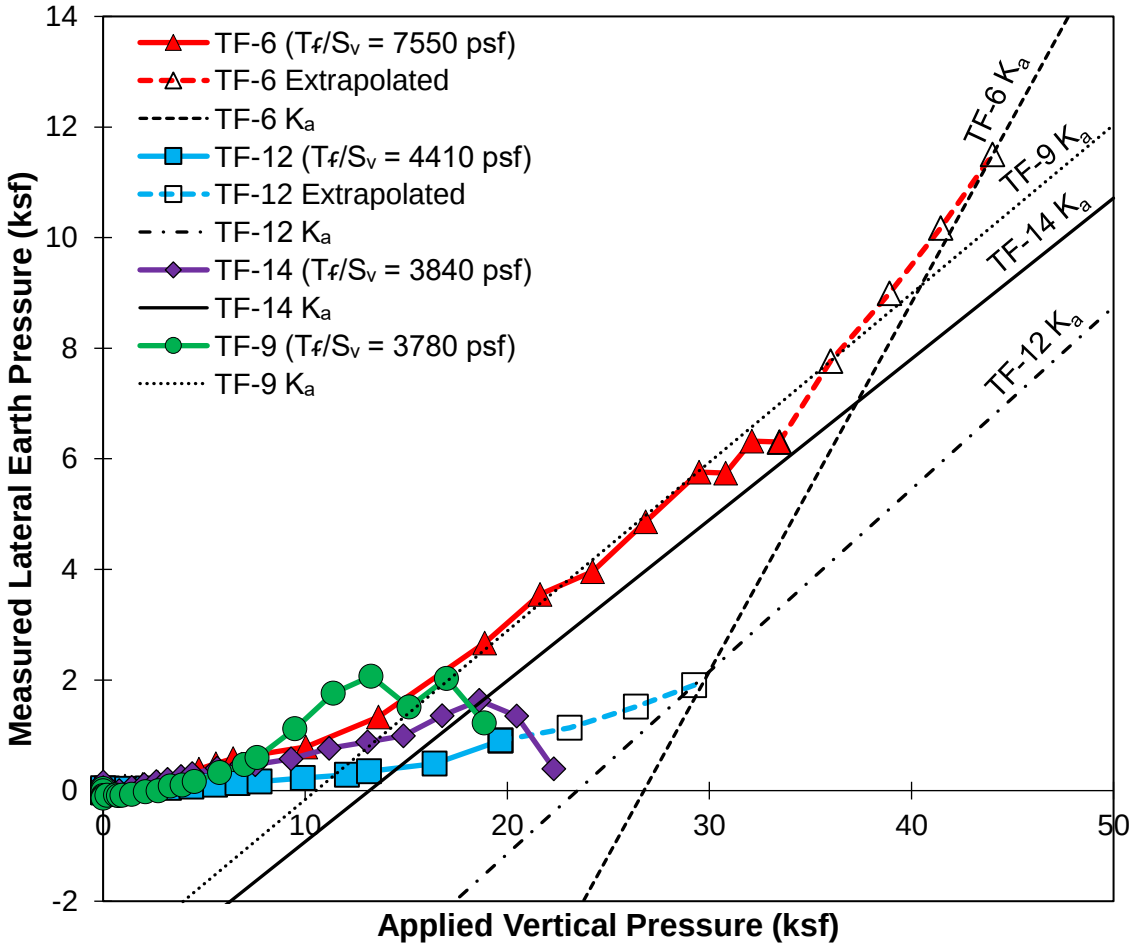

Figure 3-13: Measured lateral pressures at Fatback cell location during load testing of TF-6, -9, -12, and -14 (Iwamoto, 2014).

During the test, the fatback cell in TF-6 failed prematurely. However, based on TF-12 and TF-14 in Figure 3-13, it can be seen that the lateral pressures increased gradually with increasing load to a maximum followed by an abrupt drop. Iwamoto (2014) theorized that the CMU provide a confining stress to the GRS. As the vertical load increased and the GRS settled, the geotextiles turn downward on the inside edges of the CMU, thus making the fabric exert an axial

load on the CMU. This then restrains the blocks from moving laterally and a build-up in lateral pressure occurs, which gives the GRS structure strength. However, when the geotextile reaches its tensile strength, the geotextiles rip, and the CMU blocks lurch forward causing the lateral pressure to reduce. Once the CMU blocks are no longer connected to the GRS via the geotextile, the behavior of the GRS approaches the results of the GRS without CMUs.

3.7.5 Lateral Displacement

Using the measurements from the potentiometers and LVDTs, the lateral deformations along the GRS column height at various loads are plotted in Figure 3-14 for TF-6 and Figure 3-15 for TF-7.

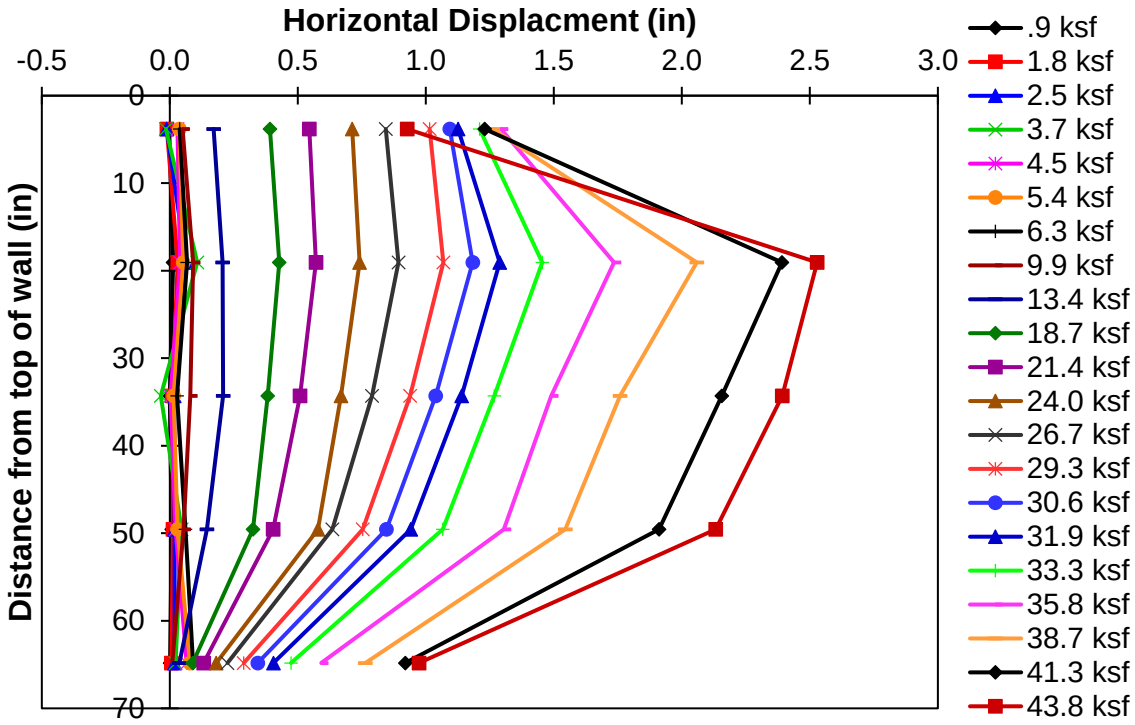

Figure 3-14: Lateral displacement of TF-6 (Iwamoto, 2014).

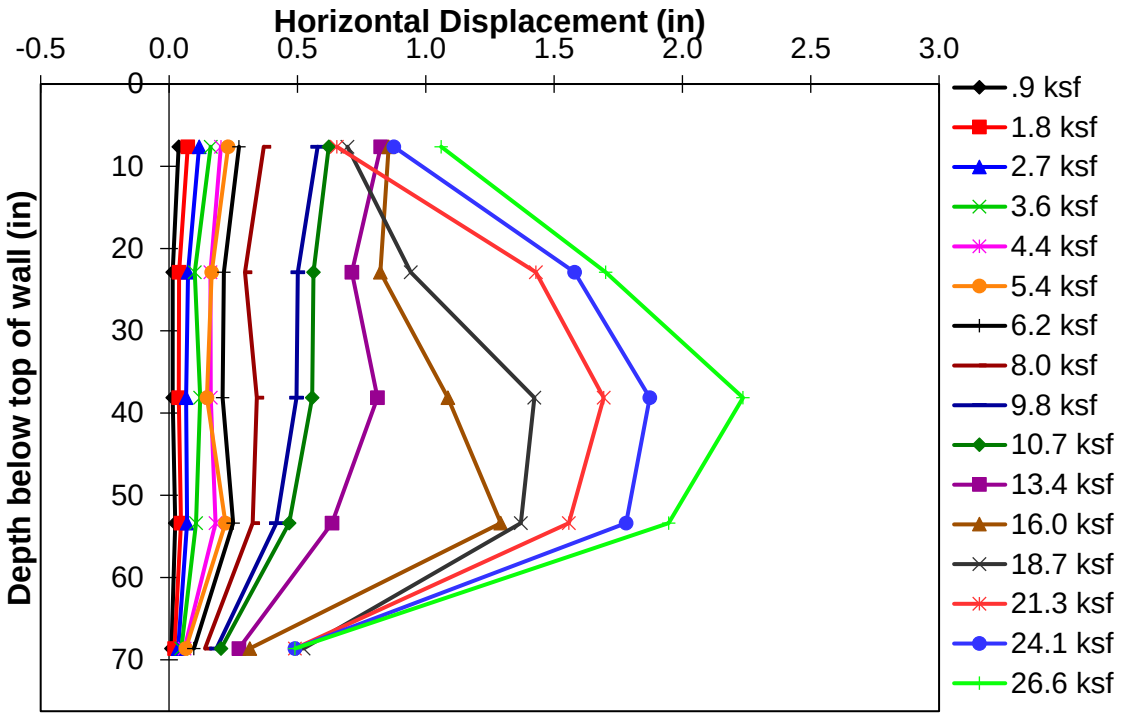

Figure 3-15: Lateral displacement of TF-7 (Iwamoto, 2014).

TF-6 has slightly larger lateral displacements at failure than TF-7. At failure, the mid-height portions of both TF-6 and TF-7 have the largest lateral movement as the GRS bulges out. At smaller loads, the largest deflections occurred at or near the top of the GRS.

4 MODEL PARAMETERS

This chapter will describe how the parameters used for modelling the soil, CMU, geotextile, footing, and interface friction angles are derived. A list of symbols used in this chapter is as follows:

Subloading t_{ij} Model Parameters for the Soil

a	Influence of density parameter
β	Parameter (≥ 1) that controls the shape of the yield function (if β = 1 => original Cam-Clay model
e	Void ratio
e_0	Initial void ratio
ε_v	Volumetric strain
κ	Slope of unload-reload line
λ	Slope of isotropic normally consolidation line
M	Slope between origin and top of yield locus in q-p' space
N	Reference specific volume (or void ratio) at 1 atmosphere
p'_{cs}	Mean stress at critical state
v_{cs}	Specific volume at critical state
R_{cs}	Stress ratio at critical state

Soil-water Characteristic Curve Parameters

χ	Effective stress parameter
$(\sigma_n - u_a)$	Net normal stress
$(u_a - u_w)$	Matric suction
S	Degree of saturation
S_r	Residual saturation
τ	Shear strength

Drucker Prager Model Parameters for the CMU

c'	Effective cohesion
E	Young's modulus

G	Shear modulus
γ	Unit weight
ν	Poisson's ratio
ϕ'	Angle of frictional resistance
ψ	Angle of dilatancy

Softening Model Parameters for the Geotextile

EA	Axial stiffness
ε_d^p	Plastic deviatoric strain
h^p	Plastic modulus
Λ	Proportionality constant
T_y	Tensile strength
χ	Exponential decay parameter

Footing Parameters

E	Young's modulus
G	Shear modulus
γ	Unit weight
ν	Poisson's ratio

Interface Element Parameters

δ	Interface friction angle

4.1 **Soil**

An isotropic consolidation test and 4 drained triaxial tests were conducted by FHWA from which the subloading t_{ij} model parameters for the soil were derived. Furthermore, using a computer program called SoilVision, a soil-water characteristic curve (SWCC) was derived to estimate a confining stress that has to be applied to the backfill to account for the effects of suction being present in the unsaturated GRS backfill. Estimation of these parameters is described below.

4.1.1 Isotropic Consolidation Test

As discussed in Section 2.2, λ and κ can be obtained from the normal consolidation line and unload-reload curve, respectively, of an isotropic consolidation test. In an isotropic consolidation test on the GRS backfill, the soil was first consolidated to a mean stress of about 34.5 kPa. The isotropic stress was then increased to 345 kPa. After that, the soil was unloaded to 34.5 kPa and then reloaded back to 345 kPa. This was repeated for a total of three unload stages.

The measured volumetric strain was converted into void ratio using the following relationship:

$$\Delta\varepsilon_v = -\frac{\Delta e}{1+e_0} \qquad \text{(Equation 4.1)}$$

The void ratio was then plotted against the mean stress as shown in Figure 4-1. It is important to correct the isotropic consolidation curves for membrane compliance (penetration of membrane into the soil). Any inward movement of the membrane causes a change in void volume that is not related to volume contraction of the soil. The membrane compliance correction is reflected in the isotropic consolidation test results plotted in Figure 4-1.

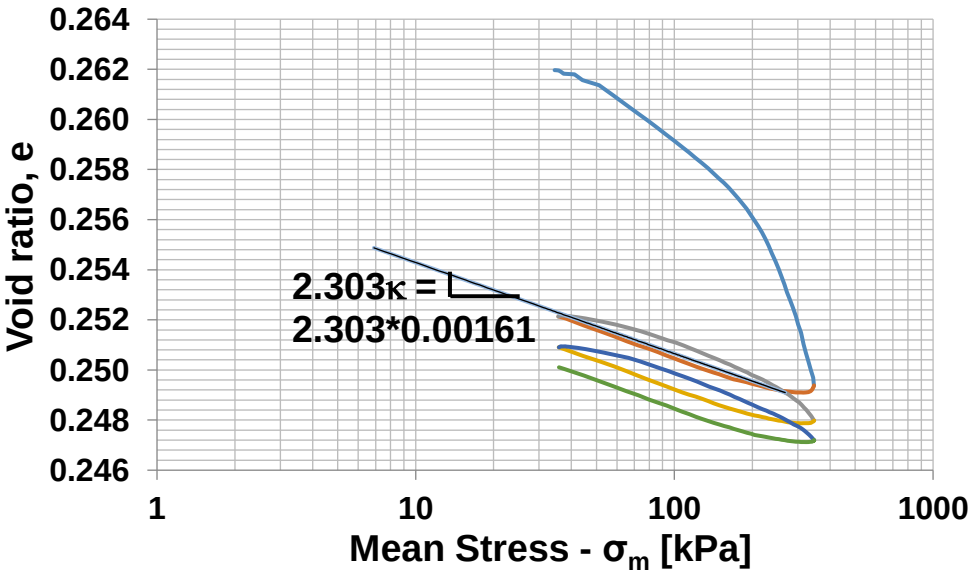

Figure 4-1: Using isotropic consolidation test to estimate normally and unload-reload slopes.

From Figure 4-1, κ = 0.00161. There was a great deal of uncertainty on the value of λ since the normally consolidated line in Figure 4-1 is rather short. Because the normally consolidated line

has the same slope as the critical state line in theory, it was decided to estimate λ by using the slope of the critical state line on the e-ln ($\sigma_{m)}$ plot instead.

4.1.2 Drained Triaxial Test

Drained triaxial tests were conducted by FHWA on the GRS backfill at confining stresses of 5, 10, 20, and 30 psi (34.5, 69, 138 and 207 kPa). Deviator stress vs axial strain, volumetric strain vs axial strain, and q/p vs axial strain plots are provided in figures 4-2, 4-3 and 4-4, respectively.

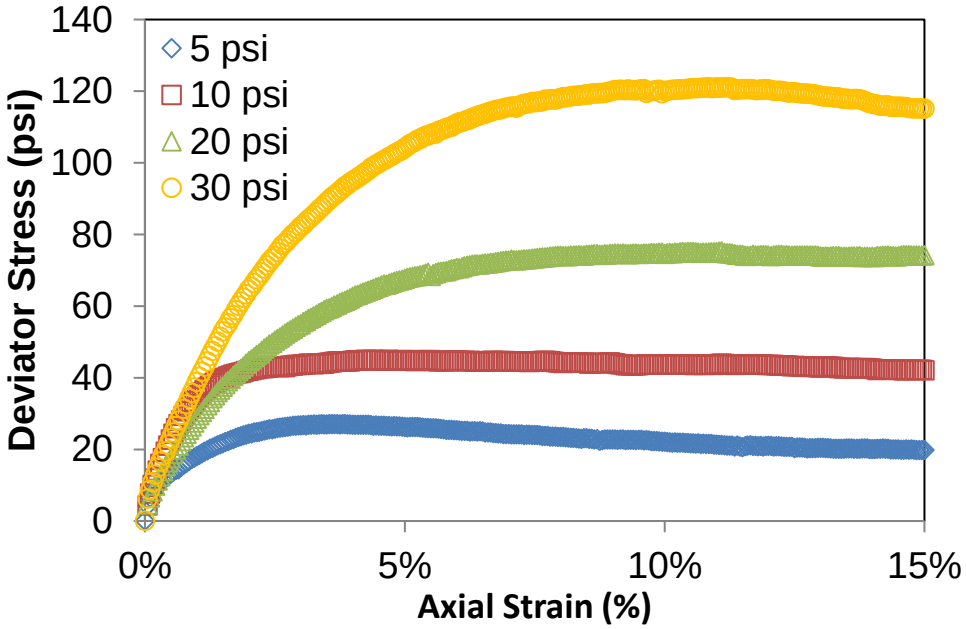

Figure 4-2: Deviator stress vs axial strain from 5, 10, 20, and 30 psi drained triaxial tests.

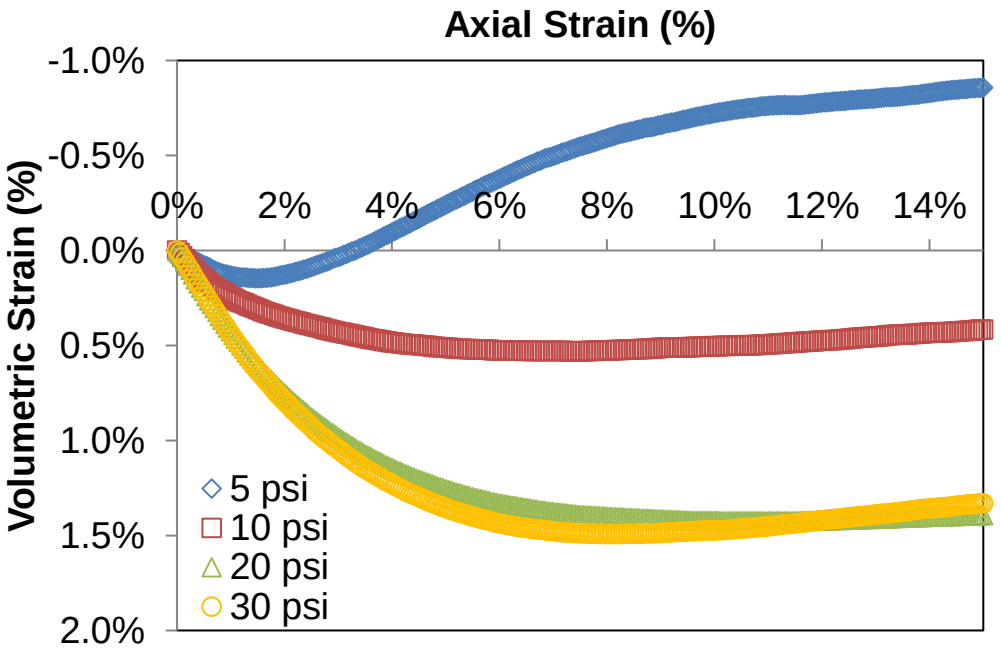

Figure 4-3: Volumetric strain vs axial strain from 5, 10, 20, and 30 psi drained triaxial tests.

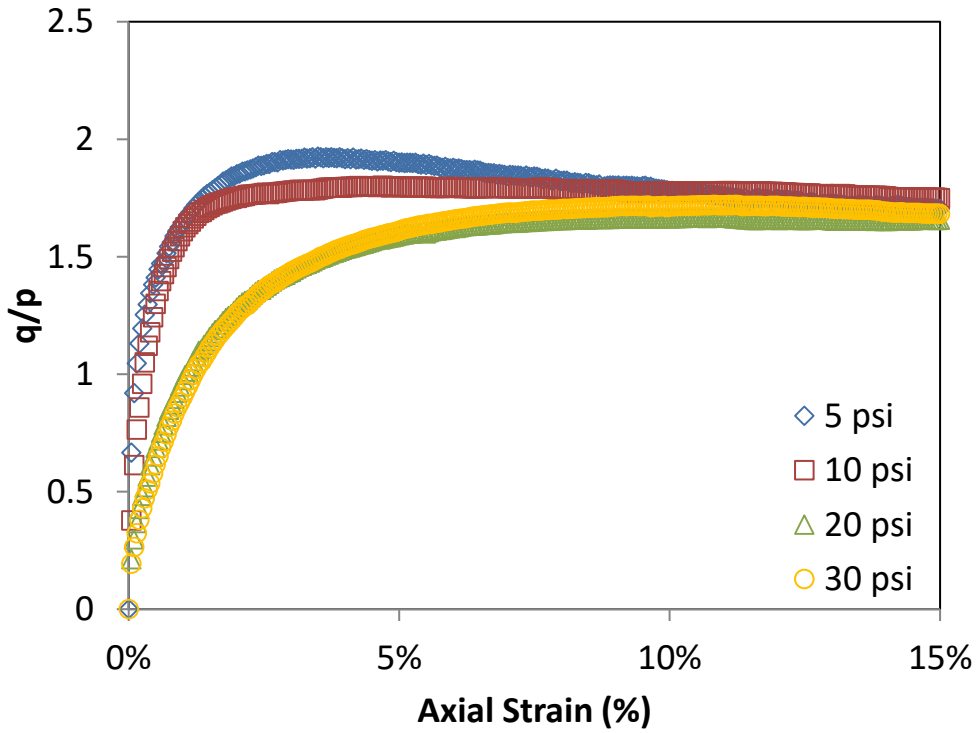

Figure 4-4: q/p vs axial strain.

From Figure 4-4, all four q/p curves appear to merge at about 15% axial strain suggesting that the soil samples are close to critical state at this juncture. The stress ratio at critical state, $R_{cs} = \sigma_1 / \sigma_3$, was estimated to be 4.71. By using the last points of the triaxial tests with confining

stresses of 5, 10 and 30 psi (34.5, 69 and 207 kPa) to construct the critical state line in Figure 4-5, the slope of the critical state line (CSL) (= λ) was estimated to be 0.022. The 20 psi (138 kPa) test was not used because the last point did not fall on the CSL.

It should be noted that the triaxial test samples were compacted to 95% relative compaction whereas the GRS backfill was compacted to 100% relative compaction.

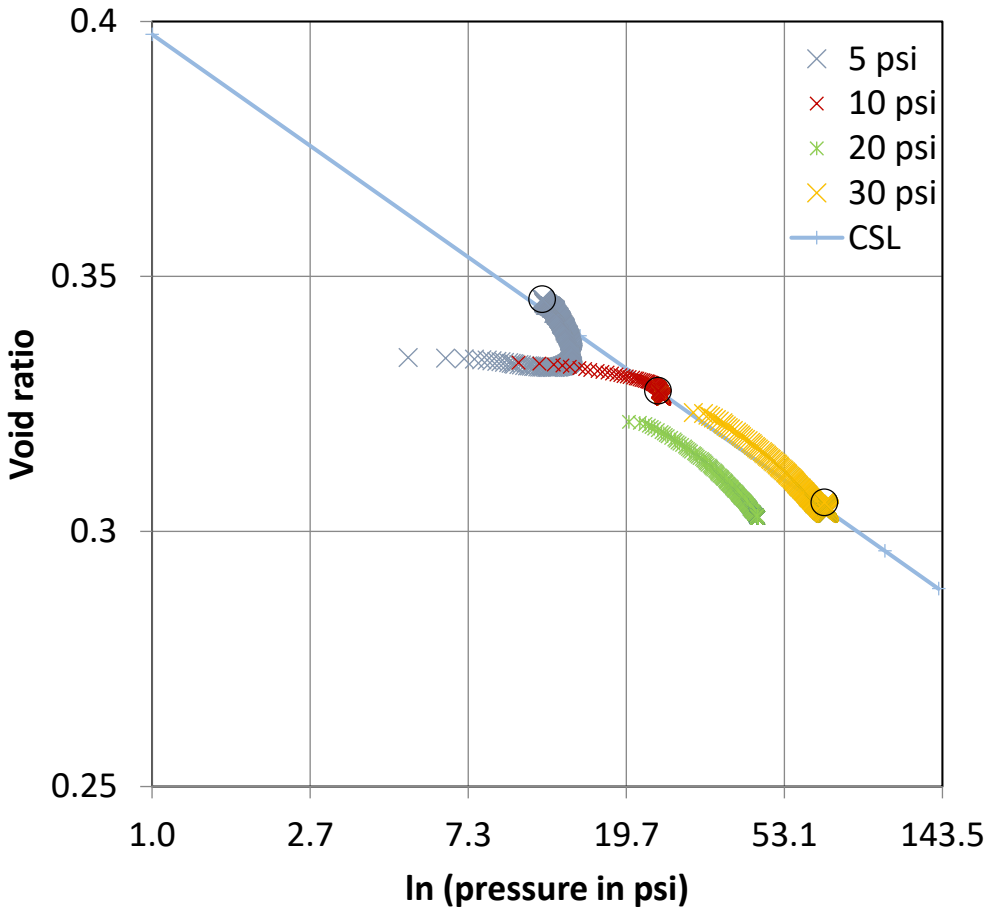

Figure 4-5: Progression of CD triaxial tests plotted on an e-ln p curve to estimate λ.

To determine the parameter N, the difference in void ratio between the NCL and CSL for a given mean stress p' must be found. Using Figure 2-3 (a)-(c), the void ratio of a soil on the CSL, e_{cs}, with a mean pressure of p' = p'_{cs} and a pre-consolidation pressure of p'_o is given by:

$$e_{CS} = N - \lambda \ln\left(p'_o\right) + \kappa \ln\left(\frac{p'_o}{p'_{CS}}\right) \qquad \text{(Equation 4.2)}$$

Figure 2-3 (a) shows that at critical state: $p' = p'_{cs} = p'_o/2$. Therefore,

$$e_{cs} = N - \lambda \ln\left(2p'_{cs}\right) + \kappa \ln(2)$$

The above equation can be rewritten as:

$$\Rightarrow \quad e_{cs} = N - (\lambda - \kappa)\ln(2) - \lambda \ln(p'_{cs}) \qquad \text{(Equation 4.3)}$$

Comparing Equation 4.3 to the NCL's equation, $e = N - \lambda \ln(p'_{cs})$, shows that the difference between the NCL and the CSL is $(\lambda - \kappa) ln(2)$. Therefore, using a void ratio on the CSL at one atmosphere of 0.338 and adding $(\lambda - \kappa) ln(2)$ gave N ≈ 0.355.

The last two subloading t_{ij} model parameters for the backfill of the GRS column are "a" and β. With the aid of an element simulation software called "Subloading t_{ij}", the triaxial test stress-strain and volume change curves can be simulated by varying the "a" and β parameters until the calculated and measured stress-strain and volume change curves were optimized for fit. From this exercise, $a = 150$ and $\beta = 1.2$ were found to yield the best fit as shown in figures 4-6 and 4-7.

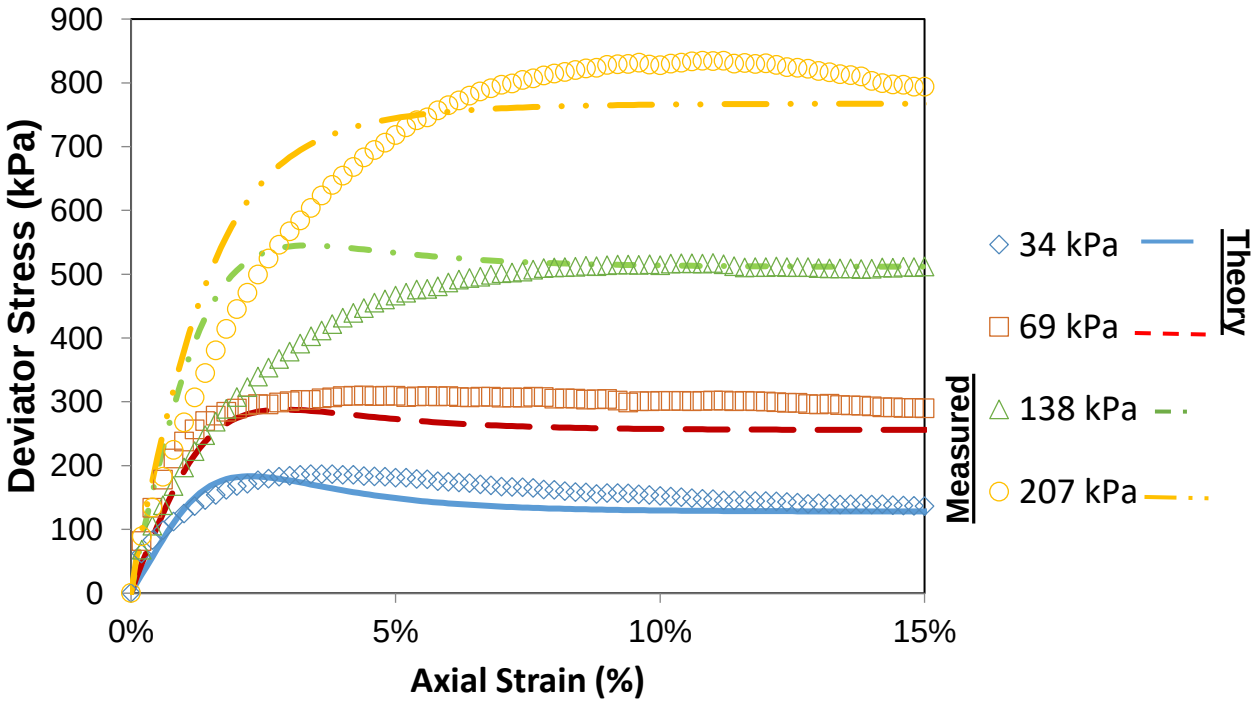

Figure 4-6: Measured vs subloading t_{ij} simulated curves of deviator stress vs axial strain.

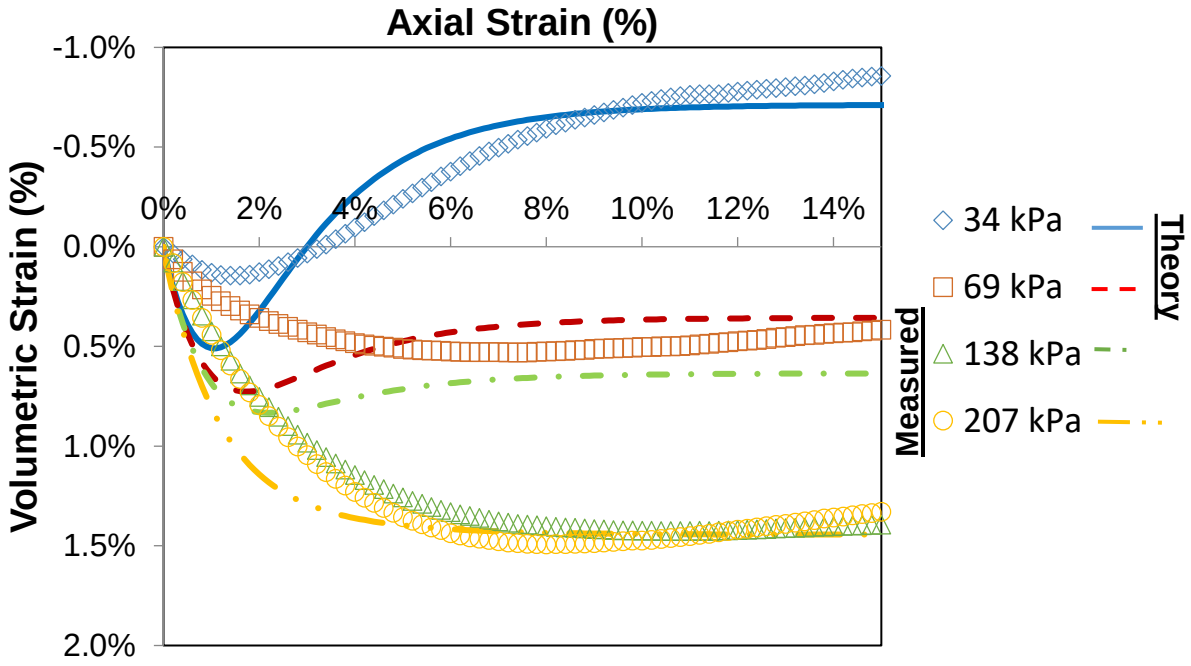

Figure 4-7: Measured vs subloading t_{ij} simulated curves of volumetric strain vs axial strain.

4.1.3 Soil Suction

The backfill in the GRS column performance test was unsaturated while the soil specimens in the triaxial tests were saturated. Therefore, the effects of soil suction can be approximated by imposing of an all-round confining stress on the GRS column. The magnitude of the confining stress is approximately $\chi(u_a - u_w)$, as seen in Equation 2.65.

A common way to estimate the matric suction of a soil is to use a SWCC. A computer program named SoilVision was used to generate one based on soil characteristics such as water content, void ratio, specific gravity and grain-size distribution.

Using the standard Proctor compaction curve (Figure 3-4), the water content at maximum dry density (146 pcf) was approximately 7.5%.

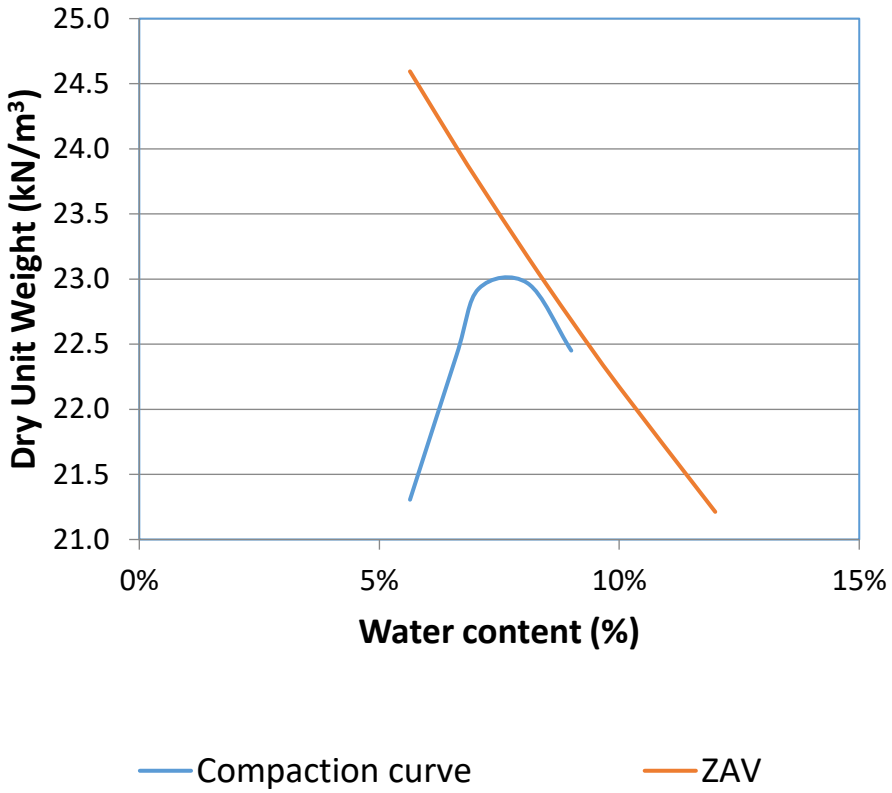

Figure 4-8: Measured compaction curve and G_s = 2.92 ZAV curve.

The specific gravity was estimated to be 2.92 based on the probable zero air void curve shown in Figure 4-8.

Values of 2.92, 0.245, and 7.5% for the specific gravity, void ratio and water content, respectively, along with the grain-size distribution were input into SoilVision. The software yielded an SWCC based on the Fredlund & Xing (1994) model as shown in Figure 4-9.

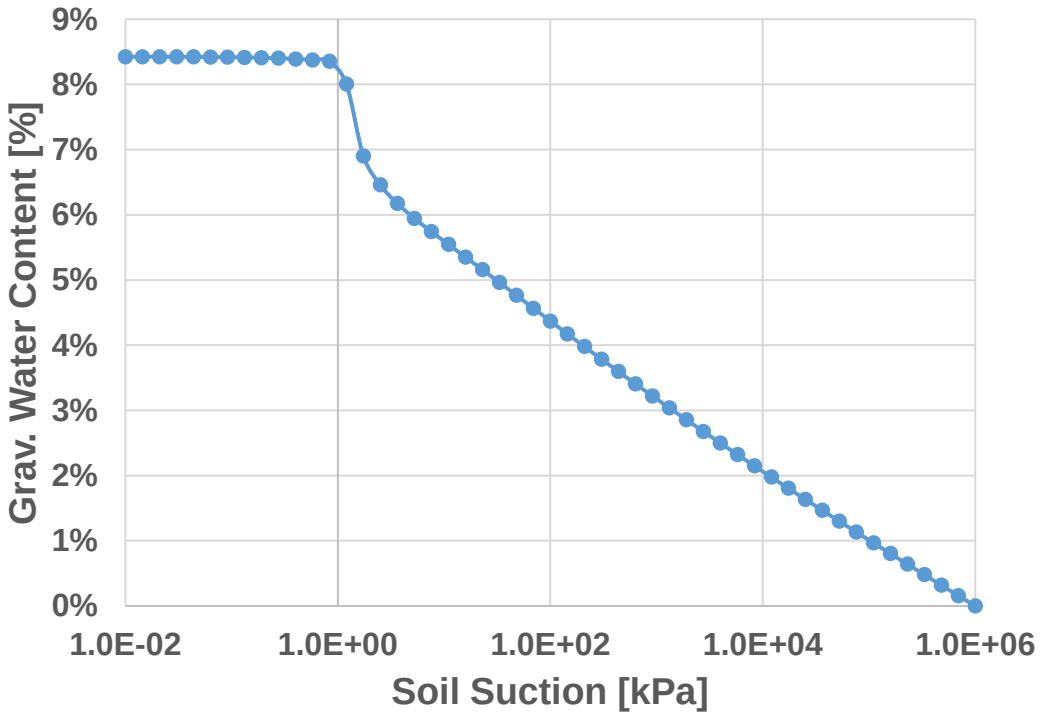

Figure 4-9: SWCC of GRS using the Fredlund & Xing fit (1994) in SoilVision.

Based on an as-compacted water content of 7.5%, the matric suction was estimated to be 1.45 kPa from Figure 4-9.

Bishop's effective stress parameter χ was then estimated by first determining the soil saturation to be 89.4% based on the optimum water content, void ratio corresponding to the maximum dry density and specific gravity. Then, using the residual water content from SoilVision of 5%, the residual saturation was estimated to be 59.6%. Finally, χ (see Equation 2.65) was calculated to be 73.7%. Therefore, multiplying χ with the matric suction of 1.45 kPa, the confining stress that should be applied to the GRS column should be 1.07 kPa. This confining stress is deemed negligible and thus will not be implemented in the numerical model.

4.2 CMU

The CMU blocks were tested by the National Concrete Masonry Association (NCMA). Each CMU block was 7⅝ x 7⅝ x 15⅝ inches and weighed about 42 lbs on average giving a unit weight of 80 pcf or 12.5 kN/m^3. The compressive strength of the concrete, f_c', was reported to be 5670 psi. The corresponding concrete Young's modulus can be estimated as follows (ACI, 2008):

$$E = 57000\sqrt{f_c'} \text{ (psi in USCS units)} \qquad \text{(Equation 4.4)}$$

The resulting Young's modulus was about 4292 ksi or 30 GPa. Finally, the shear modulus, G, can be estimated by dividing the Young's modulus by 2*(1+ν) where ν = Poisson's ratio. Assuming a Poisson's ratio of 0, the resulting shear modulus is 15 GPa. However, the CMU blocks crushed during the load test. To limit the compressive strength of the CMU, the CMU blocks were modeled as elasto-plastic assuming a Drucker-Prager failure criterion.

4.2.1 Drucker-Prager Model for CMU

The parameters for the Drucker-Prager failure criterion include cohesion, friction angle, and angle of dilatancy. Both the friction angle and angle of dilatancy were assumed to be 0, while the cohesion was assumed to be half the compressive strength of the CMU block.

Based on ASTM C90-12 standard to test three loadbearing CMU blocks on March 4th, 2013, the average gross cross-sectional area was 118.53 in^2, the average net cross-sectional area was 61.37 in^2, the average failure load was 347,610 lbs giving an average compressive strength of 2,930 psi. Therefore, the cohesion was half of this average compressive strength = 1465 psi or 10 MPa.

4.3 Geotextile

The load-deformation relationship of a fabric in a uniaxial tension test is commonly expressed as load/width vs. strain. Since E is the slope of load/area vs. strain curve in a uniaxial test, the slope of load/width vs. strain curve is E*thickness. In plane strain, the width is taken as 1 unit of length, hence E*A = E*thickness*1 = slope of load/width vs. strain curve. Using the geotextile properties in Table 3-2, the axial stiffness, EA, was calculated by dividing the width wide tensile strength, T_f, by the elongation, ε_f.

The EA range from 701 to 876 kPa based on ε_f of 10% and 8%, respectively giving an average of 790 kPa since the geotextiles were placed in an alternating pattern. However, assigning only an axial stiffness, EA, for the geotextile would imply that it would behave in a linear elastic fashion. Due to the fact that the geotextiles ripped during the load test, its strength should be limited in the numerical model.

4.3.1 2-D FEM: Truss Elements

A strain-softening elastoplastic model is considered most appropriate for the geotextiles. The geotextiles will have a slope of EA for their load-deformation curve when the tensile loads are less than the tensile strength of the geotextile. However, once the tensile force in the geotextile reaches the tensile strength, the geotextile strain softens by the following exponential decay function:

$$\frac{T}{T_y} = exp(-\chi\varepsilon) \qquad \text{(Equation 4.5)}$$

where T = tensile force in geotextile, T_y = geotextile tensile strength, ε = geotextile strain and χ = parameter that controls the rate of exponential decay. This model is best illustrated with the aid of Figure 4-10.

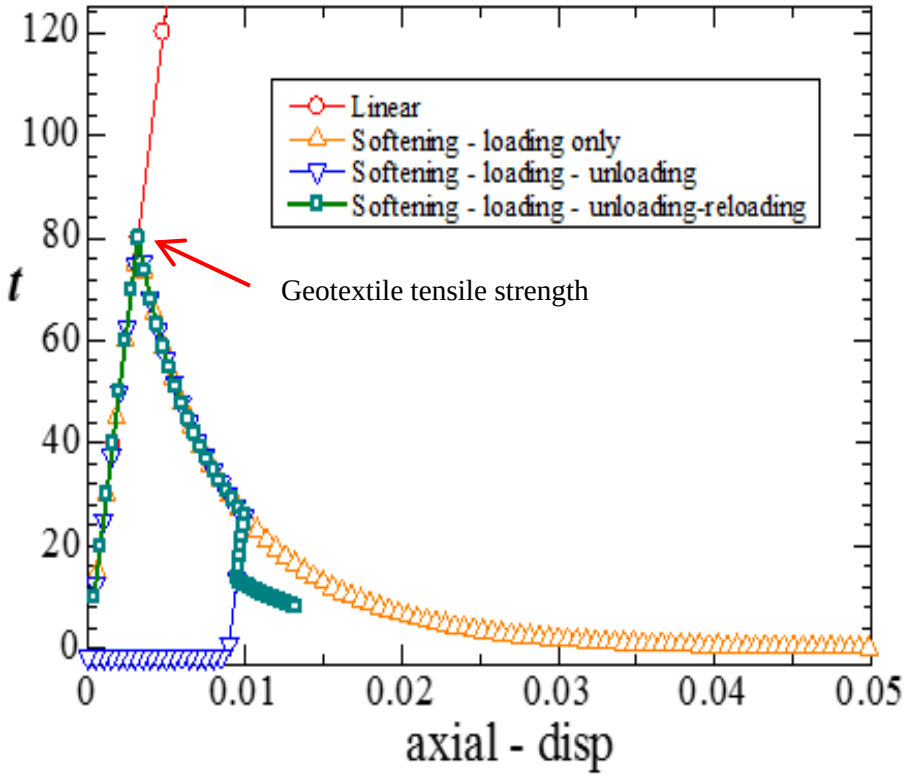

Figure 4-10: Geotextile wide width tensile force vs axial strain.

Using a geotextile tensile strength of 70 kN/m (4800 lb/ft) from Table 3-2, a sensitivity analysis of the parameter χ, is presented in the next section. In the model shown in Figure 4-10, it can be seen that the geotextile is restrained from supporting compressive forces.

4.3.2 Sensitivity of Parameter χ

To determine the ideal value for the exponential decay parameter χ, a FEMtij-2D analysis was conducted to axially stretch a 4-m-long geotextile by 0.61 m (2 ft) over 500 steps. The axial stiffness and tensile strength of the geotextile used in the GRS load tests were 790 kPa (80.5 tn/m^2) and 70 kN/m (7.14 tn/m), respectively. Values of χ were varied between 2 and 500 but it was found that when $\chi \geq 12$, there were numerical difficulties in the software that precluded the geotextile from strain softening. Therefore, the parameter χ was varied between 2 and 11 in the sensitivity analysis. However, $\chi = 11$ showed more strain softening than when $\chi = 10$ which is contrary to what is expected. Consequently, $\chi = 11$ was discarded due to numerical instability in reaching a solution. Therefore, the results of the sensitivity analysis is displayed in Figure 4-11 where the tensile force was plotted against the axial displacement for χ values of 2, 5, and 10.

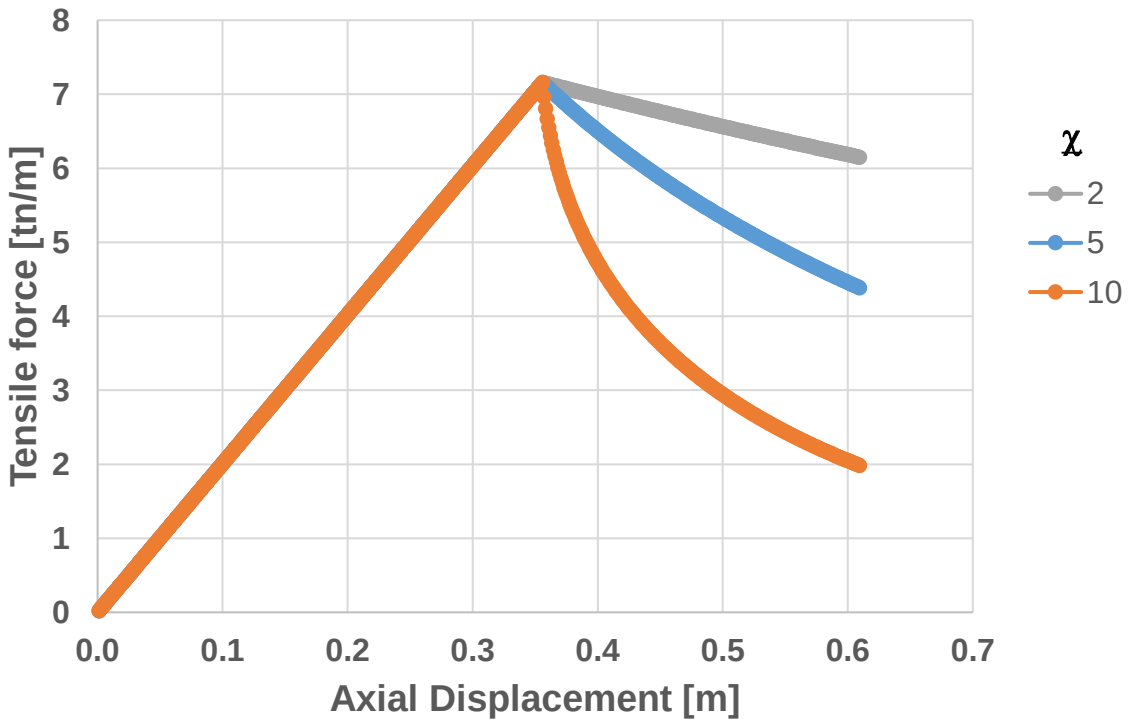

Figure 4-11: Sensitivity of parameter χ using a single geotextile.

As shown in Figure 4-11, χ = 10 displayed the most post-yield strain softening compared to the other values.

The above sensitivity analysis was performed for a single geotextile. A sensitivity analysis of χ was also performed on the GRS load test since to study its effects on the post-yield softening behavior. Figure 4-12 shows the load-settlement curves of these numerical load tests.

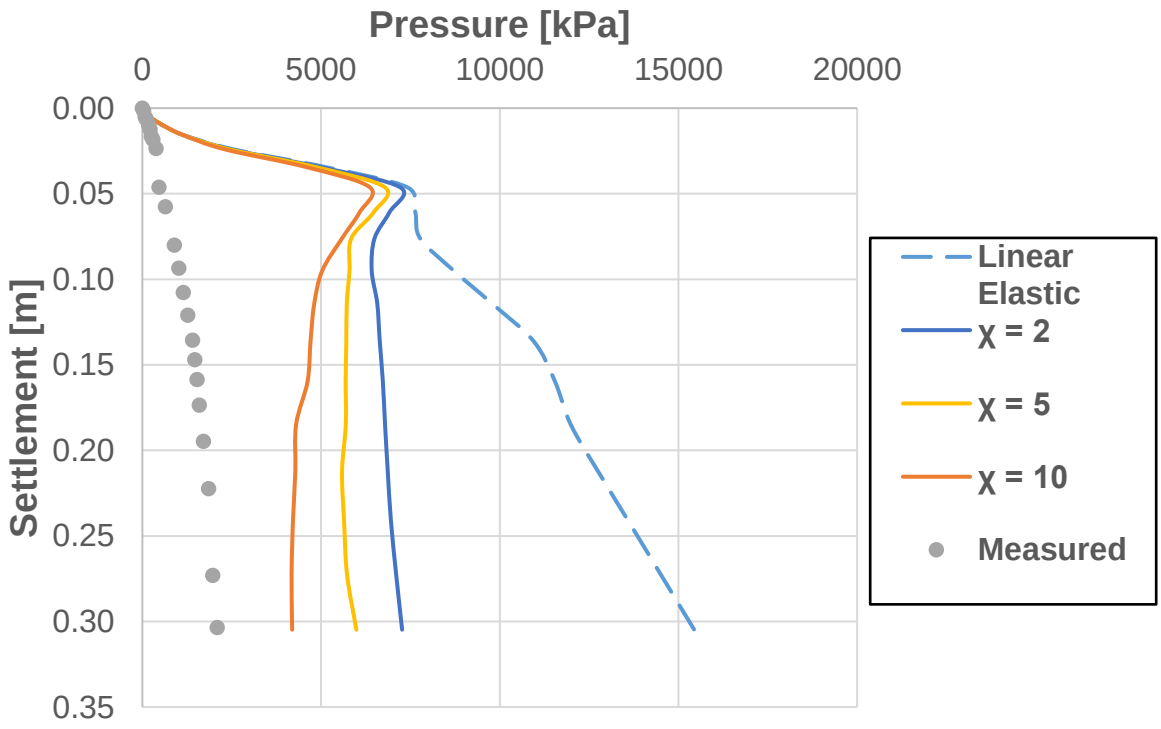

Figure 4-12: Sensitivity of parameter χ using load-settlement curves from 2-D numerical load tests.

Figure 4-12 confirms that χ = 10 shows the most strain softening compared to the other values.

4.3.3 3-D FEM: Membrane Elements

For the 3-D numerical model of the GRS load test, the geotextiles were modeled as membrane elements, which require specification of finite lengths in all three directions, Young's modulus and Poisson's ratio. The geotextile must also be restrained from supporting compressive forces. The post-yield softening of the membrane elements were not modeled in time for the duration of this thesis work. Therefore, only linear elastic membrane elements were used in the 3D analyses..

4.4 Joint Elements

Joint elements, also known as interface elements, describe the frictional interaction between two different materials. These interfaces include geotextile – soil, concrete – soil, and geotextile – CMU.

4.4.1 Concrete-Soil Interface

The interface between the footing and soil was assumed to be similar to the interface between the CMU and soil. This interface friction angle is commonly taken as ⅔ times the peak friction angle of the soil in practice since the concrete is smooth (cast with formwork). The interface friction angle for the concrete - soil interface was measured by FHWA to be 33° . The peak friction angle of the soil at 100% relative compaction measured in a direct shear box was 53° (Iwamoto, 2013). The measured interface friction angle of 33° is reasonable since it is close to ⅔ times 53° = 35°.

4.4.2 Geotextile-Soil Interface

For sands, the geotextile – soil interface friction angle varies from 77% to 87% of the soil's peak friction angle (Martin et al., 1984). Therefore, from drained direct shear test, the peak friction angle of the GRS column backfill was 53°. Gravel particles are larger than sand. It was decided to adopt a more conservative interface friction angle ratio than for sands. A geotextile – soil interface friction angle of 38° corresponding to 72% of the soil's peak friction angle is adopted herein.

4.4.3 Geotextile-CMU Interface

The interface friction angle for the geotextile – CMU interface was measured by FHWA to be 35°.

4.5 Summary

The following is a summary of the parameters used in the FEM modelling of the GRS column load test:

Table 4-1: Material properties used in the finite element analyses.

Soil		
Item (Symbol)	**Value**	**Units**
a	150	-
β	1.2	-
λ	0.022	-
κ	0.00161	-
R_{CS}	4.71	-
N	0.355	-
Poisson's Ratio (ν)	0.2	-
Geotextile		
Item (Symbol)	**Value**	**Units**
Axial Stiffness (EA)	790	kPa
Tensile Strength (T_y)	70	kN/m
Exp. Decay Parameter (*x*)	10	-
CMU		
Item (Symbol)	**Value**	**Units**
Young's modulus (E)	30	GPa
Shear Modulus (G)	15	GPa
Unit Weight (γ)	12.5	kN/m^3
Poisson's Ratio (ν)	0	-
Cohesion[2] (c)	10	MPa
Friction Angle (ϕ)	0	°
Angle of Dilatancy (ψ)	0	°
Footing		
Item (Symbol)	**Value**	**Units**
Young's modulus[3] (E)	3.00E+11	kPa
Shear Modulus (G)	1.50E+11	kPa
Poisson's Ratio (ν)	0	-
Unit Weight (γ)	27.7	kN/m^3
Interface Friction Angle, δ		
Item	**Value**	**Units**
Geotextile - Soil	38	°
Concrete - Soil	33	°
Geotextile - CMU	35	°

Notes: 1) Stiffness ratio is defined as the geotextile stiffness after the tensile force exceeds the tensile strength to that before.
2) Assume cohesion, c = 0.5 x compressive strength of CMU.
3) A very large footing modulus is used to force the footing to settle uniformly.

5 FINITE ELEMENT ANALYSIS

FEMtij-2D and FEMtij-3D were used for numerical modelling of the GRS column load test in 2-D and 3-D, respectively. FEMtij-2D was used to first evaluate the effects of several factors that can affect the load-settlement curve and the lateral displacement profile. Plane strain conditions were assumed in the 2D analysis. Strictly, it is not correct to represent the GRS column test in 2D. However, this was performed as part of a sensitivity analysis on the parameters that can affect the analysis results because 2D analyses are quicker and easier to run. This was followed by 3D analyses which better mimics the physical tests themselves.

5.1 2-D Plane Strain Analysis

For the 2-D plane strain FEM model of the GRS column load test, only half the footing and GRS need to be considered to save computational time. The mesh for TF-6, shown in Figure 5-1, has 792 nodes and 808 elements to represent the soil, footing, CMU blocks, geotextiles and the various interfaces. The boundary conditions are fixed at the bottom to model the concrete strong floor on which the load tests were conducted, and rollers were introduced along the line of symmetry. TF-7 was modelled with the same mesh in FEMtij-2D by switching the material parameters of the CMU blocks to “air” before applying the vertical load.

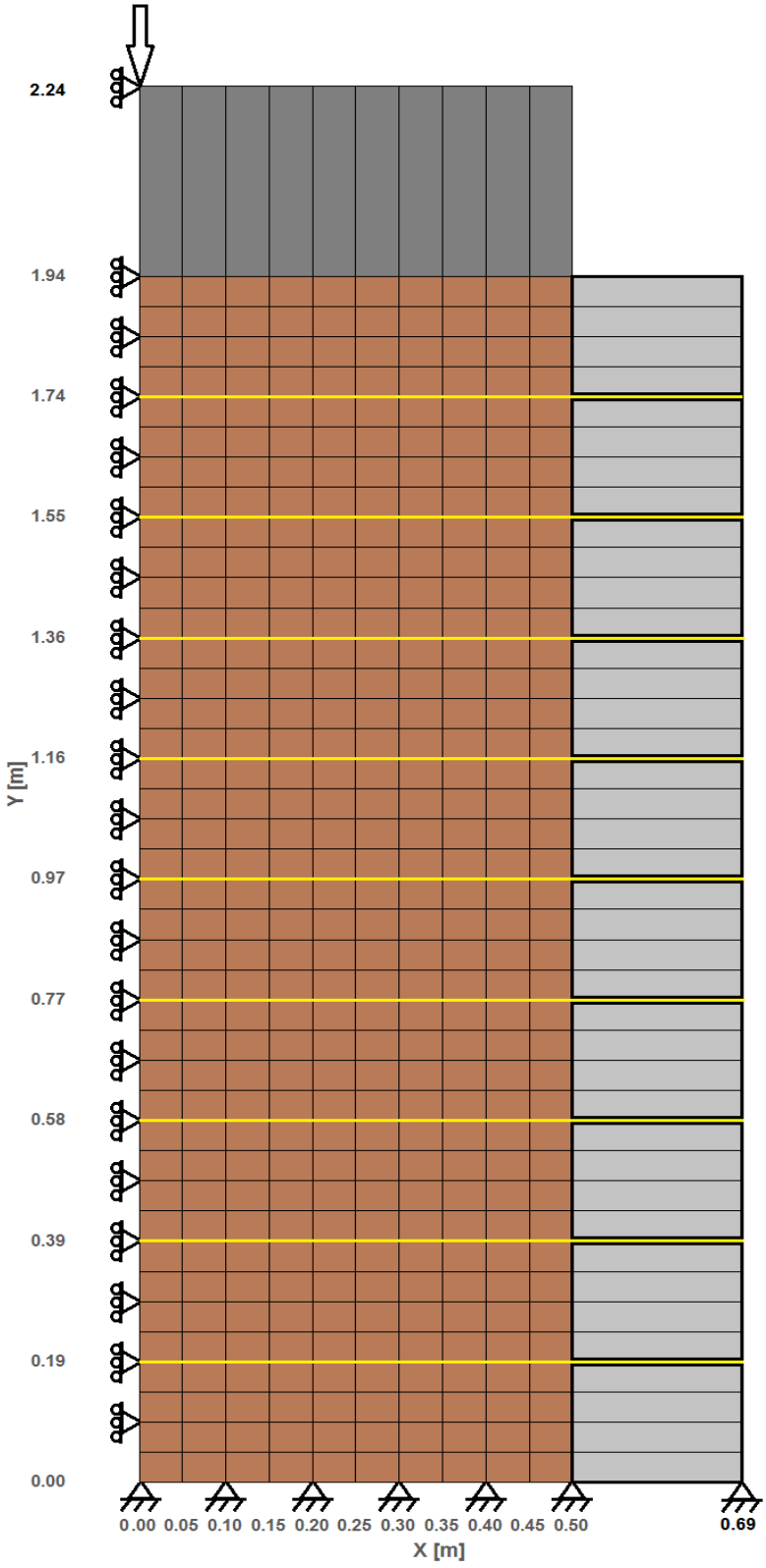

Figure 5-1: 2-D Mesh with dimensions.

An input file called "Ground.dat" containing the geometry, (node and element data), and material parameters was generated. Gravity was then turned on for the soil elements while all the other elements had the properties of "air." Then, gravity was turned on for the CMU blocks alone while all the other elements had the properties of "air." The purpose of this process was to give all elements a weight and density, which is known as "making the ground" phase. This phase is analogous to compacting each lift to build up the GRS column, and to ensure optimum compaction before the performance test. The output file called "Ground.cal" was then analyzed to check if the void ratio in the middle of the GRS backfill is the same as the void ratio calculated from the compaction curve at optimum in Figure 3-4: i.e.; optimum dry unit weight of 23 kN/m^3 (146 pcf) corresponding to a void ratio of 0.245. To achieve this, the initial void ratio was varied in the input file until the output file's soil elements at the GRS mid-height had a final void ratio of around 0.245.

The numerical load test was then conducted using the weight and density from the Ground.cal file and applying a foot of displacement at the top of the footing over 90,000 increments. In all runs, the soil was modeled using the subloading t_{ij} model. With this input file, a base case scenario was established and several analyses were made to study the effects of the following factors:

1. Footing friction;
2. Constitutive model for the CMU blocks; and
3. Constitutive model for the geotextile.

In the base case scenario, the constitutive models for the CMU blocks, geotextile, and footing are the Drucker-Prager, linear elastic with post-yield softening, and linear elastic models, respectively. Furthermore, the base case footing-soil interface friction angle was taken to be 33°, which is approximately 2/3 the peak friction angle of the soil. With the exception of the fact that the model is 2D, this base case is deemed most ideal for a GRS load test.

5.1.1 Effects of Footing-Soil Friction

In reality, the soil-footing friction angle (δ) lies between 0 and ϕ, the peak soil friction angle. For a "smooth" footing (i.e., concrete cast with formwork) on soil, it is common practice

to assume $\delta = 2\phi/3$ ($\approx 33^{\circ}$). The effects of friction angle between the footing and the GRS backfill for both TF-6 and TF-7 are shown in the following figures.

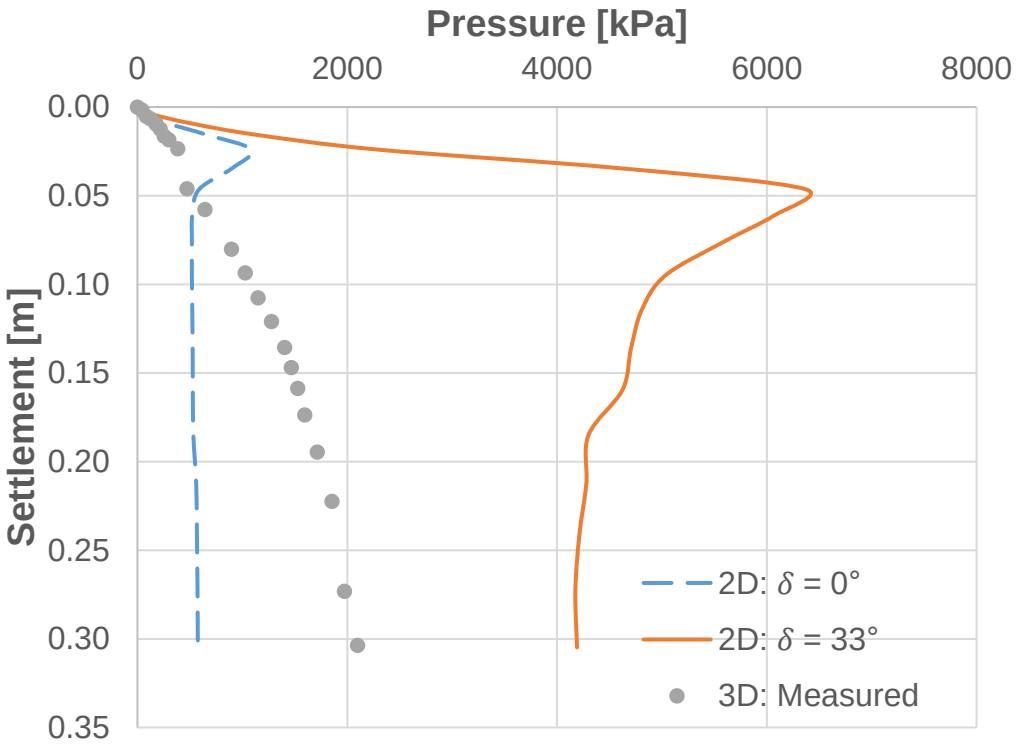

Figure 5-2: Effect of soil-footing friction angle on the TF-6 load-settlement curve.

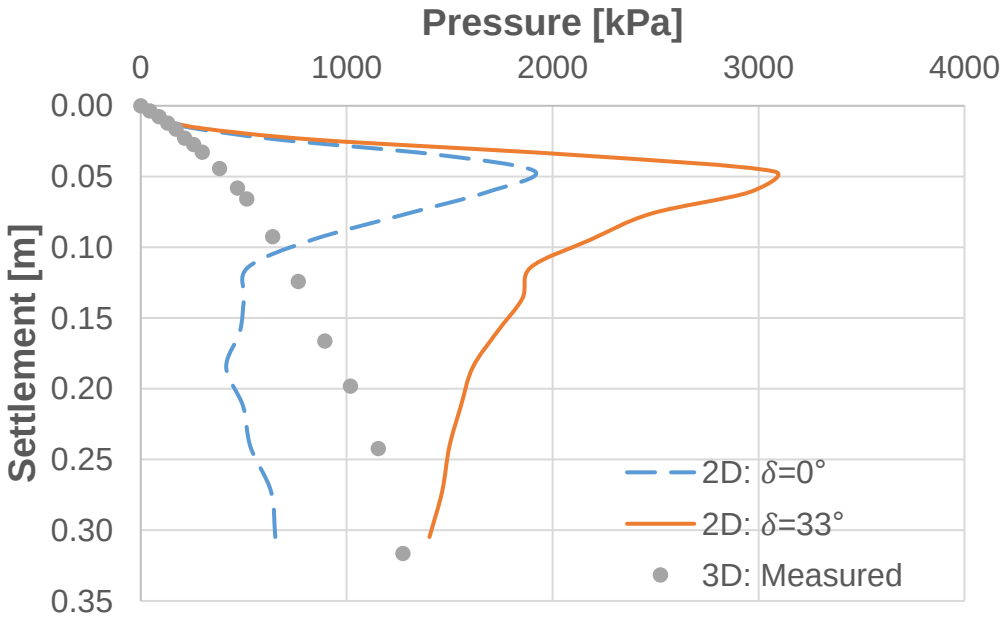

Figure 5-3: Effect of soil-footing friction angle on the TF-7 load-settlement curve.

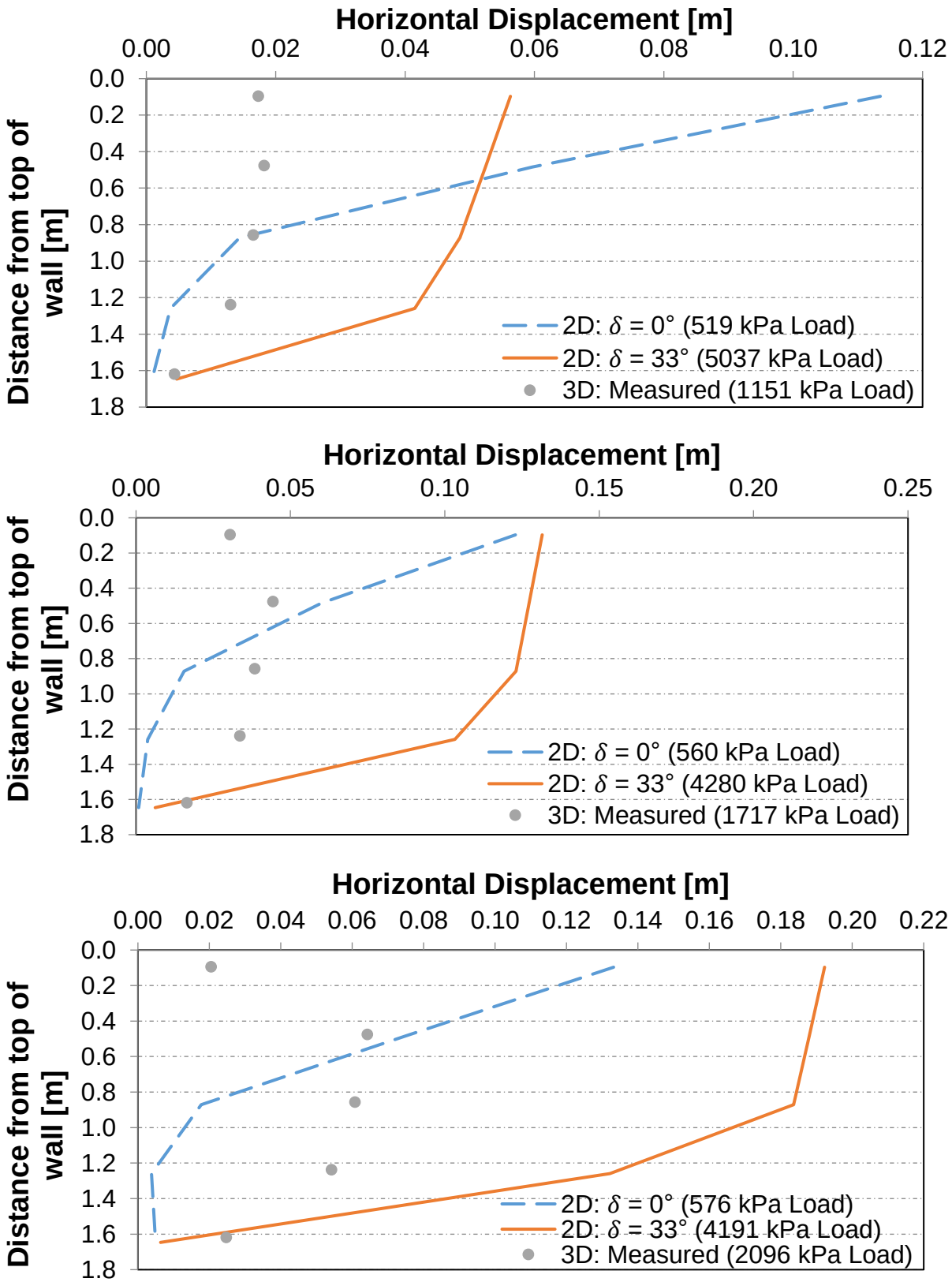

Figure 5-4: Effects of soil-footing friction angle on the TF-6 lateral displacement curve at 4, 8, and 12 inches of settlement, respectively.

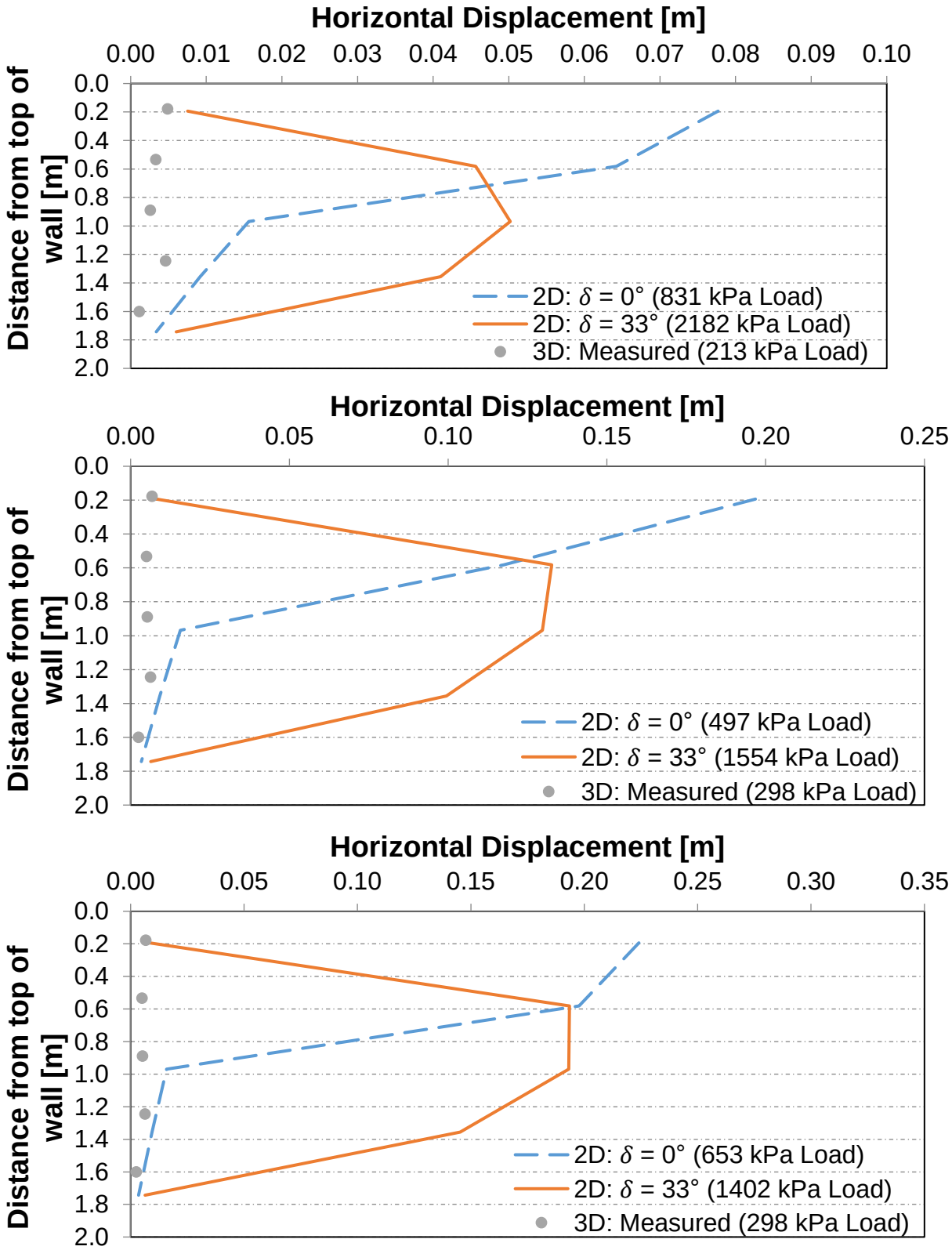

Figure 5-5: Effects of soil-footing friction angle on the TF-7 lateral displacement curve at 4, 8, and 12 inches of settlement, respectively.

It can be seen that as the friction angle increased from 0˚ to 33˚, the GRS capacity increased significantly. Also, as expected in figures 5-2 and 5-3, the measured GRS columns have a smaller capacity than the infinitely long GRS. This is to be expected as the additional confinement available on two sides of an infinitely long GRS increases the capacity as compared to a column GRS.

The lateral displacement profiles are also quite different for the two different values of footing friction angle as shown in figures 5-4 and 5-5 for TF-6 and TF-7, respectively. In TF-6, the calculated maximum lateral displacement occurred at the top of the GRS while the measured maximum lateral displacement occurred at height of about 0.75H from the bottom of the GRS. Also, the calculated lateral displacement profile for a footing friction angle of 0˚ concaved up while the calculated lateral displacement profile for a footing friction angle of 33˚ convexed up.

In TF-7, the maximum lateral displacement occurred at the top of the GRS for the measured and for the calculated with a footing friction angle of 0˚ while the maximum lateral displacement occurred at mid-height for the calculated with a footing friction angle of 33˚.

5.1.2 Effects of Properties of Facing

During the load test, it was observed that some of the CMU blocks crushed. Consequently, it is important to model the crushing of the CMU using an elasto-plastic model like Mohr-Coulomb or Drucker-Prager instead of linear elastic. Therefore, Kaya et al. (2016) analyzed the CMU elements of TF-6 using the Mohr-Coulomb model, as seen in the load-settlement curve of Figure 5-6. However, since the Drucker-Prager model is easier to program than the Mohr-Coulomb model and since the plan was to modify FEMtij-3D to incorporate an elasto-plastic constitutive model for the CMU later on, FEMtij-2D analyses was also conducted by modeling the CMU as Drucker-Prager elements to facilitate a direct comparison between 2D and 3D analyses. Results of the Drucker Prager CMU are also shown in Figure 5-7. The properties of the CMU are summarized in Table 4-1.

A comparison of the load-settlement and lateral displacement curves when the CMU was modeled as linear elastic versus elasto-plastic (Drucker-Prager model) is shown in figures 5-7 and 5-8 for TF-6.

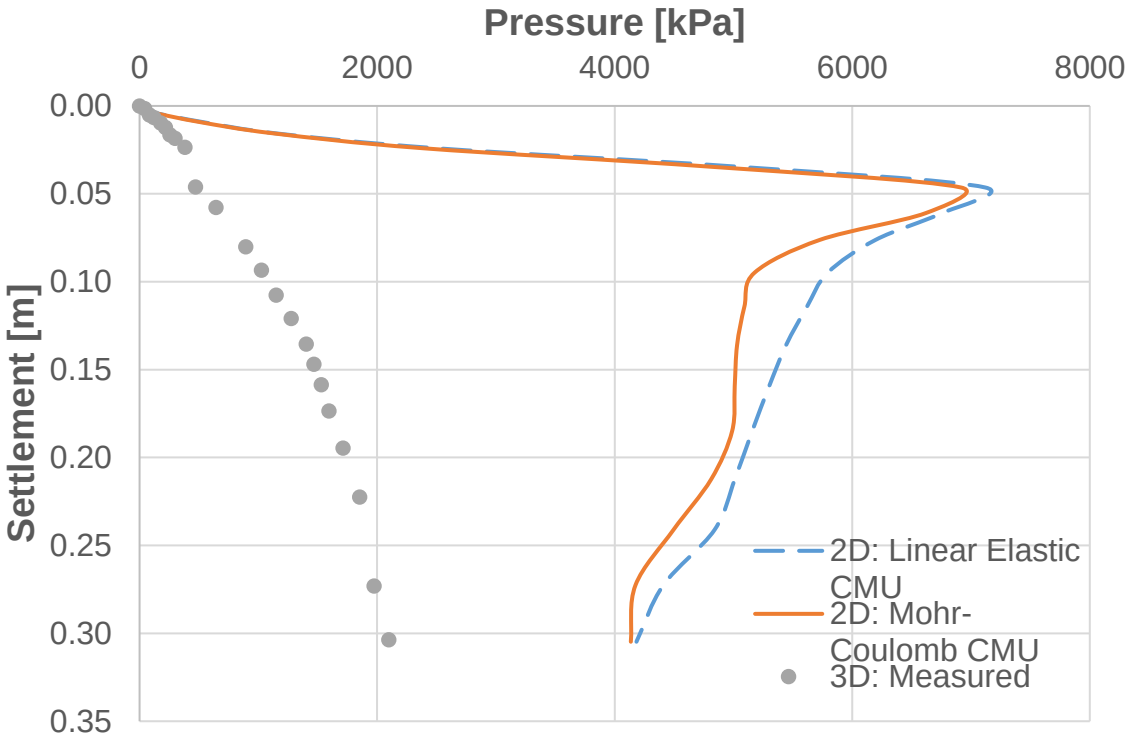

Figure 5-6: Effect of Mohr-Coulomb CMU properties on the TF-6 load-settlement curve (Kaya et al., 2016).

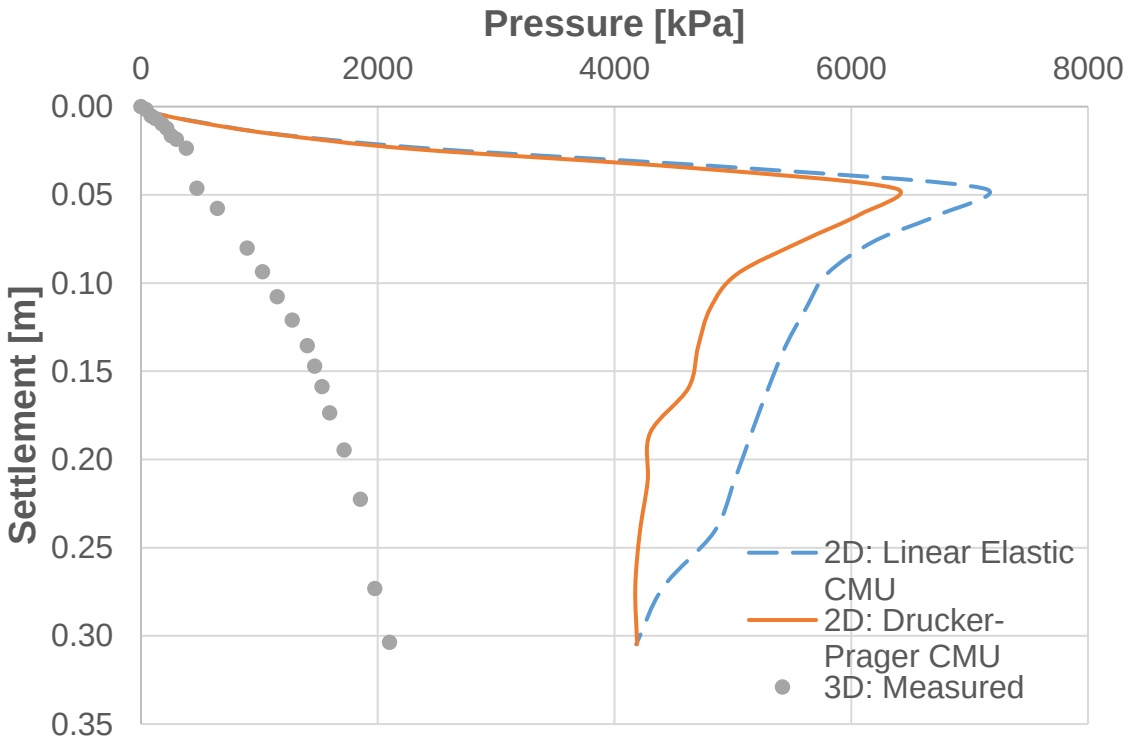

Figure 5-7: Effect of CMU properties on the TF-6 load-settlement curve.

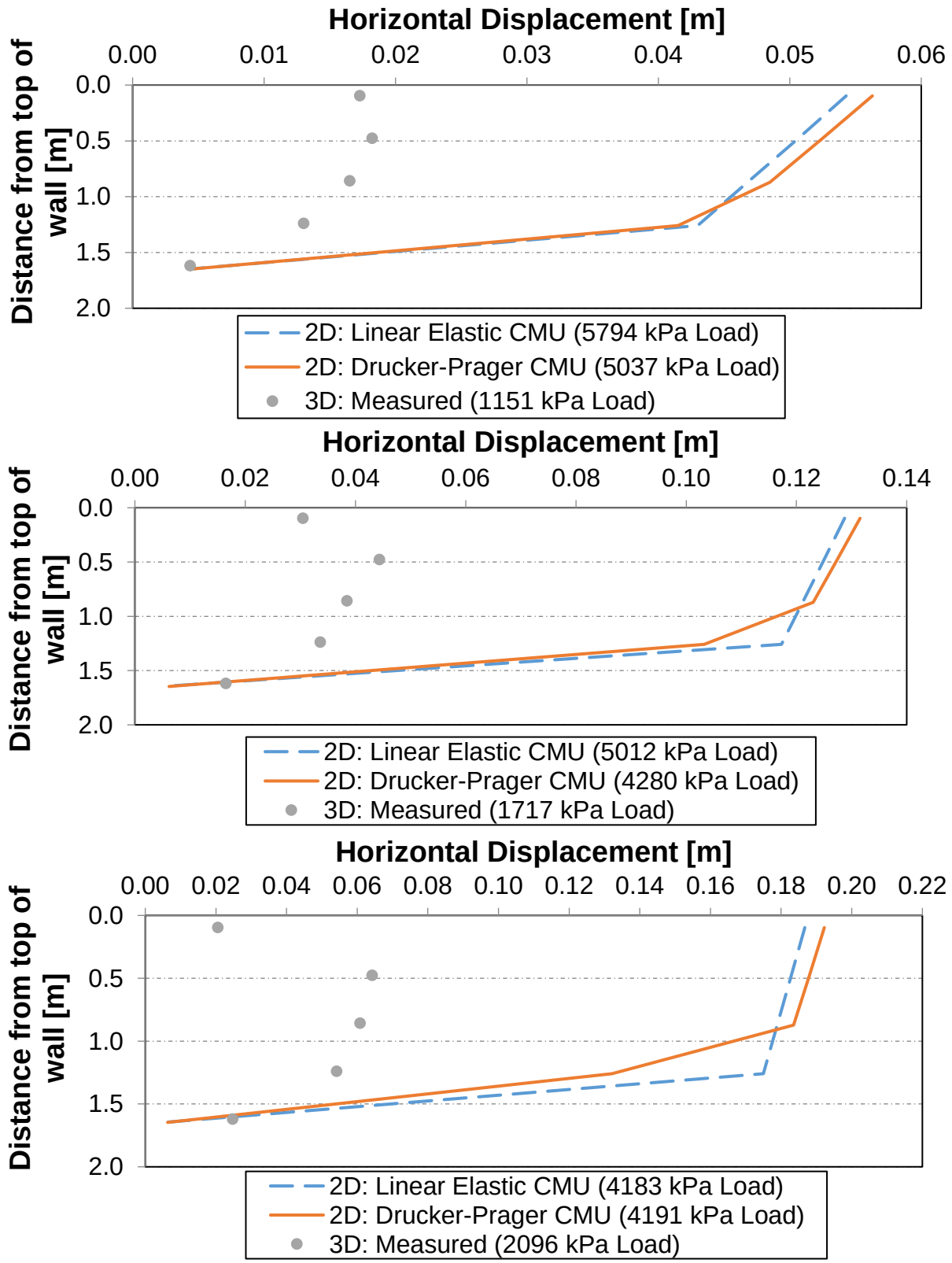

Figure 5-8: Effects of CMU properties on the TF-6 lateral displacement curve at 4, 8, and 12 inches of settlement, respectively.

As expected, a linear elastic CMU yields a higher GRS capacity than the Drucker-Prager CMU. However, the difference in the lateral displacement profiles is not very significant. Also, it can be seen that the GRS with Mohr-Coulomb CMUs yield a slightly higher capacity than that with Drucker-Prager CMUs.

5.1.3 Effects of Properties of Geotextile

Due to the geotextiles ripping during the GRS column performance test, the linear elastic geotextile with post-yield softening model, described in Section 4.3.1, should be used to simulate that behavior. A comparison of the GRS behavior was performed using the post-yield softening geotextile versus a linear elastic geotextile. Figures 5-9 and 5-10 show the effects of the geotextile properties on TF-6 and TF-7's load-settlement curves, respectively while figures 5-11 and 5-12 show the effects of the geotextile properties on TF-6 and TF-7's lateral displacement profiles.

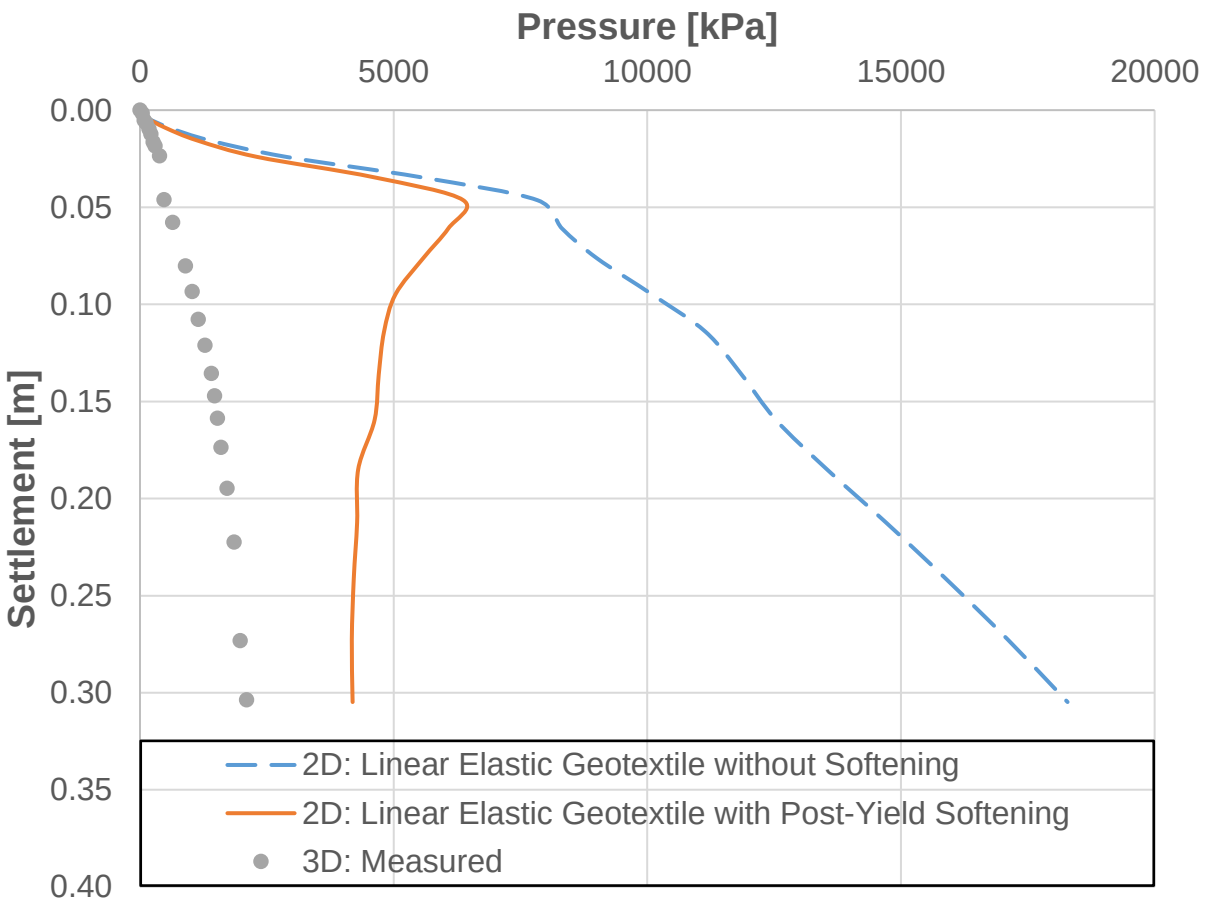

Figure 5-9: Effect of geotextile properties on the TF-6 load-settlement curve.

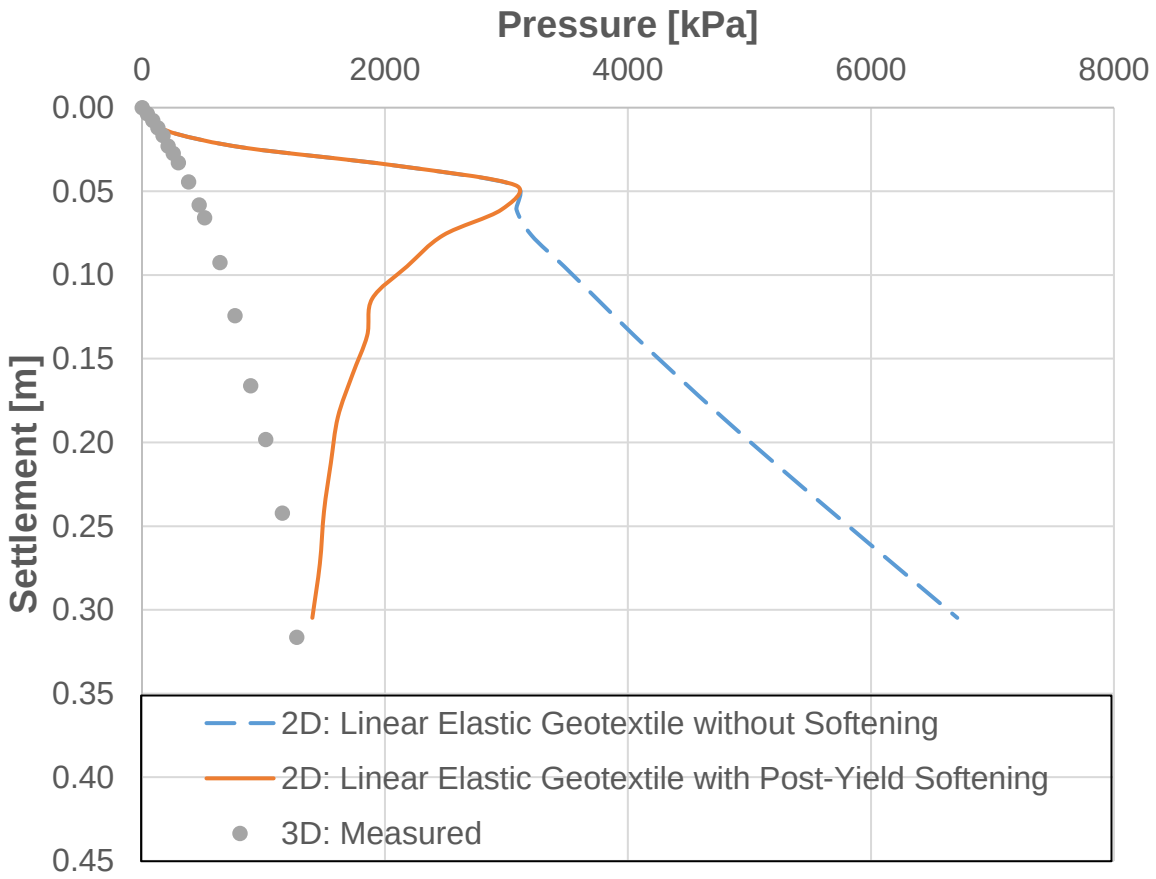

Figure 5-10: Effect of geotextile properties on the TF-7 load-settlement curve.

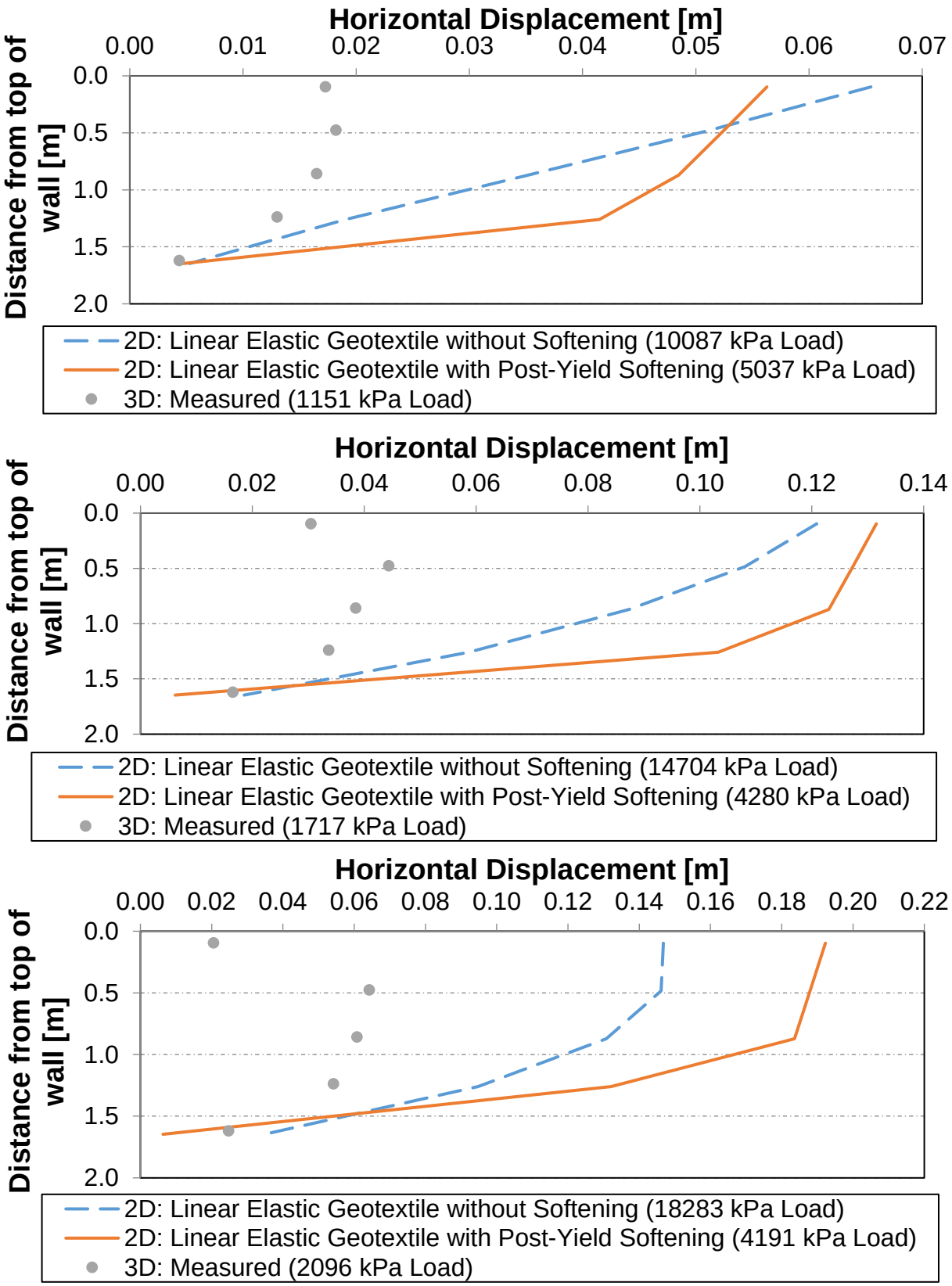

Figure 5-11: Effects of geotextile properties on the TF-6 lateral displacement curve at 4, 8, and 12 inches of settlement, respectively.

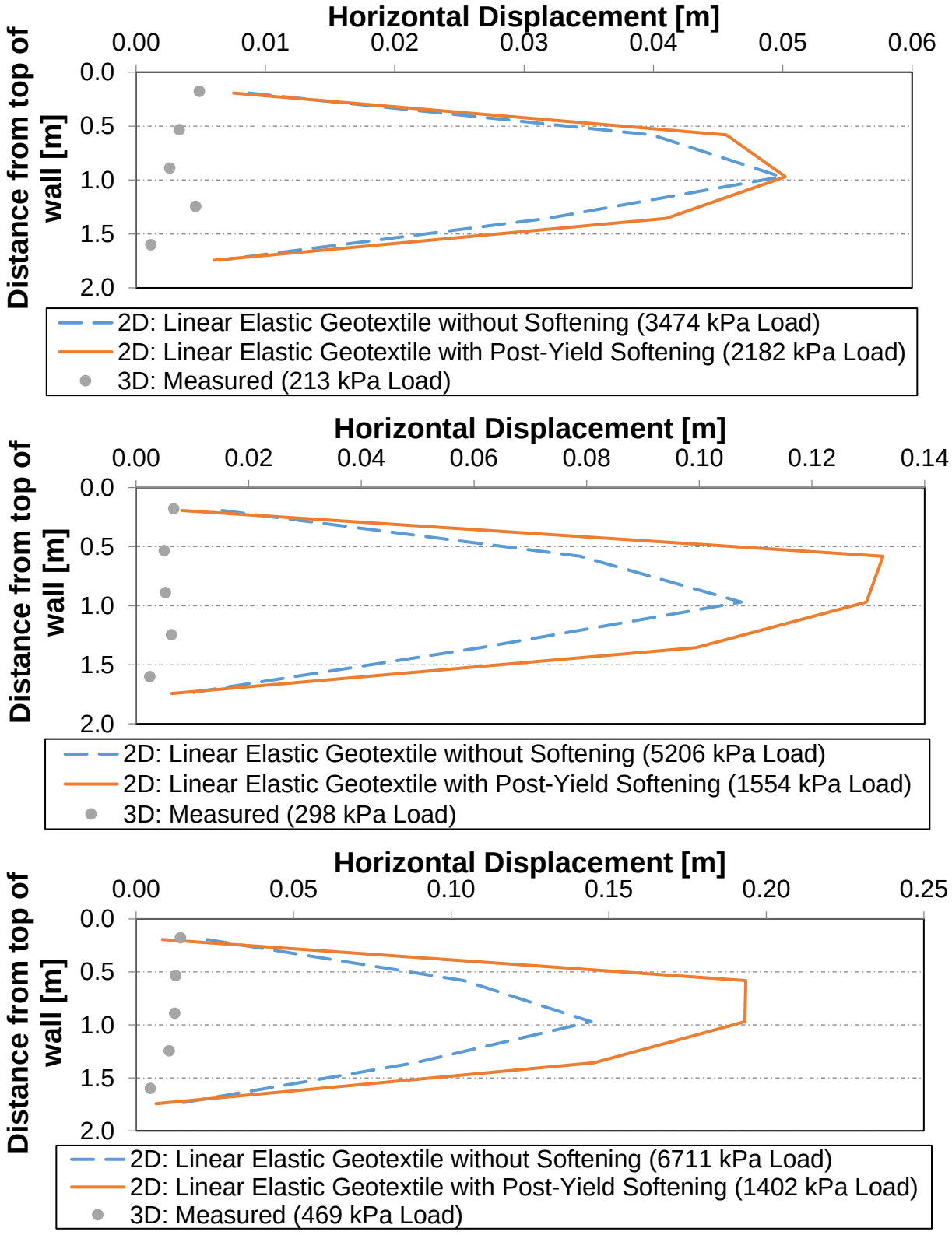

Figure 5-12: Effects of geotextile properties on the TF-7 lateral displacement curve at 4, 8, and 12 inches of settlement, respectively.

As shown in figures 5-9 and 5-10, TF-6 and TF-7 exhibit a softening in the load-settlement behavior when the geotextile was allowed to soften while the GRS with the linear elastic geotextile strain hardened after yielding. Also, TF-6 with the linear elastic geotextile behaved slightly stiffer in the initial part of the load-settlement curve than that with the post-yield softening model. However, the geotextile properties do not change the stiffness of the initial part of the load-settlement curve for TF-7. This implies that the geotextiles in TF-7 did not yield until an applied pressure of about 3075 kPa was reached.

From figures 5-11 and 5-12, the lateral displacements are more subdued for the GRS with the linear elastic geotextile. This is to be expected since the linear elastic geotextile cannot tear and lose its strength.

5.1.4 Shear band Formation in 2D FEM

Shear bands in the GRS can be discerned from the heat maps of shear strains in figures 5-13 and 5-14 for TF-6 and TF-7, respectively. These plots correspond to the last calculation step of the FEM analyses. As seen from these figures, the shear bands are inclined at 50° and 45° in TF-6 and TF-7, respectively.

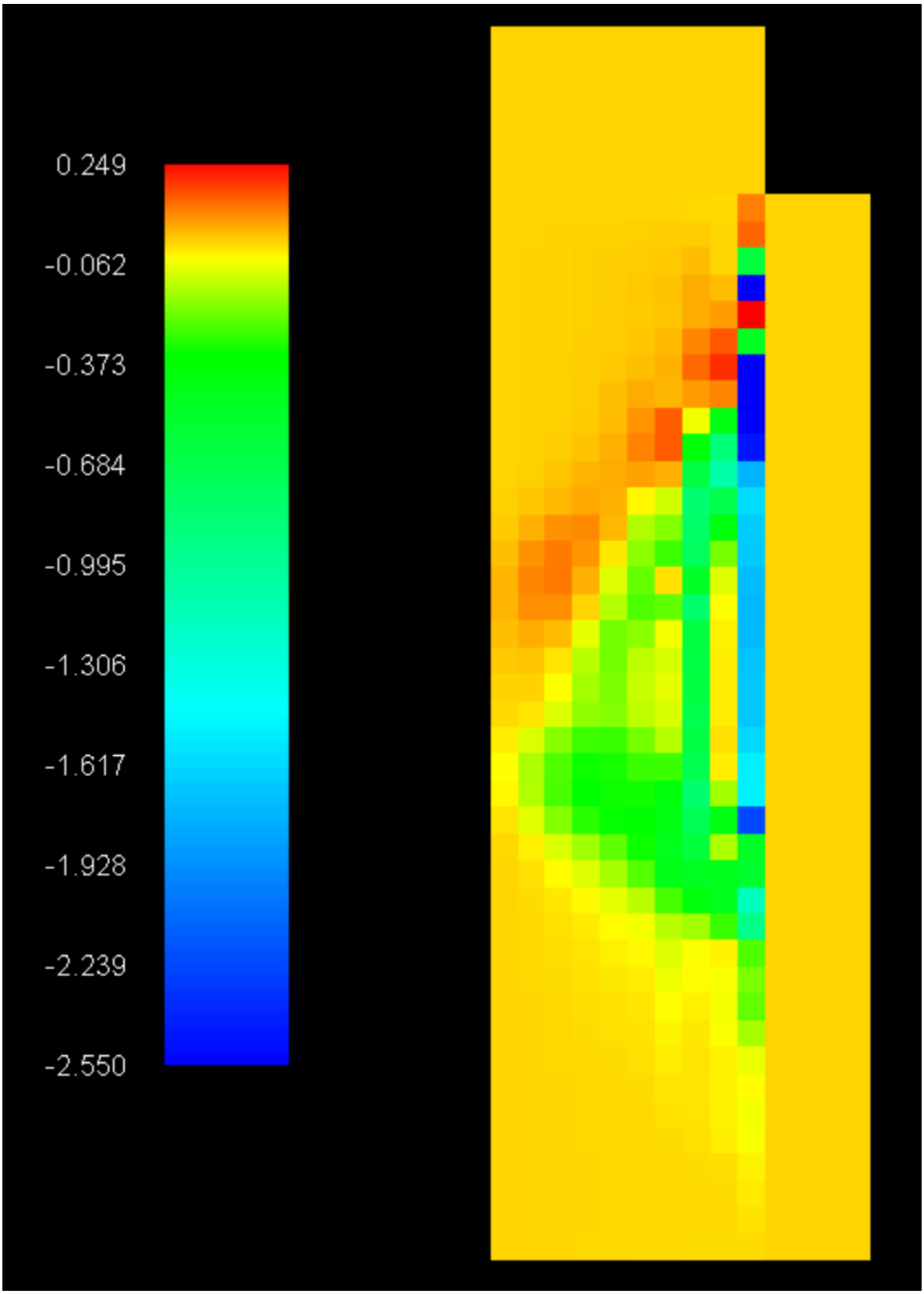

Figure 5-13: Shear band of TF-6 2D numerical load test with χ = 10, post-yield softening geotextiles.

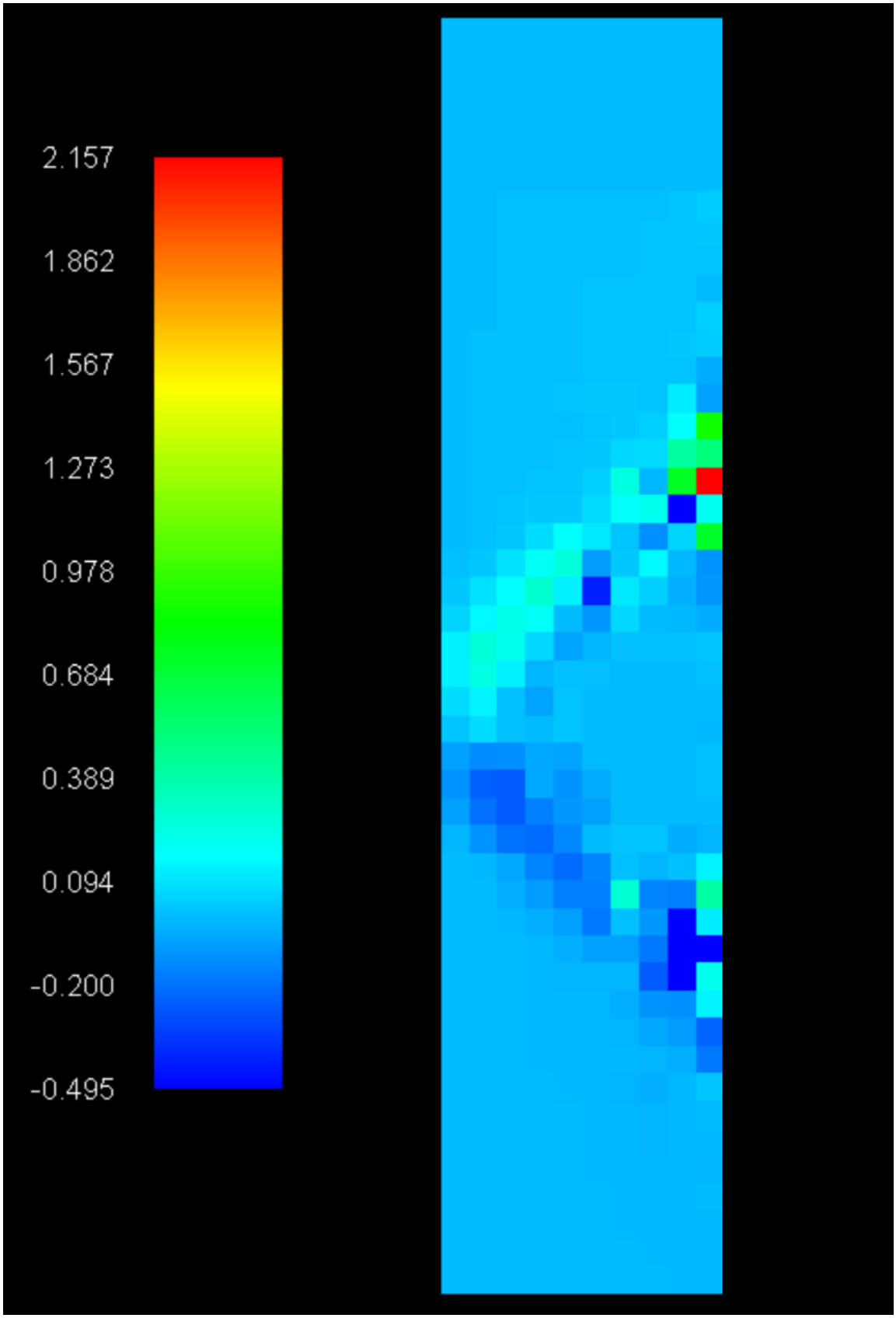

Figure 5-14: Shear band of TF-7 2D numerical load test with χ = 10, post-yield softening geotextiles.

5.2 3-D Analysis

The most ideal GRS model has to be analyzed in 3-D. This was facilitated using the FEMtij-3D program. The mesh shown in Figure 5-15 was created.

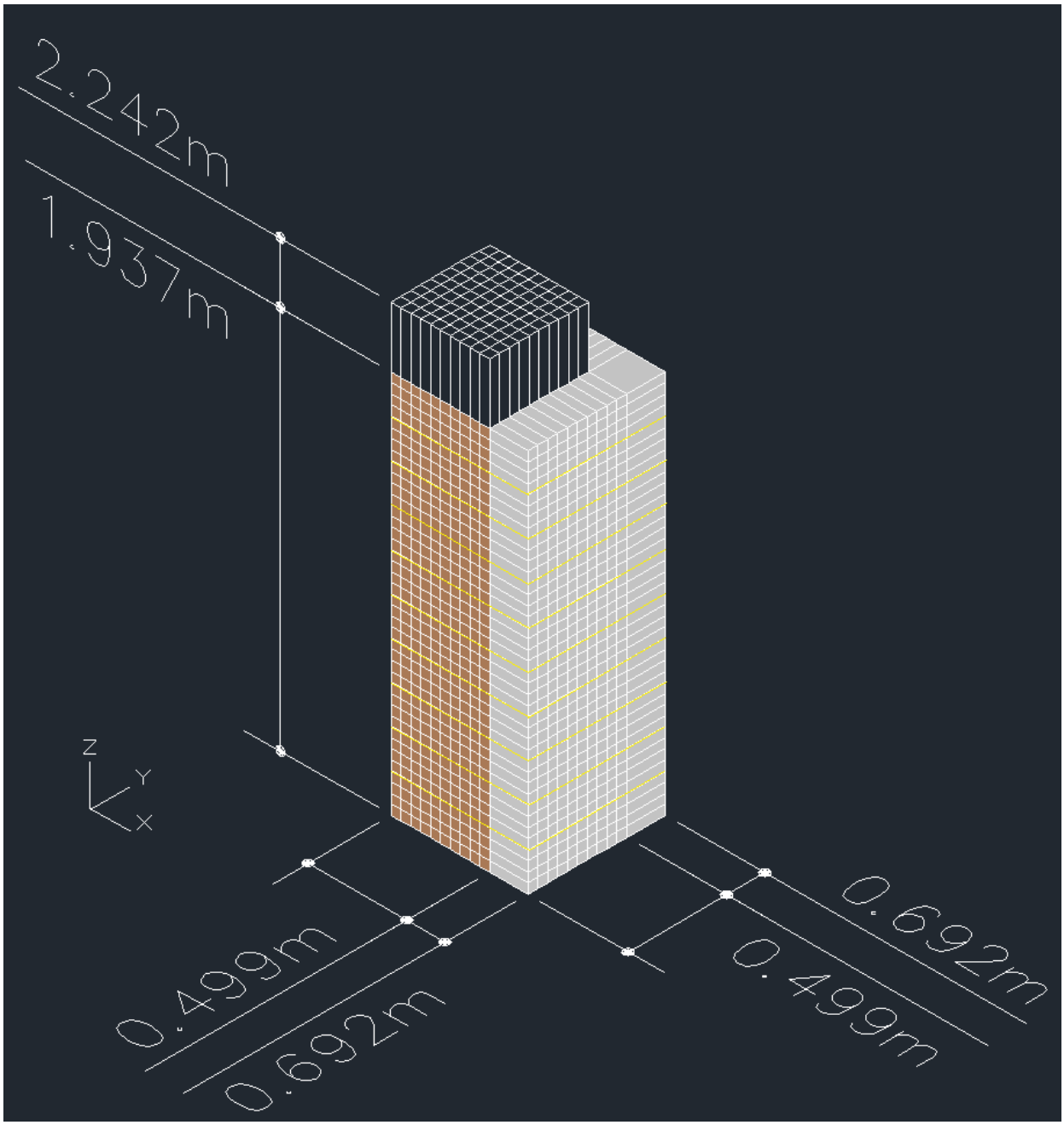

Figure 5-15: 3D finite element mesh.

The mesh represents a scaled model of TF-6 and TF-7 (where TF-7 has its CMUs turned to air) and only a quarter of the GRS was modeled to save computing time. With this mesh, the "making the ground" phase was similar to the 2-D analysis where an input file named "Ground.dat" was created to generate weight and density values for the soil and CMU elements by turning on "gravity" for the elements separately. Then during the loading phase, another input file was created to read the weights and densities of the soil and CMU. The same load set-up, joint elements, material properties, and constitutive models as in the 2-D analysis were used with the exception of the following:

1. The CMU was modeled using linear elastic elements because the Drucker Prager model is not available in FEMtij-3D.
2. The geotextile was modeled using linear elastic membrane elements because the linear elastic membrane elements with post-yield softening are not available in FEMtij-3D.

Unfortunately, numerical difficulties were encountered in the 3D analyses yielding results that looked unreasonable.

6 SUMMARY AND CONCLUSION

6.1 Project Summary

Between 2011 and 2012, 14 GRS columns (mini-piers) were constructed and load tested by the Federal Highway Administration at the Turner-Fairbank Highway Research Center. Of these 14 GRS columns, two of them were simulated numerically: TF-6 and TF-7.

The soil constitutive model used is the subloading tij model developed by Nakai and Mihara (1984). Model parameters were derived based on one isotropic compression and a series of 4 CD triaxial compression tests on the GRS backfill conducted by FHWA's Turner-Fairbank Highway Research Center.

Numerical models were developed in 2-D in plane strain. A 2D analysis does not reflect reality in this case because the GRS columns are square in plan and hence, a 3D model is necessary. A 3-D model was also developed but numerical difficulties were encountered in the analysis as more modifications to the software are necessary to make it work.

The ideal constitutive model for the soil, CMU blocks, geotextile, and footing are the subloading t_{ij}, Drucker-Prager, linear elastic with post-yield softening, and linear elastic models, respectively. With this base case scenario, three factors that can influence the results were investigated and they were (1) the soil-footing friction angle, (2) the constitutive model of the CMU, and (3) the constitutive model of the geotextile. These investigations included comparisons between measured and calculated load-settlement and lateral displacement curves.

6.2 Conclusions

The following conclusions can be made on the 2D GRS numerical load tests:

- All 2D analyses showed that the numerical model behaved in a stiffer fashion than the measured load tests. This is reasonable since on all 4 sides of the GRS column, there is no soil extending beyond the four extremities from restraining the movement laterally. In a 2D plane strain analysis, two of the 4 sides are laterally restrained. Therefore, this trend is reasonable.
- Another reason for the stiffer behavior in the 2D numerical analyses is that the CMU blocks' could have translated during compaction. Ratchet straps were used to restrain the top two rows of CMU blocks during compaction. However, this restraint can by no means

be considered as fixed. Any translation of the CMU blocks would result in a coefficient of lateral earth pressure, K, that is less than the "at-rest" value, K_0. This reduced K value is difficult to estimate. Since K_0 conditions were assumed during making the ground phase, the resulting GRS stiffness response is expected to be higher than the actual stiffness.

- The soil-footing friction angle investigation showed that the capacity of the GRS column increased when the interface friction angle increased from 0° to 33°.
- Using the Drucker-Prager model for the CMU blocks resulted in a smaller GRS capacity than the run with linear elastic CMUs. This is because the linear elastic CMUs have an infinite strength, when in reality, some of the CMU blocks crushed during the performance tests. Thus, it can be concluded that it is important to consider the yielding of the CMU in a numerical load test.
- During the investigation of the constitutive model of the geotextile, it was shown that the GRS vertical capacity is less when it had geotextiles that softened upon yield than the one with linear elastic geotextiles. This is an important consideration due to the fact that the geotextiles ripped during performance testing.
- Shear bands were observed in the GRS columns. They are inclined at 45° and 50° to the horizontal for GRS columns without and with CMU blocks, respectively

6.3 Recommendations for Future Research

For future research, it is desirable to rerun the 3D analysis with an updated FEMtij-3D program that has the post-yield softening membrane element to model the geotextile, as well as the Drucker-Prager constitutive model to model the CMU.

A finer mesh can be considered to investigate if the results become more accurate.

Another recommendation is to run tests that provide more accurate interface friction angles since some of them were values commonly assumed in practice like the soil-footing interface friction angle $\delta = 2\phi/3$ (33˚).

It would be most ideal if all the soil tests were conducted at the same conditions as the GRS backfill. For example, the drained triaxial test samples had a relative compaction of 95% while the GRS columns' backfill was at 100%. Furthermore, the triaxial tests were saturated while the GRS backfill was unsaturated.

Lastly, future research could include numerically load testing the other GRS column performance tests with different geotextile strengths and spacing.

7 REFERENCES

ACI Committee 318. (2008). *Building code requirements for structural concrete: (ACI 318-08) and commentary*. Farmington Hills, MI: American Concrete Institute.

Adams, M., Nicks, J., Stabile, T., Wu, J., Schlatter, W. and Hartmann, J. (2011). *Geosynthetic Reinforced Soil Integrated Bridge System Interim Implementation Guide.* Federal Highway Administration, Report No. FHWA-HRT-11-026, McLean, VA.

ASTM Standard C90-12. (2012). *Standard Specification for Loadbearing Concrete Masonry Units*. ASTM International, West Conshohocken, PA, 2012, DOI: 10.1520/C0090-12, www.astm.org.

Fredlund, D. G. and Morgenstern, N. R. (1977). *Stress State Variables for Unsaturated Soils.* ASCE J. Geotech. Eng. Div. GT5, 103: 447-466.

Fredlund, D. G. and Rahardjo, H. (1993). *Soil Mechanics for Unsaturated Soils.* Toronto, Canada: John Wiley & Sons, Inc.

Fredlund, D. G. and Wong, D. K. H. (1989). *Calibration of Thermal Conductivity Sensors for Measuring Soil Suction.* ASTM Geotech. J. 12 (3): 188-194.

Fredlund, D. G. and Xing, A. (1994). *Equations for the soil-water characteristic curve.* Canadian Geotechnical Journal, 31 (3): 521-532.

Iwamoto, M. K., Ooi, P. S. K., Nicks, J. E. and Adams, M. T. (2014). *Observations From Load Tests on Geosynthetic Reinforced Soil.* (Master's thesis, University of Hawai'i at Manoa, Honolulu, Hawai'i).

Kaya, L. H., Ooi, P. S. K., Nakai, T., Adams, M. T., Nicks, J. E. and Shahin, H. Md. (2016). *Numerical Load Testing of a Geosynthetic Reinforced Soil*, presented at Civil Engineering Conference in the Asian Region CECAR 7, Honolulu, HI, 2016.

Martin. J. P. Koerner, R. M. and Whitty, J. E. (1984). *Experimental Friction Evaluation of Slippage Between Geomembranes, Geotextiles and Soils.* Proceedings of the Intl. Con5 on Geomembranes, Denver, Colorado: 191-196.

Matsuoka, H. (1974). *Stress-strain relationship of sand based on the mobilized plane.* Soils and Foundations 14 (2): 47-61.

Matsuoka, H. and Nakai, T. (1974). *Stress-deformation and strength characteristics of soil under three different principal stresses.* Proceedings of JSCE 232: 59-70.

Nakai, T. (1989). *An isotropic hardening elastoplastic model for sand considering the stress path dependency in three-dimensional stresses.* Soils and Foundations 29 (1): 119-137.

Nakai, T. (2013). *Constitutive Modeling of Geomaterials: Principles and Applications*. Boca Raton, FL: CRC Press, Taylor and Francis Group.

Nakai, T. and Mihara, Y. (1984). *A new mechanical quantity for soils and its application to elastoplastic constitutive models.* Soils and Foundations 24 (2): 82-94.

Nicks, J. E., Adams, M. T., Ooi, P. S. K. and Stabile, T. (2013). *Geosynthetic Reinforced Soil Performance Testing – Axial Load Deformation Relationships.* Federal Highway Administration, Report No. FHWA-HRT-13-066, McLean, VA.

Roscoe, K. H., Schofield, A. N. and Thurairajah, A. (1963). *Yielding of clays in states wetter than critical*. Geotechnique 13 (3): 211-240.

Roscoe, K. H. and Burland, J. B. (1968). *On the generalized stress-strain behavior of wet clay*. In Engineering plasticity, ed. J. Heyman and F. A. Leckie. Cambridge, England: Cambridge University Press, 535-609.

SoilVision. (2001). SoilVision Software Users Guide, Version 3.0, 2nd Edition. SoilVision Systems, Ltd., Saskatoon, Canada.

Tatsuoka, F. (1978). *Stress-strain behavior of an idealized granular material by simple elastoplastic theory.* Proceedings of United States-Japan Seminar on Continuum Mechanical Statistical Approaches of Granular Materials, Sendai, Japan, 301-320.

Vanapalli, S. K. and Fredlund, D. G. (2000). *Comparison of Different Procedures to Predict Unsaturated Soil Shear Strength*. GeoDenver Conference. Denver, Colorado: 195-209.

Wood, D. M. (1990). *Soil Behavior and Critical State Soil Mechanics.* Cambridge, England: Cambridge University Press.